Quantum Cascade Laser Frequency Combs

by

Theodore Peter Letsou

B.S.E, Engineering Physics
Case Western Reserve University (2019)

Submitted to the Department of Electrical Engineering and Computer Science
in partial fulfillment of the requirements for the degree of

Master of Science in Electrical Engineering and Computer Science

at the

MASSACHUSETTS INSTITUTE OF TECHNOLOGY

September 2021

Author .....
Department of Electrical Engineering and Computer Science
August 27, 2021

Certified by .....
Qing Hu
Distinguished Professor of Electrical Engineering and Computer Science
Thesis Supervisor

Accepted by .....
Leslie A. Kolodziejski
Professor of Electrical Engineering and Computer Science,
Chair, Department Committee on Graduate Students

Quantum Cascade Laser Frequency Combs

by

Theodore Peter Letsou

Submitted to the Department of Electrical Engineering and Computer Science
on August 27, 2021, in partial fulfillment of the
requirements for the degree of
Master of Science in Electrical Engineering and Computer Science

Abstract

Quantum cascade lasers (QCLs) have been the dominant source of high-power infrared radiation ever since their invention in 1994. The ability to engineer their emission wavelengths from 3 μm to 300 μm has allowed scientists to use QCLs in a plethora of applications, ranging from spectroscopy to tomography. In addition, QCLs are highly non-linear devices, and possess the ability to emit many frequencies of light simultaneously. This has made them excellent candidates for frequency combs, which are broadband light sources that emit equally-spaced frequencies with a well-defined phase relation. By manipulating the optical non-linearities through dispersion engineering, QCLs can be made to enter frequency combs states on-demand. By mixing two different frequency combs, absorption features at optically frequencies can be encoded into the radio-frequency domain, eliminating the need for expensive, high-frequency detectors. This "dual-comb spectrometer" offers a chip-scale alternative to bulky spectrometers, making it one of the most attractive applications of QCLs.

This thesis outlines the development, characterization and theory of QCL frequency combs operating in the atmospheric transmission window (8 μm – 12 μm)—a spectral region where many chemical species have their fundamental vibrational and absorption bands. By borrowing techniques commonly used in ultra-fast optics, the dispersion of QCLs—which is the primary catalyst for comb formation—can be tuned without the use of mechanically-moving parts. In addition, this thesis utilizes optical coherence techniques to reconstruct the electric field profile of QCL combs, which provides valuable insight on the physics of their formation.

Thesis Supervisor: Qing Hu
Title: Distinguished Professor of Electrical Engineering and Computer Science

Acknowledgments

First and foremost, I would like to thank Professor Qing Hu for providing me an opportunity to work on such a stimulating project. QCLs lie directly at the intersection of physics and engineering, and I am especially grateful for Qing's wisdom and guidance in exploring this deeply rich field.

Throughout my time in the group, I've had the pleasure to interact with many amazing labmates, all of which have incredibly different personalities. Elise Uyehara is one of the most patient people I've ever met. Her willingness to discuss any topic at any pace for any duration is truly unique. She is also from Hawaii, which automatically makes her the coolest person I know. Tianyi Zeng taught me every experimental technique I know. He is intensely inquisitive, and will never let a half-answer slide. Despite having to completely invert his schedule to fabricate the devices shown in this thesis (for which I am eternally grateful), Tianyi is never without a smile (and a Vanilla Latte). Ali Khalatpour taught me what hard work actually means. His determination and willingness to go the extra mile in every situation is something I stride for. He is also an extremely gifted plumber. Finally, Andrew Paulsen is pretty much the most down-to-earth person MIT has to offer. Anyone who talks to Andrew knows he has a variety of interests, from machining, to bowling, to farm animals. He always knows the correct answer, and gives valuable advice both inside the lab and out.

I would like to thank my great-aunt, Athena, for always willing to spend time with me in Lowell, and showing me the importance of family.

I would also like to thank my brother, William, and my sister, Tina for being amazing role models growing up. As the youngest of the family, I always wanted to be like my siblings in pretty much every way. I can thank them (for better or for worse) for all of my habits, mannerisms, and my passion for problem-solving.

Finally, I would like to thank my parents, Peter and Felicity, for providing loving support, and constantly stressing the importance of always putting your best forward. This thesis is dedicated to them.

Contents

List of Figures

List of Tables

Chapter 1

Introduction

Frequency combs based on quantum cascade lasers (QCLs) are coherent, broadband light sources that emit equally-spaced frequencies spanning from the mid-infrared (3 - 8 μm) to the THz (30 μm to 300 μm) portion of the electromagnetic spectrum. By optically mixing two frequency combs, a "dual-comb spectrometer" is realized, offering a chip-scale alternative to bulky spectrometers.

This chapter serves as a brief introduction towards the motivation and development of QCL frequency combs operating in the atmospheric transmission window (8 μm – 12 μm)—a spectral region where many chemical species have their fundamental vibrational and absorption bands.

1.1 Infrared spectroscopic techniques

Terrorist attacks on United States soil have garnered a significant amount of attention in recent years. With terrorists implementing increasingly sophisticated techniques to cause causalities on a large scale, the need for direct detection of chemical explosives in populated urban environments is of paramount importance. This thesis serves to address this complex issue by outlining the development of a spectroscopic sensor based on quantum cascade laser frequency combs operating in the mid-infrared spectral range. This technology is uniquely suited for detecting trace ($<$ 10 parts-per-billion (ppb)) amounts of a broad range of chemical warfare agents (sarin, tabun,

soman, etc.) and simulants (DIMP, DEMP, DMMP, etc.) by operating within the atmospheric transmission window (8–12 μm).

Other sensing techniques such as light detection and ranging (LIDAR), open-path tunable laser absorption spectroscopy (OP-TDLAS), and open-path Fourier transform infrared spectroscopy (OP-FTIR) have been used in the past with mixed results. LIDAR sensing is typically performed by back-scattering light from objects of interest. Unfortunately, back-scattering is much weaker in the mid-infrared spectral region as compared with the visible or ultraviolet range, leading to a weak return signal. OP-TDLAS is a similar technique to LIDAR, where spectral information is gathered using a strong, tunable light source, such as a diode laser. Despite being optically bright sources, diode lasers are often weakly tunable, rendering them ineffective in targeting multiple chemical species. In order to increase the tunability of these light sources, complex external apparatuses involving mechanically moving parts must be employed. On the other hand, OP-FTIR can directly measure over a large spectral range in the mid-infrared, but it cannot be used in remote sensing. Furthermore, OP-FTIR also requires the use of mechanically moving parts in the form of a Michelson interferometer.

Spectroscopy utilizing frequency combs has recently been studied as an effective alternative for remote sensing of chemical species. Two frequency combs with repetition rates f_r and $f_r + \Delta f_r$ can be operated simultaneously in a dual-comb spectroscopy (DCS) setup. At optical frequencies, the comb "teeth" are spaced evenly with a separation given by the repetition rate, resulting in equally spaced beat-notes in radio frequency (rf) spectra (Fig. 1-1(a) [1]). Therefore, absorption features measured at optical frequencies are encoded into the rf domain using a single fast photoreceiver. DCS can also be used in both asymmetric and symmetric configurations, where measurements of the phase and amplitude of the rf comb teeth are utilized, respectively (Fig. 1-1(b) [1]). DCS offers unique advantages over the aforementioned sensing mechanisms. Primarily, frequency combs can span a broad spectral range ($\approx$ 100 cm^{-1}) without sacrificing the modal quality associated with single mode lasers, making them suitable for the simultaneous detection of multiple chemical species.

Additionally, frequency combs can operate with high finesse without the use of mechanically moving parts, allowing for a high range of versatility with respect to sensing environments.

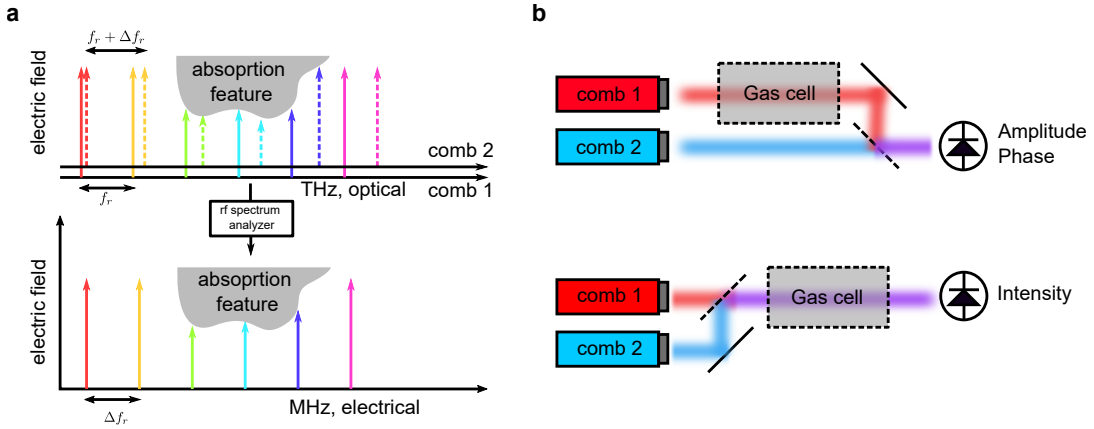

Figure 1-1: **Dual-Comb Spectroscopy.** (a) Two frequency combs with repetition rates f_r and $f_r + \Delta f_r$ mixed in a fast photodetector. Through multiheterodyne down conversion in a fast photodectors, a frequency comb with a uniform mode spacing Δf_r generated at rf frequencies (GHz), which can be easily analyzed using microwave instruments. Absorption features at optical frequencies are then encoded into the rf spectra. (b) DCS can be performed with either one or both combs passing through the sample. The absorption feature is then measured using the phase or amplitude of the comb teeth, respectively. Adapted from [1].

Frequency combs are traditionally formed using mode-locked lasers. However, they are often expensive and bulky, limiting their use outside the lab environment. Additionally, mode-locked lasers are unable to produce high power radiation in the mid-infrared spectral range. Recently, DCS was performed in the near-infrared spectral range using frequency combs based on mode-locked lasers with a total power of 160 μW [7], achieving a molecular sensitivity on the order of 10 ppm over a duration of 100 s to average the low power signal. This level of sensitivity is often insufficient for remote sensing. Frequency combs can also be formed using optical parametric oscillators or by pumping $\chi^{(3)}$ -nonlinear materials with an infrared continuous wave (CW) source [4]. Despite producing large, high-power spectral coverage in the mid-infrared spectral range, both of these methods require large experimental apparatuses, eliminating the possibility of chip-sized scalability.

1.2 Spectroscopy based on quantum cascade lasers

The technological foundation for this thesis is frequency combs based on the quantum cascade laser (QCL)—a semiconductor laser where mid to far-infrared radiation is emitted by intersubband transitions in repeated quantum well heterostructures (Fig. 1-2(a)). QCL lasers afford a number of distinct advantages over traditional semiconductor lasers in sensor operation. QCLs offer a wide range of wavelength selectivity, because light is produced by the electron's motion through an engineered gain structure rather than through electron-hole recombination across a bandgap (Fig. 1-2(b)). This flexibility allows for operation in the atmospheric transmission window, for example the long-wave infrared window (LWIR, 8-12 μm) that is very important for military applications where a number of chemical species have their fundamental vibration absorption bands. In addition, QCLs are naturally broadband devices making them excellent candidates for frequency comb formation with high optical power per mode (10 mW/mode).

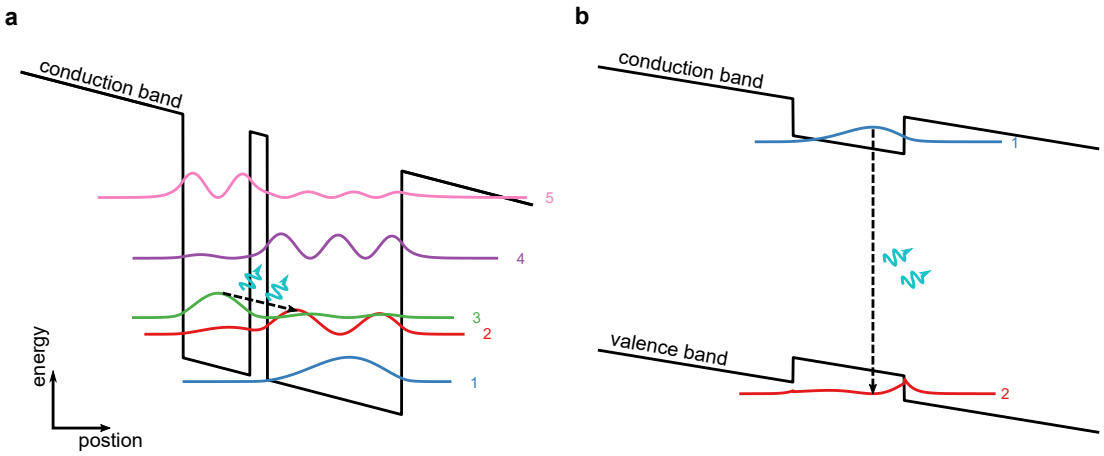

Figure 1-2: **Lasing from Quantum Wells** (a) An example of a quantum cascade laser (QCL) where laser photons are emitted by an electron transition in the conduction band of a quantum well heterostructure. Laser photons are emitted between levels 3 and 2. (b) An example of a quantum well laser where laser photons are emitted though electron-hole recombination across a bandgap.

Despite the fact that the first mid-infrared QCL frequency comb was achieved without compensation for the laser's natural dispersion (a non-trivial phase relation

between cavity photons) [5], it has recently been shown that deliberate dispersion compensation is necessary for stable comb formation over a large bandwidth and dynamic range c. Therefore, in order for a spectrometer based on QCL frequency combs to achieve a high level of sensitivity across the atmospheric transmission window, developing an effective method of dispersion compensation is of the upmost importance.

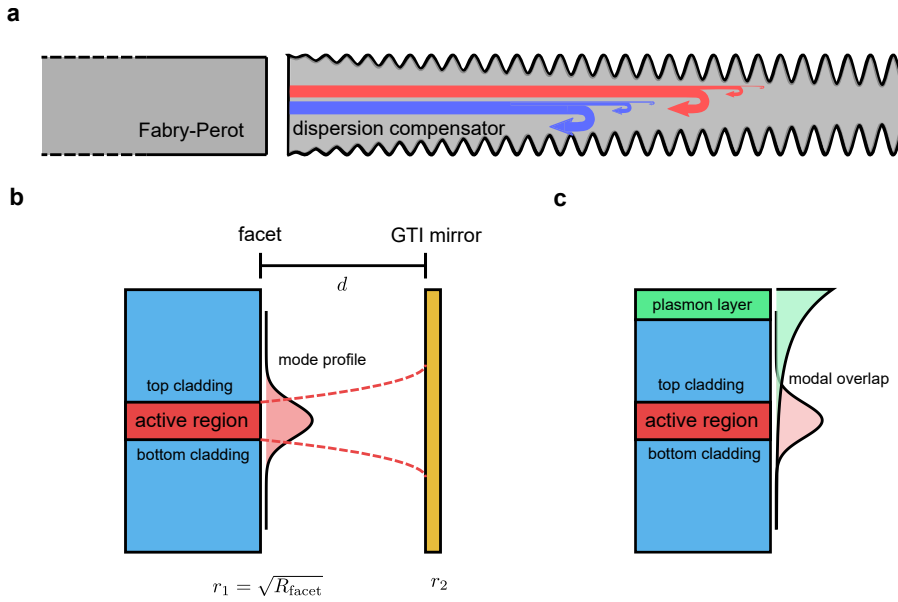

Figure 1-3: **Dispersion Compensation Schemes** (a) Chirped gratings delay different wavelengths of light (shown here by blue and red arrows) different distances by "chirping" the periodicity of a Bragg reflector. This scheme acts both as a high-reflectivity (HR) coating as well as a dispersion compensator. (b) Gires-Tournois interferometer (GTI) mirrors compensate dispersion by externally reflecting photons back into the cavity after a round-trip through the waveguide. Depending on the position of the mirror, dispersion can be partially compensated. (C) Surface-plasmon enhanced waveguides utilize the modal overlap of the plasmonic mode of a highly-doped layer on the top cladding (green profile) with the fundamental cavity mode of the waveguide (red profile) to negate the laser's dispersion.

As summarized in Fig. 1-3, there are three main dispersion compensation schemes used for QCLs: (a) chirped gratings [8], (b) tunable Gires-Tournois interferometer (GTI) mirrors [9], and (c) surface-plasmon enhanced waveguides [10]. The chirped grating compensation scheme delays light with higher group velocity by forcing the light to travel further along the grating. Thus, light of all group velocities will traverse

the length of system in the same amount of time, eliminating the intrinsic dispersion of the laser. This compensation scheme can be directly integrated with the QCL comb using electron beam lithography and has been shown to compensate for dispersion up to the fourth order [11]. In addition, the chirped grating acts as a Distributed Bragg Reflector (DBR), reducing the current required to achieve lasing, otherwise known as current threshold. However, in order to properly design the chipped grating, an accurate measurement of the laser's dispersion must be performed.

Unlike chirped gratings, GTI mirror compensation does not require an extensive dispersion measurement. Instead, a computer-controlled mirror acts as an external cavity to the QCL. Although easier to integrate than chirped gratings, GTI mirrors are limited to partial dispersion compensation. Moreover, the use of a computer-controlled stage drastically reduces the scalability of this scheme.

Surface plasmon controlled waveguides are a robust method of dispersion compensation that can be directly implemented in the QCL comb by overlapping a plasmonic mode with the fundamental mode, altering the refractive index distribution of the device. Similar to GTI mirrors, this method is also limited to partial compensation.

The bulk of this thesis was spent on the design and characterization of chirped grating dispersion compensators as they provide the most versatility when it comes to dispersion control. In addition, chirped gratings can be fabricated such that they are optically coupled to the rest of the laser waveguide, while remaining electrically isolated. This allows for independent tuning of the dispersion compensator, which has been shown to lead to comb formation over the entire lasing range of the QCL [11].

1.3 Concluding remarks

QCL frequency combs were only recently developed in 2012; therefore, there are still many fundamental questions on a device level that need to be understood, such as the exact role dispersion plays in output modulation of frequency combs. In order to elucidate some of key physical features that cause comb formation, both theoretical

models based off of the Maxwell-Bloch equations (MBE) [12, 13, 14] and experimental coherence techniques are explored. One such QCL coherence technique (and the most powerful) is Shifted Wave Interference Fourier-Transform Spectroscopy (SWIFTS). Using SWIFTS, the level of mutual coherence among comb teeth can be directly measured to the sub-Hz level [15]. The relative phase between comb lines can also be measured using SWIFT, which can be used to reconstruct the time-domain profile of the comb output [16].

QCL frequency combs lie directly at the intersection of engineering and physics. In order for such a device to be implemented in a chip-scale, dual-comb spectrometer, both physical understanding and high-resolution fabrication techniques must be utilized. This thesis aims to address both of these points. The remainder of this thesis is organized as follows.

- Chapter 2 provides a brief historical overview of QCLs and discusses the physically processes involved in their operation.
- Chapter 3 discusses fabrication methods as well as basic measurement techniques.
- Chapter 4 discusses how frequency comb states arise from multi-mode states in QCLs.
- Chapter 5 discusses dispersion engineering and presents some initial results.
- Chapter 6 discusses coherence techniques commonly used to evaluate comb performance.
- Chapter 7 discusses the theoretical framework used to describe the field profile of combs.
- and Chapter 8 provides some concluding remarks and possible future directions.

Chapter 2

Quantum Cascade Lasers: History and Theory

At its core, the quantum cascade laser (QCL) is an electron waterfall. When the device is electrically pumped, electrons travel through a periodic structure of multiple quantum wells (MQWs), confined to states that are solutions to the Schrödinger equation. Specific transitions between states are "selected" by the engineer to emit a certain wavelength of photon. The QCL is unique as compared to other laser systems for two reasons: firstly, each electron that traverses through one period (or module) of the structure will emit one photon; secondly, the wavelength of the emitted photon is only dependent on the geometry of the MQWs instead of intrinsic material properties. It is for these two reasons that QCLs have become the dominant source of high-power radiation throughout the mid-infrared and THz regimes.

This chapter serves as an overview of the history and working principles of QCLs. In addition, methods for solving for the electronic states of QCLs are discussed.

2.1 Quantum cascade laser history

The first quantum cascade laser was demonstrated by Jérôme Faist and co-workers in the Capasso group at Bell Laboratories in 1994. Faist *et. al.* achieved lasing through a series of $In_{53}Ga_{47}As/In_{52}Al_{48}As$ heterostructures grown by molecular-beam epitaxy

(MBE). This result is the culmination of decades of theoretical and experimental work, much of which took place at the Bell laboratories.

Interestingly, the original concept for intersubband lasing predates the invention of the traditional semiconductor laser. In 1960, Lax published a paper hypothesizing that population inversion could be achieved between Landau levels in the valence band of Germanium in the presence of magnetic fields [17]. Although experimentally demonstrated several years later [18], the need for high-power (>1 T) magnetic fields hindered the laser's potential applications. Around the same time period, other theoretical studies predicted interesting quantum effects in MQW systems.

The most notable paper of this era was published by Kazarinov and Suris in 1971 [19]. They postulated that the electronic levels in the conduction band of a quantum well superlattice could be used to achieve light amplification. When the superlattice is biased, the quantum wells begin to "tilt" in energy space, causing electrons to flow through the system. As the electrons flow, their wavefunctions are restricted to energy levels that correspond to solutions of the Schrödinger equation. Electrons move through the system a number of different ways. While inside the quantum wells, the electrons can either scatter to different states (intersubband scattering) or emit a photon. When traveling between quantum wells, electrons can scattering to different states, emit a photon or resonantly tunnel through the potential barrier.

Before proceeding, it is important to discuss how electrons tunnel through the potential barrier [20]. To first order, electrons can tunnel when there is an available state on the other side of the barrier that matches the electron's energy, E, and lateral momentum, k_x and k_y. Consider the double quantum well system with two subbands labeled blue and red as shown in Fig. 2-1. When the two electronic subbands are separated such that the energy of the red subband ($E_{\mathrm{red}} = \frac{\hbar^2 k_0^2}{2m^*}$, where k_0 is the z component of the state momentum, $\hbar$ is the reduced Planck's constant and m^* is the effective mass of the electron) is higher than the Fermi level, E_{F}, of the system, no electrons can tunnel across the barrier.

Another way to view the system is through the so-called Fermi sphere. All possible electron momenta (k_x, k_y, k_z) that exist in the system lie within the shaded region

of the Fermi sphere with radius k_f. At zero bias, k_0 lies outside the Fermi sphere. Therefore, there are no states in the red subband that correspond to any electrons in the system. As the quantum wells are biased, k_0 begins to drop within the Fermi sphere, meaning that electrons in the blue subband with lateral momentum that lie on the shaded disk are able to tunnel to red subband. As the bias is increased further such that $k_0^2 = 0$ (corresponding to the equator of the Fermi sphere), the two subbands are completely resonant, and amount of the tunnelling electrons per unit area is equal to $\frac{m^* E_F}{\pi\hbar^2}$. Past this bias point, no electrons can tunneling while conserving their lateral momentum. Physically, this results in a abrupt decrease in tunneling current known as negative differential resistance (NDR).

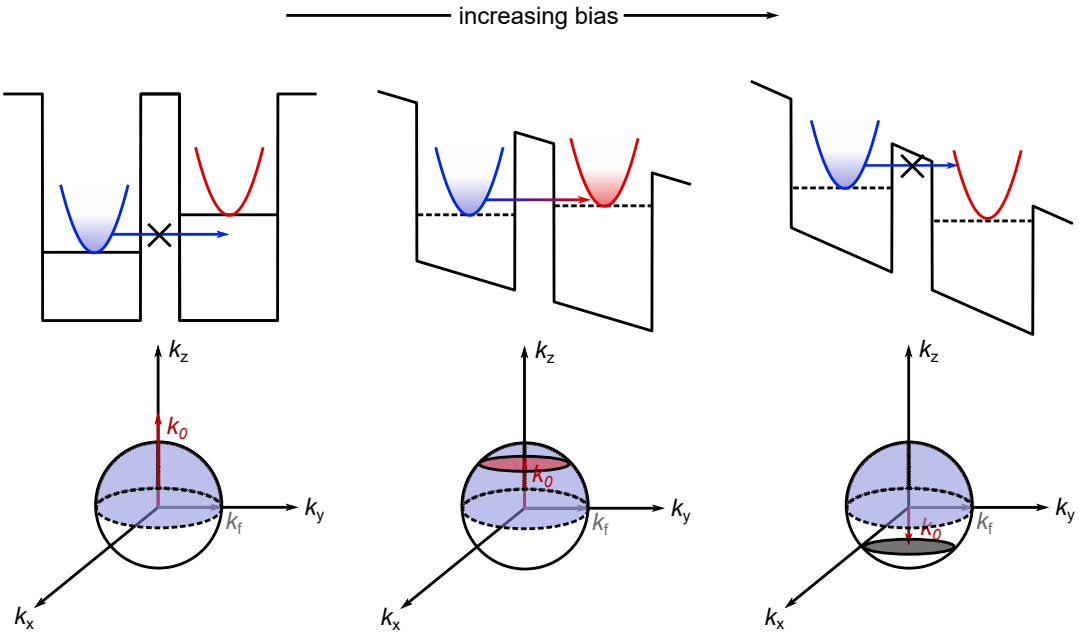

Figure 2-1: **Tunneling Across a Potential Barrier** A two quantum well system is biased at three differential potentials. As the bias is increased from 0 to non-zero values, the blue and red subband go in and out of resonance. To first order, tunneling between the two subbands occurs if the electron's lateral momentum can be conserved.

Kazarinov and Suris' original design is shown in Fig. 2-2. At bias point V_1 electrons in level 4 can both tunnel to the adjacent quantum well and scatter to state 3, leading to an increase in current as shown in the hypothetical IV curve. Another resonant condition is reached at bias point V_2. Here, levels 3, 4 and levels 3, 2 strongly

overlap. Physically, this means electrons in the ground of one quantum well (levels 5 and 3) are in resonance with the first excited state of the adjacent quantum well (levels 4 and 2). Transport is further enhanced by the emission of longitudinal-optical (LO) phonons from level 4 to 3. Due the sub-picosecond nature of LO-phonon emission, the ground state of each quantum well is more populated than any excited state. Therefore, population inversion ($n_3 > n_2$, where n_i is the concentration of electrons in level i) is achieved for biases above V_2. At bias point V_3, electrons in levels 3 begin coherently oscillating with electrons in state 2, forming an electric dipole. As a result of these oscillations, photons are emitted between levels 3 and 2. A sharp decrease in current is expected as the system is biased out of the peak resonant condition (above V_2); hence, NDR is predicted.

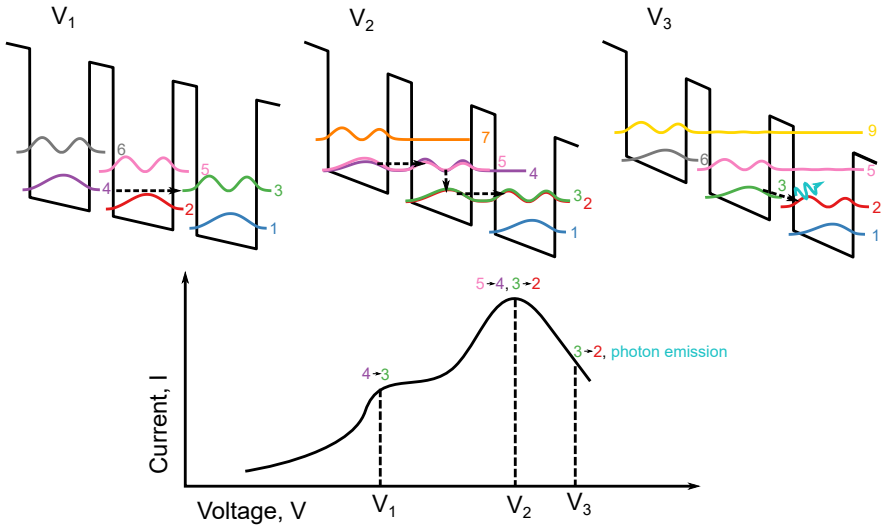

Figure 2-2: **Kazarinov and Suris Proposal** A superlattice of quantum wells is biased at three different potentials. At V_1, electrons in level 4 can scatter and tunnel to level 3 leading to a local peak in current. V_2 corresponds to the maximum current in the superlattice; electrons can tunnel from 5 to 4, emit a phonon to level 3, then tunnel from 3 to 2. At V_3, there is sufficient interaction between levels 3 and 2, that coherent electric dipole oscillations can occur, leading to the emission of a photon. Population inversion is achieved though the ultra-short lifetimes of the excited state, level 2. This dipole oscillation leads to NDR. This figure is adapted from [2].

This paper provided sufficient fuel to the fire towards the development of a practical intersubband laser. With significant technological improvements in MBE growth

since its birth in 1968 [21, 22], many attempts were made to realize the structure proposed by Kazarinov and Suris. However, some physical limitations in the original proposal – notably, electrical instability due to charge build-up and the inability to bias the structure into the NDR regime – make the structure impossible to achieve. In addition, the states involved in lasing (states 3 and 2) are separated by a barrier. In order for photons to be emitted, the phase of the wavefunctions must preserved while tunneling, otherwise known as coherent tunneling. Experimentally, coherent tunneling is hard to achieve in such a diagonal design. Electrons undergo ultra-fast scattering processes that randomize the phase of the wavefunctions, thus destroying phase coherence. Further specifics on the issues associated with this design can be found in [2].

Despite this, efforts persisted throughout the 1970s and 1980s. Notable achievements include experimental demonstration of resonant tunneling through double barriers by Chang *et. al.* in 1974 [23] and the first experimental demonstration of incoherent resonant tunneling through a superlattice by Capasso *et. al.* in 1985 [24].

Incoherent – otherwise known as sequential – resonant tunneling turned out to be fundamental towards the creation of the first quantum cascade laser. The structure designed by Capasso *et. al.* is reproduced in Fig. 2-3. Unlike Kazarinov and Suris' design where the photon transition was diagonal across a barrier, Capasso's design has a highly vertical photon transition between states 3 and 2. Therefore, tunneling from 4 to 3 does not need to be coherent, and scattering processes may assist in tunneling. Furthermore, depopulation of level 2 is designed to coincide with the LO phonon energy. However, this design was not able to achieve population inversion.

Instead of emitting a photon, electrons in level 3 also relax to level 2 by ultra-fast LO phonon emission. This is depicted in the energy-momentum (EK) diagram for levels 1, 2 and 3 in Fig. 2-4 (a). According to Fermi's golden rule, the LO phonon scattering rate is inversely proportional to the square of the exchange momentum that occurs during scattering (the exchange momentum is shown by the green and red dotted arrows). Thus, to suppress LO phonon emission from levels 3 to 2, the exchange momentum must be made larger. One way to do so is to increase the energy

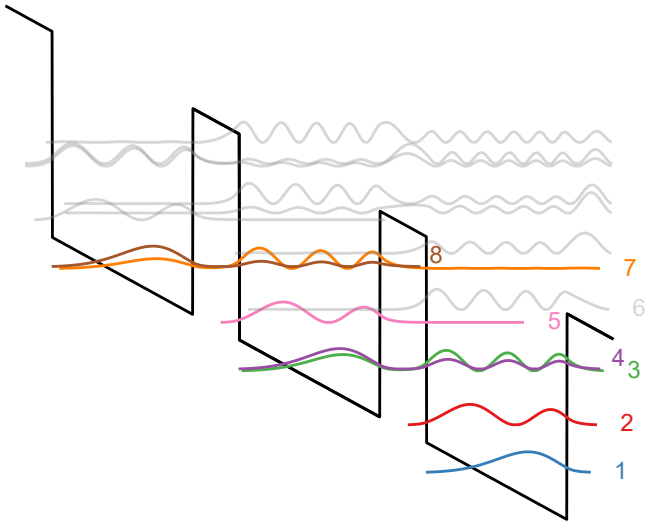

Figure 2-3: **Capasso *et. al.* design** Scattering-assisted tunneling takes place between states (8,7) and states (4,3). LO phonon emission is designed to primarily take place between states (5,4) and states (2,1), but parasitic LO phonon emission prevented the design from lasing.

separation between levels 3 and 2 (Fig. 2-4 (b)). Even with non-parabolicity effects considered, the exchange momentum required for LO phonon emission is significantly increased by adjusting the energy of level 3.

Indeed, by suppressing LO phonon emission from levels 3 to 2, the first quantum cascade laser (QCL) was born [25]. To achieve this, Faist *et. al.* developed the superlattice structure shown in Fig. 2-5. The three coupled quantum wells (dubbed active region) is where the photon transition occurs. By adjusting the widths of the quantum wells, the energy separation between levels 3 and 2 can be made arbitrarily large. This large energy separation causes the lifetime associated with LO phonon emission to be several ps (Faist estimated 4.7 ps). Coupled with a fast (0.6 ps) lower state depopulation lifetime, lasing was achieved at 4.7 μm.

Efficient injection into level 3 is achieved by use of a digitally graded alloy, which is effectively a series of highly doped quantum wells. This implementation of quantum wells creates a series of highly resonant quantum states densely packed in energy known as a "mini-band". At design bias, the mini-band is resonant with both level 1 and level 3 of the next module, therefore electrons are quickly extracted from level 1

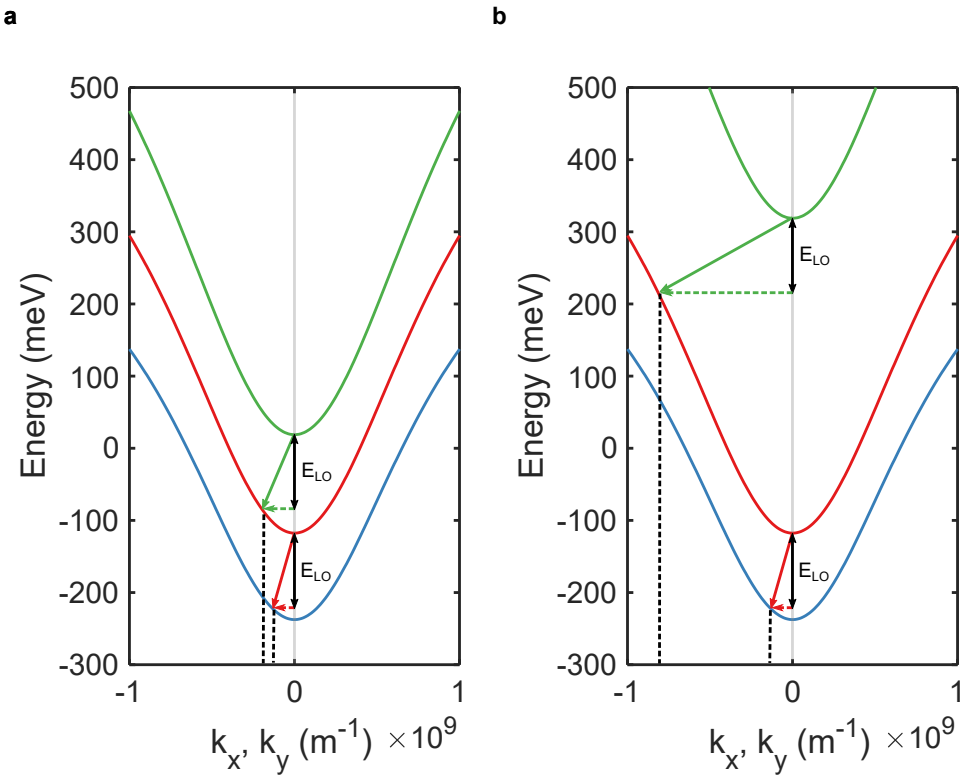

Figure 2-4: **Energy-momentum (EK) diagrams** (a) The EK diagram for Fig. 2-3 and (b) the EK diagram for Fig. 2-3 with adjusted energy spacing between levels 3 and 2. Non-parabolicity is considered.

and injected to level 3. Additionally, the graded alloy serves to block electrons from escaping out of level 3 to the continuum (over the potential barrier), as there are no states in alloy near the continuum. The first QCL lased up to a temperature of 10 K biased at 0.1 % duty cycle. The threshold current density was 11 kA/cm^2 with a peak output power of 8.5 mW. Since then, QCLs have improved dramatically. Room temperature (RT) operation and continuous-wave (CW) operation was achieved in 1995 [26, 27], simultaneous RT-CW operation was achieved in 2001 [28] and far-infrared (THz) QCLs were developed in 2002 [29]. Today, RT-CW QCLs operating from 3 μm to 11 μm are commercially available with output powers exceeding 1 W [30]. One such design is shown in Fig. 2-6 [31].

Electrons in the upper lasing state (8) can transition to a continuum of states (7, 6, 5, ...) and are subsequently injected into the following module. This design –

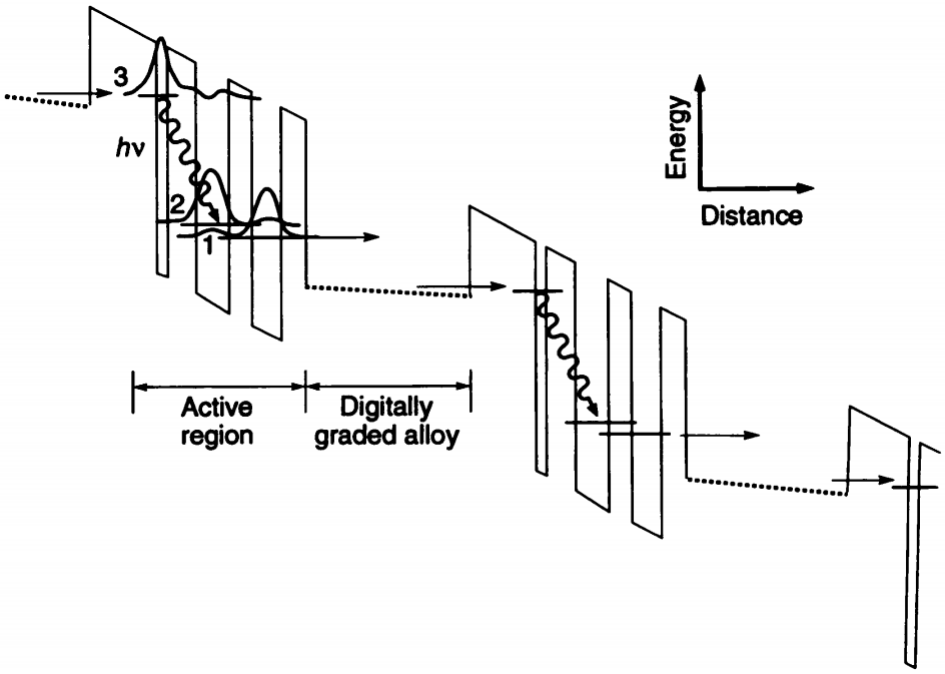

Figure 2-5: **Original QCL design** Lasing takes place between levels 3 and 2, which are far off resonance with LO phonon emission (levels 2 and 1). Efficient injection into level 3 is achieved via a digitally graded alloy, which prevents escape to the continuum.

known as the "bound to continuum" design – is known for a broad gain spectra and low threshold current density.

The ability to achieve high-power radiation in such a compact design allow QCLs to be used outside academic settings. QCLs have direct applications in a variety of different scientific fields, from infrared spectroscopy to chemical sensing [32, 33]. However, both a physical and mathematical understanding of how electron arrange themselves in QCLs is critical in designing such devices.

2.2 Quantum cascade laser theory

Modeling observed behavior of QCLs can be handled at a variety of different complexities. The lowest order of complexity is treating the motion of electrons semiclassically, and ignoring all quantum mechanical effects. Simplistic models involve the use of rate equations that track the evolution of electrons though the QCL as populations

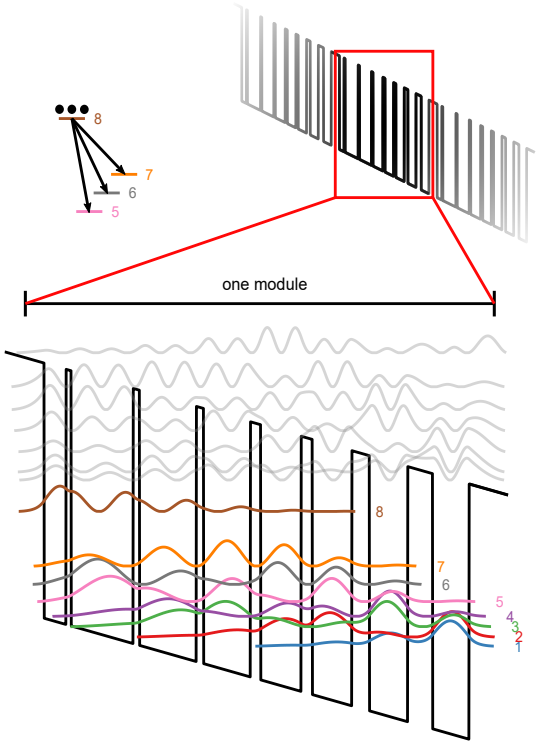

Figure 2-6: **Example Infrared QCL** A state-of-the-art QCL designed to lase at 11.5 μm.

of different subbands. These populations are solved for iteratively until a convergence condition is met. Alternatively, stochastic models, such as Monte Carlo, can also be used to solve for populations. This method has the advantage of not requiring the knowledge of the initial electron distribution to achieve convergence [34, 35].

The next level of complexity involves the use of density matrices. Density matrices allow one to calculate not only the semi-classical evolution of electrons, but the coherent evolution as well. The density matrix is evolved in time via the Liouville equation until all matrix elements have converged. This method is particularly adept at modeling tunneling through potential barriers, as the strength of tunneling is directly proportional to the coherent (or off-diagonal) elements of the density matrix [36].

The highest level of complexity is the Non-Equilibrium Green's Function (NEGF) approach. NEGF methods iteratively solve the Dyson and Keldysh equations for the retarded and lesser Green's functions. NEGF methods are completely quantum

mechanical and often take hours or days to reach convergence; however, they are the most robust and offer the most realistic predictions as compared to experiments. The reader is directed towards Jirauschek's and Kubis' review article on modeling techniques for QCLs for additional details [37].

By far, the most important aspect to all of the aforementioned simulations techniques is the band structure of a QCL. Without proper calculation of the electronic levels, simulations will produce non-sensible results [38]. Therefore, it is worth discussing how calculations of band structure are made, starting from simple III-V semiconductors and heterostructures, to practical implementations in a so-called "Schrödinger-Poisson solver".

2.2.1 Band structure calculations of III-V semiconductors

For bulk materials, such as III-V semiconductors, each electron eigenstate, $\Psi(\mathbf{r})$, must satisfy the Schrödinger equation [39],

$$\left(\frac{\mathbf{p}^2}{2m_0} + V(\mathbf{r}) + \frac{\hbar}{4m_0^2c^2}(\sigma \times \nabla V) \cdot \mathbf{p}\right)\Psi(\mathbf{r}) = E\Psi(\mathbf{r}), \tag{2.1}$$

where $\mathbf{p} = -i\hbar\nabla$ is the momentum operator, m_0 is the free electron mass, $V(\mathbf{r})$ is the potential of the lattice, c is the speed of light in a vacuum, and E is the energy associated with the electron electron eigenstate. The complexities of 2.1 are drastically simplified by noting that $V(\mathbf{r})$ is periodic over the entirety of the material. Therefore, Bloch's theorem is applied. $\Psi(\mathbf{r})$ can be written as

$$\Psi_{n,\mathbf{k}}(\mathbf{r}) = \frac{1}{\sqrt{N}}e^{i\mathbf{k}\cdot\mathbf{r}}u_{n,\mathbf{k}}(\mathbf{r}), \tag{2.2}$$

where N is the number of unit cells that divide the material and $u_{n,\mathbf{k}}(\mathbf{r})$ is called the Bloch function. The indices on Bloch function represent the band index n and the crystal momentum $\mathbf{k}$, which are restricted to the first Brillouin zone ($|\mathbf{k}| \leq \pi/a$, where a is the lattice constant). This restriction causes the Bloch function to have the same periodicity as the lattice, i.e. $u_{n,\mathbf{k}}(\mathbf{r}) = u_{n,\mathbf{k}}(\mathbf{r} + \mathbf{R})$. Combining 7.8 and 2.1, one

can arrive at a new Schrödinger equation with periodicity $\mathbf{R}$. Ignoring spin-orbital coupling, the new Schrödinger equation is given by

$$\left(\frac{\mathbf{p}^2}{2m_0} + V(\mathbf{r}) + \frac{\hbar}{m_0}\mathbf{k}\cdot\mathbf{p} + \frac{\hbar^2|\mathbf{k}|^2}{2m_0} \right) u_{n,\mathbf{k}}(\mathbf{r}) = E_{n,\mathbf{k}} u_{n,\mathbf{k}}(\mathbf{r}), \tag{2.3}$$

where the red highlighted terms in 2.3 are independent of $\mathbf{k}$ (H_0) and the blue highlighted terms in 2.3 are $\mathbf{k}$-dependent ($W(\mathbf{k})$).

This reformed Schrödinger equation is the essence of the so-called $\mathbf{k}\cdot\mathbf{p}$ (k dot p) method. If the solution to 2.3 is known at a particular extrema in $\mathbf{k}$-space, ($\mathbf{k} = 0$, for example), solutions for finite values of $\mathbf{k}$ can be treated as perturbations to the $\mathbf{k}$-independent Hamiltonian:

$$\left(H_0 + W(\mathbf{k})\right) u_{n,\mathbf{k}}(\mathbf{r}) = E_{n,\mathbf{k}} u_{n,\mathbf{k}}(\mathbf{r}), \tag{2.4}$$

where

$$H_0 u_{n,\mathbf{0}}(\mathbf{r}) = E_{n,\mathbf{0}} u_{n,\mathbf{0}}(\mathbf{r}), \tag{2.5}$$

In other words, $u_{n,\mathbf{0}}(\mathbf{r})$ is used as a basis expansion to find wavefunctions and energies for finite values of $\mathbf{k}$. The second order correction to the energy of $u_{n,\mathbf{k}}(\mathbf{r})$, $E_{n,\mathbf{k}}$ is given by

$$E_{n,\mathbf{k}} = E_{n,\mathbf{0}} + \frac{\hbar^2|\mathbf{k}|^2}{2m_0} + \frac{\hbar^2}{m_0^2}\sum_{m\neq n} \frac{|\langle u_{n,\mathbf{k}}|\mathbf{k}\cdot\mathbf{p}|u_{m,\mathbf{k}}\rangle|^2}{E_{n,\mathbf{0}} - E_{m,\mathbf{0}}}. \tag{2.6}$$

Therefore, evaluation of 2.6 requires knowledge of the matrix elements $|\langle u_{n,\mathbf{k}}|\mathbf{k}\cdot\mathbf{p}|u_{m,\mathbf{k}}\rangle|$ for different bands, hence the name $\mathbf{k}\cdot\mathbf{p}$. The Bloch functions are expanded to finite $\mathbf{k}$ in a similar manner.

In principle, the more bands involved in the summation in 2.6, the more accurate the energy correction will be. However, Kane [40] noted that only a few bands needed to be considered to achieve accurate energy corrections using $\mathbf{k}\cdot\mathbf{p}$ around $\mathbf{k} = 0$ (Γ

point),

$$u_{n,\mathbf{k}}(\mathbf{r}) = \sum_m c_m^{(n)}(\mathbf{k}) u_{m,\mathbf{0}}(\mathbf{r}). \tag{2.7}$$

Here, $c_m^{(n)}$ are coefficients to the basis expansion which depend on the band index n and the total number of bands considered. Kane found that only 8 bands needed to be considered (Fig. 2-7): two conduction bands and 6 valence bands (light-hole, heavy-hole and split-off). There are four unique bands near the Γ point, and the factor of 2 comes from spin-degeneracy. The conduction band is separated by the light hole and heavy hold valance bands by the bandgap energy, E_g, and the split-off band is further separated by Δ_0. Both of which are well-known material parameters.

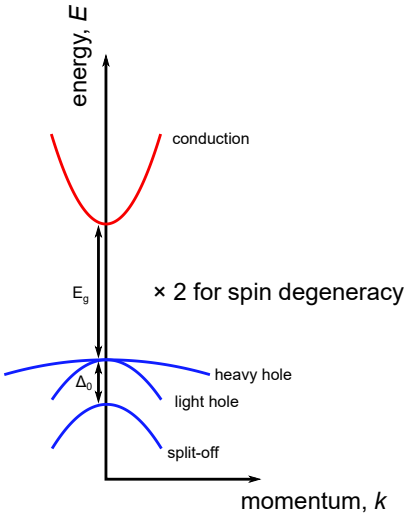

Figure 2-7: **Dispersion of electronic band** The bands Kane found to be significant near the Γ point: the conduction band, the heavy hole band, the light hole band and split-off band.

The contribution of each of the 8 bands to the total Hamiltonian can be formulated into an 8×8 matrix-eigenvalue problem whose solutions (eigenvalues) are the dispersion relation for the band of interest:

$$\mathsf{H}(\mathbf{k}) u_{n,\mathbf{k}}(\mathbf{r}) = E_n(\mathbf{k}) u_{n,\mathbf{k}}(\mathbf{r}), \tag{2.8}$$

where $\mathsf{H_{nm}}(\mathbf{k}) = \langle u_{n,\mathbf{0}}|H_0 + W(\mathbf{k})|u_{m,\mathbf{0}}\rangle$. $\mathsf{H}(\mathbf{k})$ is analytically cumbersome to manipulate, but well-posed numerically. Matrix-based programming languages such as MATLAB can handle large matrices, such as $\mathsf{H}(\mathbf{k})$, quite easily.

2.2.2 Envelope function approximation

The methods described in 2.2.1 work well for bulk semiconductors where the symmetry is maintained throughout the crystal. However, when the crystal periodicity is broken (as with any heterostructure), these methods break down. In order to rectify this, the envelope function approximation is applied.

Consider an imperfect crystal such that its periodicity is not maintained over the entire lattice. The electronic states can be written as a superposition of Bloch states at finite $\mathbf{k}$. Invoking 2.7, the Bloch states themselves can also been written as a superposition of Bloch states around $\mathbf{k} = 0$,

$$\Psi(\mathbf{r}) = \sum_{n,\mathbf{k}} a_n(\mathbf{k}) e^{i\mathbf{k}\cdot\mathbf{r}} u_{n,\mathbf{k}}(\mathbf{r}) = \sum_{\mathbf{k}} e^{i\mathbf{k}\cdot\mathbf{r}} \left(\sum_{m=1}^{8} c_m(\mathbf{k}) u_{m,\mathbf{0}}(\mathbf{r}) \right), \tag{2.9}$$

where the $a_n(\mathbf{k})$'s were absorbed into $c_m(\mathbf{k})$. Rearranging 2.9, one finds

$$\Psi(\mathbf{r}) = \sum_{m=1}^{8} \left(\sum_{\mathbf{k}} c_m(\mathbf{k}) e^{i\mathbf{k}\cdot\mathbf{r}} \right) u_{m,\mathbf{0}}(\mathbf{r}). \tag{2.10}$$

The terms in the parentheses of 2.10 are slowly-varying envelope functions with respect to primitive lattice, which one can denote $f_m(\mathbf{r})$. It should be stated that the only approximations made thus far are that of Bloch's theorem and Kane's perturbative use of $\mathbf{k}\cdot\mathbf{p}$. In the limit of considering an infinite number of bands, 2.10 is exact [41].

Suppose a slowly-varying (again, compared to the primitive lattice) potential $\phi(\mathbf{r})$ is added to the Hamiltonian to model imperfections in the crystal,

$$(H_0 + W(\mathbf{k}) + \phi(\mathbf{r}))\Psi(\mathbf{r}) = E\Psi(\mathbf{r}). \tag{2.11}$$

By subbing 2.10 into 2.11 and making use of some identities of slowly-varying functions [42], one can show that

$$(\mathsf{H}(-\mathsf{i}\nabla) + \phi(\mathbf{r}))\,\mathbf{F}(\mathbf{r}) = E\mathsf{I}\mathbf{F}(\mathbf{r}), \tag{2.12}$$

where $\mathbf{F}(\mathbf{r})$ is vector containing all of the envelopes and I is the identity matrix. 2.12 is a modified Schrödinger equation for the imperfect crystal, now acting on the slowly-varying envelopes instead of the full wavefunctions. 2.12 is often known as the *effective mass theorem* as the complexities of the lattice are modeled as position-dependent *effective* material parameters. To demonstrate this, consider a simple heterostructure consisting of two materials, A and B, where the transition from material A to B occurs at r', as shown in Fig. 2-8.

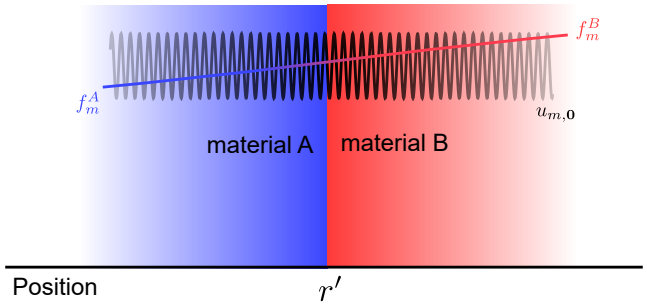

Figure 2-8: **Effective mass theorem** A simple heterostructure to demonstrate the significance of the effective mass theorem. The slowly-varying envelopes are shown by the red and blue curves, while the Bloch function is shown by the rapidly-varying black curve.

Several key assumptions are made in Fig. 2-8. The first assumption is that of 2.10; the total wavefunction in each layer can be written as expansion of 8 Bloch functions at the Γ point, with slowly varying envelopes (denoted by the blue/red curves),

$$\Psi(\mathbf{r}) = \sum_{m=1}^{8} f_m^{(\mathrm{A/B})}(\mathbf{r}) u_{m,\mathbf{0}}^{(\mathrm{A/B})}(\mathbf{r}). \tag{2.13}$$

The second key assumption is the Bloch amplitudes (denoted by the black curve) are

identical in both materials,

$$u^{(\mathrm{A})}_{m,\mathbf{0}}(\mathbf{r}) = u^{(\mathrm{B})}_{m,\mathbf{0}}(\mathbf{r}). \tag{2.14}$$

This second assumption is much more significant, and was key in eliminating the Bloch functions in 2.12. All microscopic details of the lattice have vanished, and the characteristic equation for the system only involves the slowly-varying envelopes.

The Hamiltonian for the system in Fig. 2-8 is given by

$$\mathsf{H}(-\mathsf{i}\nabla)\mathbf{F}(\mathbf{r}) = \left\{\mathsf{H}_{\mathrm{A}}(-\mathsf{i}\nabla)(1-\Theta(\mathbf{r}-\mathbf{r}')) + \mathsf{H}_{\mathrm{B}}(-\mathsf{i}\nabla)\Theta(\mathbf{r}-\mathbf{r}')\right\}\mathbf{F}(\mathbf{r}) = E\mathbf{F}(\mathbf{r}), \tag{2.15}$$

where $\Theta(\mathbf{r}-\mathbf{r}')$ is the Heaviside step function. The material interface in the effective mass approximation simply creates position-dependent Hamiltonian matrices, $\mathsf{H}_{\mathsf{i}}(-\mathsf{i}\nabla)$, that "turn on" in the presence of material i. The matrix elements, $\mathsf{H}_{\mathsf{nm}}(-\mathsf{i}\nabla)$, can be shown [39] to be

$$\left[E^{(A)}_{n,0} + V_{n,0}(\mathbf{r}) - \frac{\hbar^2\nabla^2}{2m_0}\right]\delta_{n,m} - \frac{i\hbar}{m_0}\langle u_{n,\mathbf{0}}|\mathbf{p}|u_{m,\mathbf{0}}\rangle\nabla - \frac{\hbar^2}{2}\sum_{\alpha,\beta}\frac{\partial}{\partial\alpha}\frac{1}{M^{\alpha\beta}}\frac{\partial}{\partial\beta}. \tag{2.16}$$

Here, the red highlighted terms represent *effective* band offsets as a function of position. The function $V_{n,0}(\mathbf{r})$ is defined such that in material A, $V_{n,0}(\mathbf{r}) = 0$ and in material B, $V_{n,0}(\mathbf{r}) = E^{(B)}_{n,0} - E^{(A)}_{n,0}$. The blue highlighted terms represent *effective* interband matrix elements, defined such that

$$\langle u_{n,\mathbf{0}}|\mathbf{p}|u_{m,\mathbf{0}}\rangle = \int_{\Omega_0} d^3\mathbf{r}\left\{u^*_{n,\mathbf{0}}\mathbf{p}u_{m,\mathbf{0}}\right\}, \tag{2.17}$$

where Ω_0 is the unit cell of the host material. Finally, the green highlighted terms represent elements of the *effective* mass tensor, where the indices α and β are over x, y, z.

At this point, all rapidly varying phenomena have disappeared from the equation of motion and are replaced with *effective* parameters. These parameters are (in

principle [43]) well established and drastically simplify solving 2.15. Despite this, 2.15 is still quite daunting. Luckily, some simplifications that apply to QCLs (and other intersubband devices) reduce the dimensionality of the Hamiltonian even further.

2.2.3 Three-band $\mathbf{k} \cdot \mathbf{p}$ model

QCLs are made of alternating bi-layers of atomically thin materials. The growth of these bi-layers is one (z) direction. The variation in the other two directions (x and y) occurs on lengths scales on the order of mm or μm; therefore, they can be ignored. Thus, the envelope functions can be assumed to have the following form:

$$\mathbf{F}(\mathbf{r}) = \frac{1}{\sqrt{A}} e^{i(k_x x + k_y y)} \mathbf{F}_{k_x,k_y}(z). \tag{2.18}$$

Furthermore, solutions to 2.12 are usually desired at the Γ point, therefore $k_x, k_y = 0$ and $-i\nabla \longrightarrow -i\frac{\partial}{\partial z}$. These simplifications have profound effects on the matrix Hamiltonian. First of all, the two spin degeneracies completely decouple from one another (8×8 to 4×4) and the heavy hole band decouples from the remaining three bands, leaving only the conduction band, the light hole band and the split-off band (4×4 to 3×3). The resulting Hamiltonian matrix equation is given by

$$\begin{pmatrix} -\frac{\hbar^2}{2m_0}\frac{\partial^2}{\partial z^2} + E_{\mathrm{c}}(z) & \sqrt{\frac{2}{3}}\frac{p_{\mathrm{cv}}}{m_0}p_z & -\sqrt{\frac{1}{3}}\frac{p_{\mathrm{cv}}}{m_0}p_z \\ \sqrt{\frac{2}{3}}\frac{p^*_{\mathrm{cv}}}{m_0}p_z & -\frac{\hbar^2}{2m_0}\frac{\partial^2}{\partial z^2} + E_{\mathrm{lh}}(z) & 0 \\ -\sqrt{\frac{1}{3}}\frac{p^*_{\mathrm{cv}}}{m_0}p_z & 0 & -\frac{\hbar^2}{2m_0}\frac{\partial^2}{\partial z^2} + E_{\mathrm{so}}(z) \end{pmatrix} \begin{pmatrix} f_{\mathrm{c}} \\ f_{\mathrm{lh}} \\ f_{\mathrm{so}} \end{pmatrix} = E \begin{pmatrix} f_{\mathrm{c}} \\ f_{\mathrm{lh}} \\ f_{\mathrm{so}} \end{pmatrix}, \tag{2.19}$$

where the eigenvector of the Hamiltonian, $\mathbf{F}$, contains the envelopes for all three bands. The free electron terms on the diagonal of the matrix can be shown to be on the order of $(E_{\mathrm{c}} - E_{\mathrm{lh}})/E_{\mathrm{p}}$, where $E_{\mathrm{p}} = \frac{2}{m_0}|p_{\mathrm{cv}}|^2$ is known as the Kane energy. The Kane energy is on the order of 20 eV, while $E_{\mathrm{c}} - E_{\mathrm{lh}}$ is typically on the order of 1 eV. Hence, these terms can be ignored. In addition, the light hole and heavy hole bands are not coupled, so their contribution to the conduction band are considered separately. This

is convenient as the states of interest for QCLs lie within the conduction band. The conduction band envelope can be found by solving,

$$-\frac{\hbar^2}{2}\frac{\partial}{\partial z}\frac{1}{m_0}\left[\frac{2}{3}\frac{E_\mathrm{p}}{E-E_\mathrm{lh}(z)}+\frac{1}{3}\frac{E_\mathrm{p}}{E-E_\mathrm{so}(z)}\right]\frac{\partial}{\partial z}f_\mathrm{c}+E_\mathrm{c}(z)f_\mathrm{c}=Ef_\mathrm{c}. \tag{2.20}$$

This is the power of the effective mass theorem; all complications involved in modeling the states of a QCL come down to solving the one-dimensional Schrödinger equation,

$$-\frac{\hbar^2}{2}\frac{\partial}{\partial z}\frac{1}{m^*(E,z)}\frac{\partial}{\partial z}f_\mathrm{c}=(E-E_\mathrm{c}(z))f_\mathrm{c}, \tag{2.21}$$

with an energy and position dependant effective mass, calculated as $m^*(E,z) = m_0\left[\frac{2}{3}\frac{E_\mathrm{p}}{E-E_\mathrm{lh}(z)}+\frac{1}{3}\frac{E_\mathrm{p}}{E-E_\mathrm{so}(z)}\right]^{-1}$. The energy dependence of the effective mass is called "non-parabolicity". For large values of $\mathbf{k}$, the parabolic approximation for subbands breaks down and the influence of other bands (such as the valence bands) must be considered. This reduces the curvature of the subband, ultimately increases the effective mass for higher energy electrons. 2.21 is well-posed numerically, and can be solved using a number of different standard techniques (see Appendix A).

2.2.4 Example QCL design

Fig. 2-9 shows the single module bandstructure for an example QCL used in this thesis. This dual-stack design, which lases at 8.2 μm, was designed by the ETH group [44]. The wafer index is A1182. The lasing transition for both stacks occurs between 3 and 2.

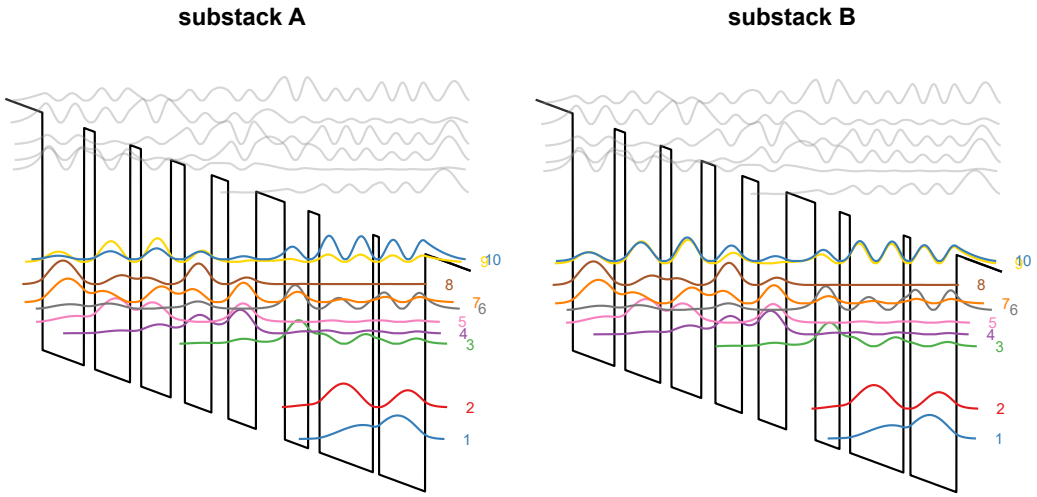

Figure 2-9: **ETH dual-stack design** The bandstructure for one of the primary QCLs (A1182) used in this thesis found by solving 2.21. This design consists of two lasing stacks (substack A and substack B). The designs are (in angstroms) A($In_{0.5918}Ga_{0.4082}As/In_{0.36}Al_{0.64}As$): 44.9, 11.7, **37.9, 11.9, 32.3**, 15, 28.9, 17.9, 30.1, 31.0, 25.2, 12.3, 57.7, 6.4, 50, 9.1, B($In_{0.5918}Ga_{0.4082}As/In_{0.36}Al_{0.64}As$): 44.9, 11.7, **37.9, 11.9, 32.3**, 15, 28.9, 17.9, 30.1, 31.0, 26.2, 11.3, 57.7, 7.4, 50, 9.1. Bold denotes doped regions.

Chapter 3

Fabrication and Experimental Methods

All of the QCL active regions shown in this thesis were grown by Thorlabs Quantum Electronics (TQE) using state-of-the-art MBE and MOCVD techniques. The majority of the active regions were also designed in-house by TQE, with the exception of a few well-established literature designs [44]. This was done to ensure the QCLs operate in the LWIR atmospheric transmission window (8 μm - 12 μm) for peak comb-spectrometer performance. The custom QCL designs are trade secrets, so the exact band-structures are unknown. Despite this, information on growth substrate, waveguide cladding and doping are given, which greatly assist in the fabrication of QCL ridges.

This chapter outlines the process involved in fabricating QCLs from raw wafers. Both wet and dry etching recipes are presented, detailed simulations on QCL thermal performance are conducted and basic QCL measurement techniques are discussed.

3.1 Fabrication processes

The author is indebted to Tianyi Zeng for the fabrication of the devices presented in this thesis. The fabrication process discussed in this section is the culmination of years of optimization and testing by Tianyi Zeng [45]. Therefore, such credit should

go to him. Further details of the fabrication flow can be found in [45].

3.1.1 Raw wafers

Raw wafers are grown on two inch InP substrates via MOCVD or MBE. A wafer cross-section with typical doping values and layers thicknesses is shown in Fig. 3-1. The top and bottom cladding regions act as a dielectric waveguide for light produced in the active region. These thicknesses change from growth to growth, but are typically 3.5 - 6 μm thick. Most IR-QCLs are grown using $In_{53}Ga_{47}As/In_{52}Al_{48}As$ heterostructures (although slight deviations are common). This material system has proven to be the most versatile and reliable in growing high-power lasers. In addition, the comparatively high refractive index of $In_{53}Ga_{47}As/In_{52}Al_{48}As$ (3.5) compared to InP (3.1) leads to excellent modal confinement. It should be noted that the highly-doped plasmon layer is not grown on all wafers.

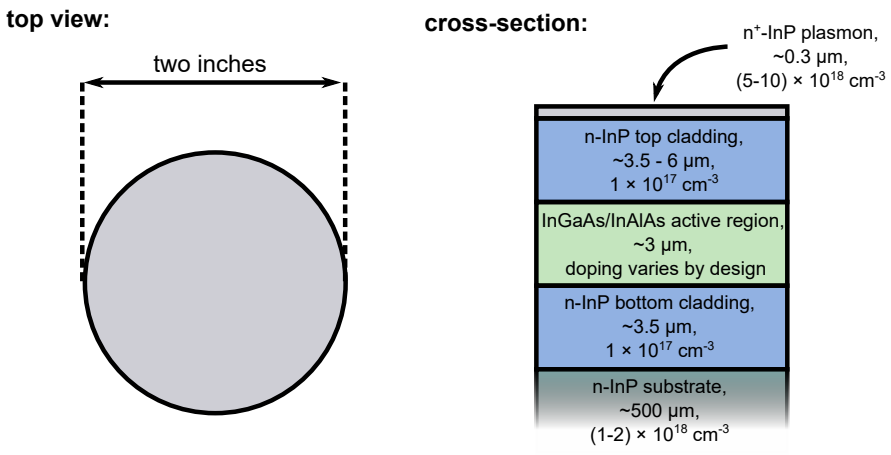

Figure 3-1: **QCL wafer** Typical doping values and layer thicknesses are shown.

3.1.2 Fabrication flow

Before the wafers can be fabricated into QCL ridges, they must be cleaved into 1 cm $\times$ 1.5 cm pieces and cleaned via piranha to ensure no organic residue remains on the surface of the wafer. A typical QCL ridge fabrication flow-chart is shown in Fig. 3-2.

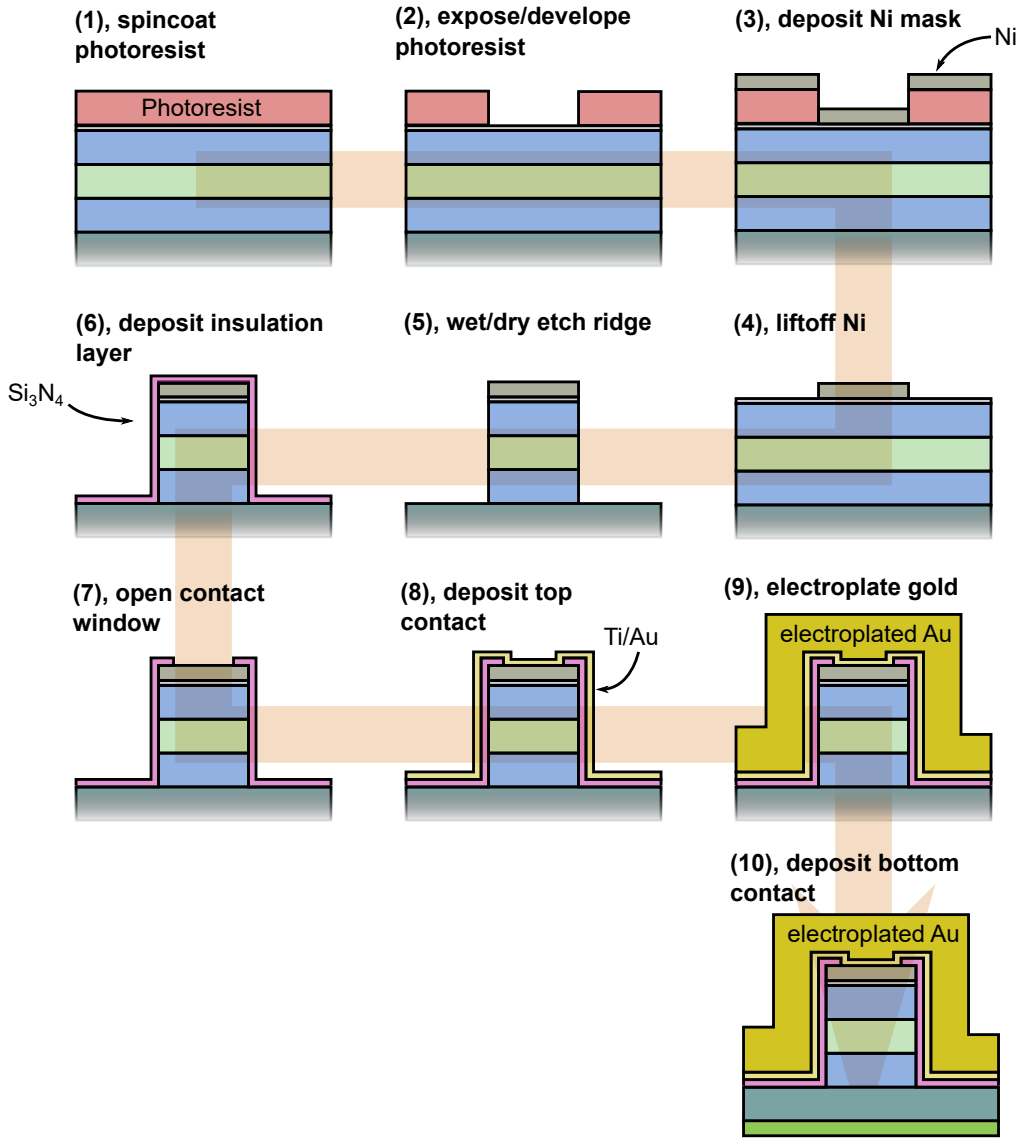

Figure 3-2: **Example fabrication flow** Major steps include hard mask definition **(1-4)**, ridge etching **(5)**, top contact definition **(6-8)**, Au electroplating **(9)**, and back-side metalization **(10)**.

The first several steps **(1-4)** of the fabrication flow define the top metal/hard mask for the etching process. Standard photo techniques based on both electron-beam (e-beam) lithography and optical lithography are utilized. Ni is highly resistant to chemical etch, which makes it an ideal etch mask.

The laser ridge is then defined by either plasma-based etching (dry-etch) or wet chemical based etching (wet-etch) **(5)**. Most QCLs ridges throughout history have

been defined via wet-etch and this thesis is no exception. QCLs were etched in a solution of $HBr/HCl/H_2O_2/H_2O$ (ratios of 50/25/10/200) to a depth of 12-15 μm and a width of 8-15 μm. These thicknesses are chosen to ensure the waveguide only supports the fundamental lasing mode. Fortunately, all grown materials (InP, InGaAs, InAlAs) have a uniform etch rate, leading to a smooth etch profile. However, wet-etching is *isotropic*, meaning the solution etches the material in all directions at the same rate. As a result, ridges have significant curvature, which leads to current spreading. On the other hand, dry-etching has the advantage of being almost completely *anisotropic* due to the highly-directional nature of plasma-based etching techniques. QCLs were dry-etched using a mixture of $Cl_2/BCl_3/SiCl_4/Ar$. Unfortunately, dry-etching can often leave rough etched surfaces and "grass", so process parameters must be finely adjusted to minimize adverse etching effects.

Steps **(6-8)** define the top contact for the device. First, an insulation layer (Si_3N_4) is deposited using plasma-enhanced chemical vapor deposition (PECVD). This ensures high film quality, and reduces the likelihood of dielectric breakdown. Then, a window is opened in the insulation layer using standard photo/etching techniques, and the top contact of Ti/Au is deposited.

The Ti/Au layer also serves as a base layer for Au electroplated **(9)**. Several μms of gold are electroplated around the ridge to improve heat removal from the active region.

Finally, a back-side contact is deposited **(10)**. Either an annealed sequence of Ge/Au/Ni/Au or Ti/Au is used.

This fabrication flow is completely general and the methods can (in theory) be applied to a different sorts of QCL geometries. Specifically, it is advisable to etch QCLs in a so-called "double-channel" geometry. Rather than etching away all material in **(5)**, leaving only the ridge, the QCL is etched in a trench. Double-channel geometry ensures greater structural stability of the top surface of the ridge, which greatly assist in device bonding.

It is also important to note that this is *not* the only way to fabricate IR QCLs, *nor is the most effective*. Rather than depositing an insulation layer, as in **(6)**, modern

IR QCLs fabrications flows use the regrowth of Fe doped InP to serve as both an insulating layer and a heat removal layer. However, regrowth of Fe:InP is both time-consuming and expensive, thus this method could not be utilized. A cross-sectional image of two QCL ridges (one dry-etched, one wet-etched) is shown in Fig. 3-3

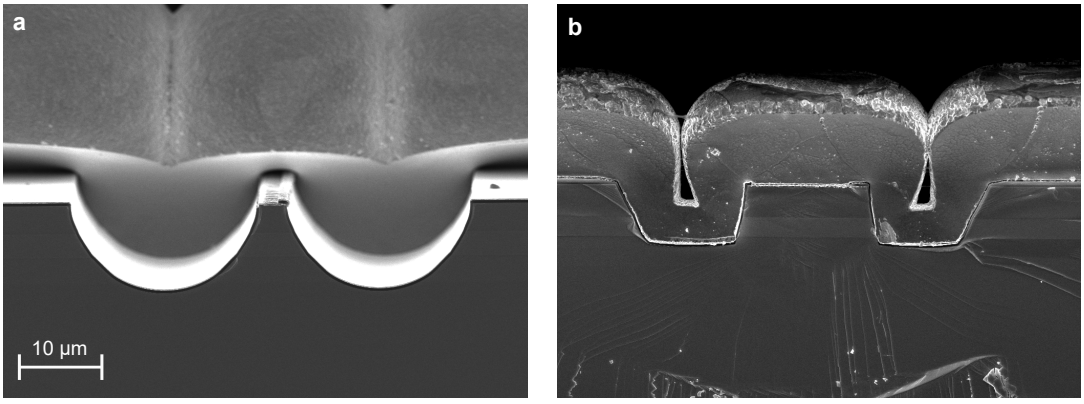

Figure 3-3: **Example device fabrication** SEM images of a QCL defined by (a) wet-etch and (b) dry etch.

3.1.3 Mounting techniques

The mounting process is a critical step in ensuring both a stable electrical contact and efficient heat removal from the device. There are two main types of mounting technique: *epi-up* mounting, which means mounting the laser epitaxial-side upwards on a mount, and *epi-down* mounting, which means mounting the laser epitaxial-side downwards on a mount. Both mounting techniques were utilized and both have their advantages and disadvantages.

Epi-up mounting is significantly easier than epi-down mounting. Once the QCLs have been fabricated, the devices facet's are cleaved (usually in a group of three ridges), and soldered onto a copper block using In foil as shown in Fig. 3-4 (a). Electrical connections to "chip-carriers" can either be made through Au wire bonds or In wire bonds.

Epi-down mounting, on the other hand, is more involved. Instead of directly bonding the dies to copper blocks, the lasers are first mounted on AlN sub-mounts

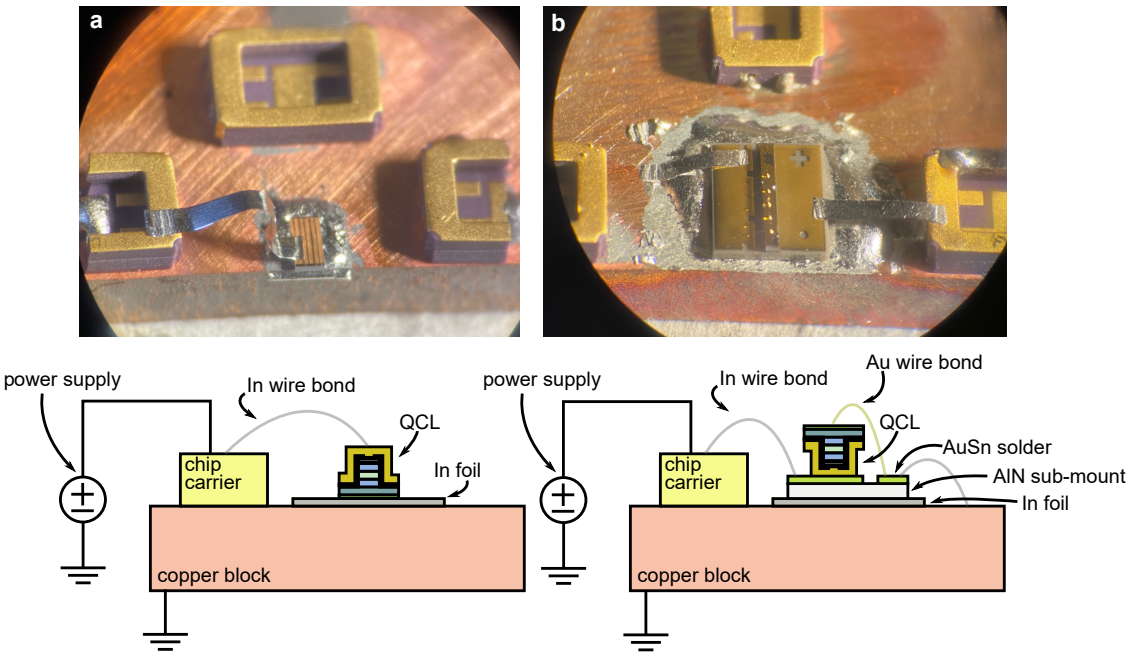

Figure 3-4: **QCL mounting techniques** Microscope images of devices mounted (a) epi-up and (b) epi-down. Cartoon schematics of wire connections are also shown.

covered in 6 μm of AuSn (80/20) solder. Then, the AlN sub-mount (along with the laser) are mounted on a copper block using In foil. Unlike with epi-up mounting, the laser must be grounded via wire connections. Cartoon schematics of wire connections are also shown in the bottom of Fig. 3-4.

The main advantage of epi-down mounting compared to epi-up mounting is heat removal. Fig. 3-5 details a COMSOL simulations of the estimated temperatures of a QCL under typical operating conditions for several mounting scenarios: epi-up mounting (a), epi-up mounting with a thinned substrate (b), epi-down mounting with a thinned substrate (c) and epi-down mounting (d). Thermal boundary conditions of 10 deg. C are defined via the blue lines. Reported ΔTs represent the temperature difference between the hottest portion of the active region and the boundary condition. This value is critical as the smaller ΔT is, the less likely the laser will cease operation due to thermal runoff or sustain permanent damage. There is a clear thermal advantage to epi-down mounting as compared to epi-up mounting, even when the substrate is thinned. It is important to note that thinning the substrate has no

effect on ΔT for epi-down mounting.

Once mounting is complete, the lasers are placed on a thermoelectric cooler (TEC) stabilized at 10 deg. Celsius, and are biased via an electrical connection to the chip carrier.

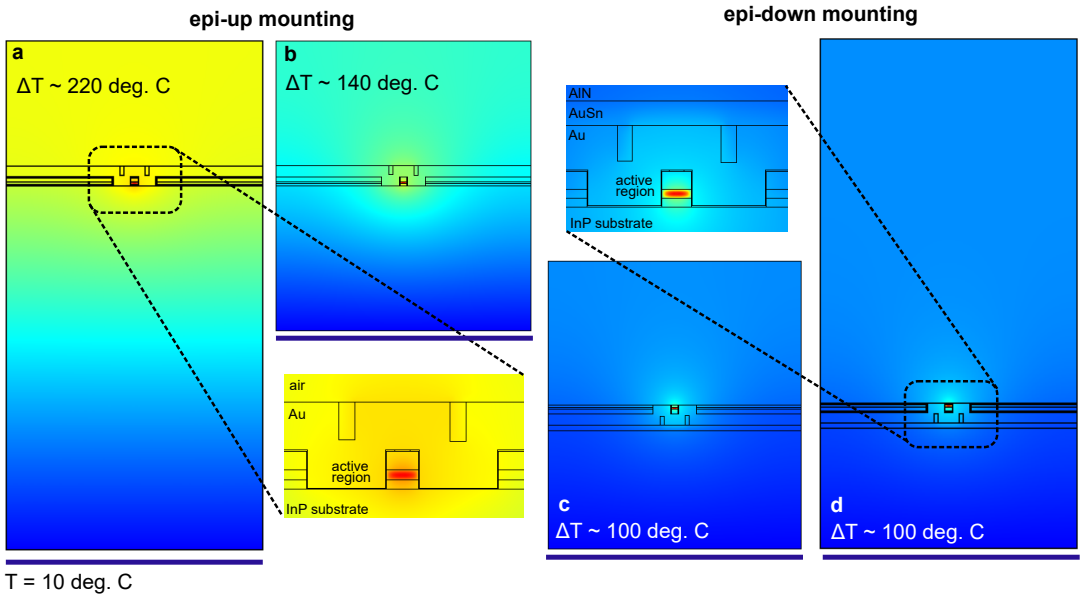

Figure 3-5: **Thermal simulation of mounting** COMSOL simulation of epi-up mounting with and without thinned substrates (a), (b), and epi-down mounting with and without thinned substrates (c), (d). QCL operation is simulated via a uniform heat source of 2.2×10^{14} W/m^3, which corresponds to current density of 4 kA/cm^2. The active region is 10 μm wide. Thermal conductivities of all materials are taken from [3].

3.2 Experimental methods

There are two main types of characterization methods to evaluate QCL performance: (1) an "IVL" measurement and (2) a spectrum measurement. An IVL measurement (current-voltage-light) involves biases the QCL with either a pulsed or CW voltage source while monitoring the current and light output using external detectors. A spectrum measurement involves shining the laser light into a Fourier Transform Infrared Spectrometer (FTIR) to measure the QCL's output frequencies.

3.2.1 IVL measurements

The QCLs in this thesis were typically biases either using an Avtech voltage pulser or a Keithley DC supply. Pulse widths can vary from 100 ns to 100 μs with duty cycles ranging from 0.1% to 10%. The current though the biases QCL is measured by an inductive current probe and the light output is monitored using a liquid nitrogen cooled Mercury-Cadmium-Telluride (MCT) detector. A typical IVL curve is shown in Fig. 3-6

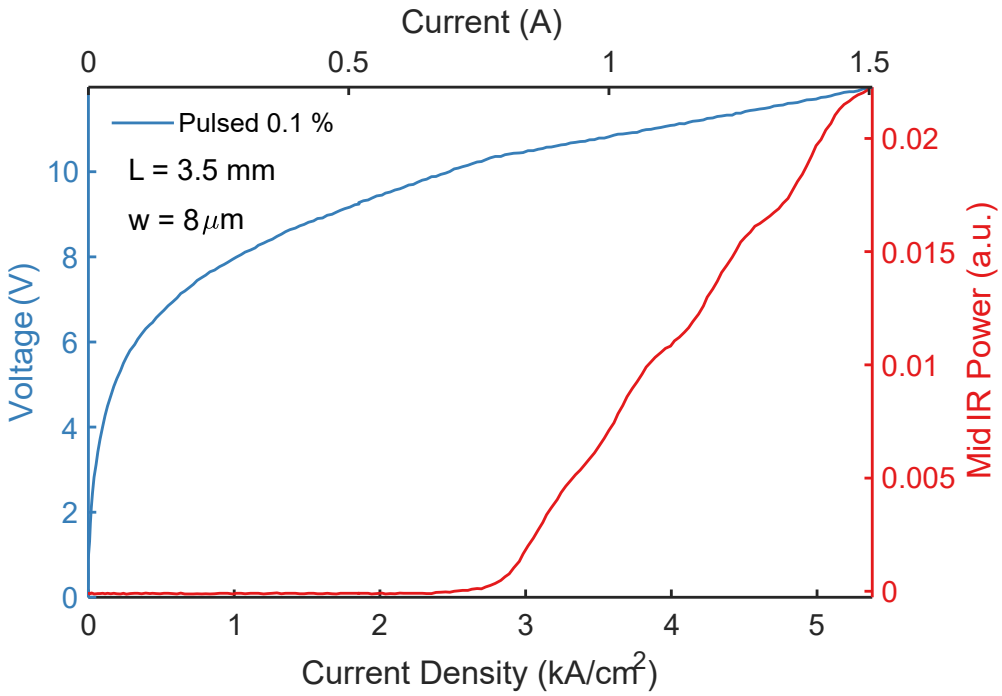

Figure 3-6: **Example IVL of QCL** The IV curve from wafer index A1182 is plotted in blue while the light output curve is plotted in red. The top x-axis is absolute current, while the bottom x-axis is current density.

The blue curve represents voltage and current, while the red curve represents light output. Current is typically plotted in both absolute terms (top x-axis) and in density terms (bottom x-axis). The onset of lasing is characterized by the sharp increase in light output. The current at which lasing begins is known as *threshold current*. Typical values for threshold current density range from 1.5 kA/cm^2 to 5 kA/cm^2. A low threshold is indicative of a high-quality laser ridge. On the other hand, high threshold does not necessarily imply the fabrication went ariy. Sometimes,

instabilities during the wafer growth process can prevent even the highest-quality ridges from lasing. Here, lasing begins at 2.8 kA/cm^2.

The onset of lasing also changes the IV curve. A strong "kink" is present above threshold, followed by a change in the slope of the IV curve. This change in slope models after the IV characteristics of a diode laser above threshold; the laser acts as a resistor with resistance equal to the contact resistance.

3.2.2 Spectrum measurements

The most effective way to measure the spectrum of any infrared source is to use an FTIR. Unlike other spectroscopy techniques, which split light into its different spectral components and measure the power associated with each line, an FTIR measures the *interferogram* of the source, which is directly related to the spectrum of the source via the Fourier transform. The schematic for the FTIR is shown in Fig. 3-7

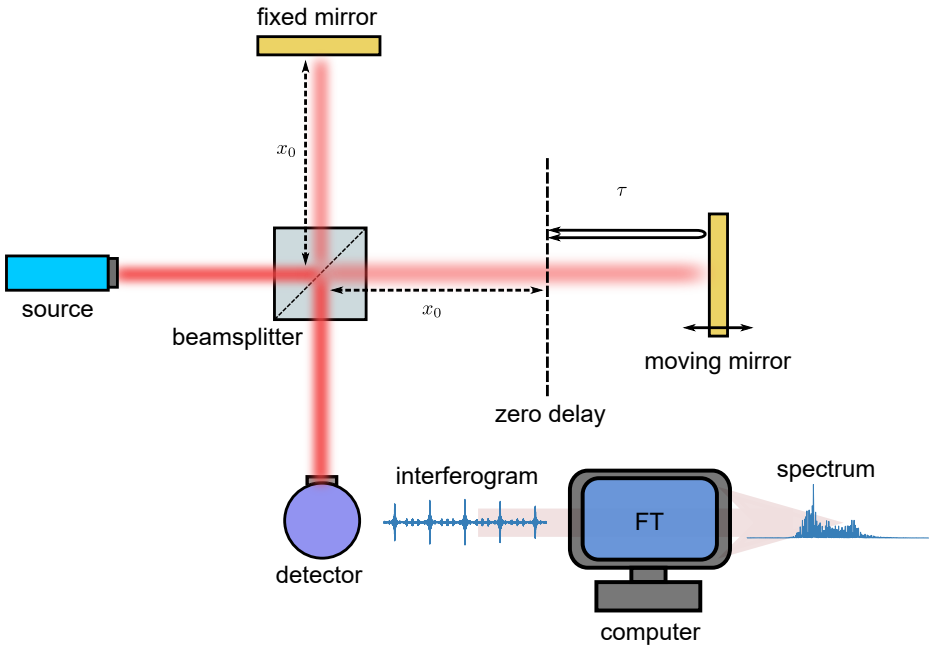

Figure 3-7: **Schematic of FTIR** The spectrum of a source is measured by interfering the source with itself at a variety of different delay positions. The Fourier transform of the interference patter—or interferogram—is the spectrum of the source convoluted with an apodization function.

At its core, the FTIR measures the time-domain power signal associated with

a source. It does this by first splitting the source into two equally-powered optical paths. Then, the FTIR delays one optical path in time by an amount τ using a computer-controlled mirror. The delayed path and original path are interfered with one another, and the resulting interference output power is measured as a function of delay. This signal is known as the interferogram.

In order to understand how the spectrum is extracted from the interferogram, consider the detector signal at time t for a certain delay τ,

$$P(t,\tau) = (E(t) + E(t-\tau))^2 \tag{3.1}$$

$$= E^2(t) + E^2(t-\tau) + 2E(t)E(t-\tau). \tag{3.2}$$

The first two terms, $E^2(t) + E^2(t-\tau)$, are the DC field intensities corresponding to each of the arms, while the last term, $2E(t)E(t-\tau)$, is the interference between the two arms. Ignoring the first two terms and the factor of two on the last term, the averaged output signal over a measurement duration T is given by,

$$\langle E(t)E(t-\tau)\rangle = \frac{1}{T}\int_0^T \mathrm{d}t\{E(t)E(t-\tau)\}, \tag{3.3}$$

otherwise known as the auto-correlation. This can also be represented by the integration over a boxcar measurement Kernel $K(t)$,

$$\langle E(t)E(t-\tau)\rangle = \int_{-\infty}^{\infty} \mathrm{d}t\{K(t)E(t)E(t-\tau)\}. \tag{3.4}$$

In addition, the finite stage delay is modeled through the multiplication of the averaged signal with an apodization function $A(\tau)$. Therefore, the output signal for a given delay τ is $S_0(\tau) = A(\tau)\langle E(t)E(t-\tau)\rangle$. The Fourier transform of the output signal is given by

$$S_0(\omega) = \int_{-\infty}^{\infty} \mathrm{d}\tau \left\{A(\tau)\langle E(t)E(t-\tau)\rangle\right\} e^{i\omega\tau}. \tag{3.5}$$

One can then invoke the convolution theorem:

$$a(t) = b(t) \cdot c(t) \Longleftrightarrow A(\omega) = B(\omega) * C(\omega), \tag{3.6}$$

and show

$$S_0(\omega) = A(\omega) * \int_{-\infty}^{\infty} \mathrm{d}\tau \left\{ \langle E(t)E(t-\tau) \rangle \right\} e^{i\omega\tau} \tag{3.7}$$

$$= A(\omega) * \int_{-\infty}^{\infty} \mathrm{d}\tau \left\{ \int_{-\infty}^{\infty} \mathrm{d}t \{ K(t)E(t)E(t-\tau) \right\} \tag{3.8}$$

$$= A(\omega) * \int_{-\infty}^{\infty} \mathrm{d}t \{ K(t)E(t) \} \int_{-\infty}^{\infty} \mathrm{d}\tau \left\{ E(t-\tau)e^{i\omega\tau} \right\}. \tag{3.9}$$

Using the change of variables $t' = t - \tau$, $S_0(\omega)$ becomes

$$S_0(\omega) = A(\omega) * \int_{-\infty}^{\infty} \mathrm{d}t \left\{ K(t)E(t)e^{i\omega t} \right\} \int_{-\infty}^{\infty} \mathrm{d}t' \left\{ E(t')e^{-i\omega t'} \right\}. \tag{3.10}$$

Several more simplifications can be made. One notes the convolution theorem can be applied to the first integral, resulting in $E(\omega) * K(\omega)$. Furthermore, $K(\omega)$ is a very narrowband function, which can be approximated as a delta function, $\delta(\omega)$. The second term is just the complex conjugate of the Fourier transform of the electric field, $E^*(\omega)$. The output signal of the FTIR (after applying the Fourier transform) is thus

$$S_0(\omega) = A(\omega) * [E^*(\omega) \cdot E(\omega) * \delta(\omega)] = A(\omega) * |E(\omega)|^2, \tag{3.11}$$

which is the spectrum of the source convolved with the apodization function.

The majority of spectral measurements were taken on a custom FTIR built by David Burghoff. This FTIR has a 30 cm interferometric stage, which corresponds to a spectral resolution of 0.033 cm^{-1} or 0.001 THz. An example interferogram and spectrum for a QCL is shown in Fig. 3-8

The zero-delay position is approximately 135 mm, with satellite interference peaks occurring every 15 mm. The relatively narrowband time-domain signal naturally leads

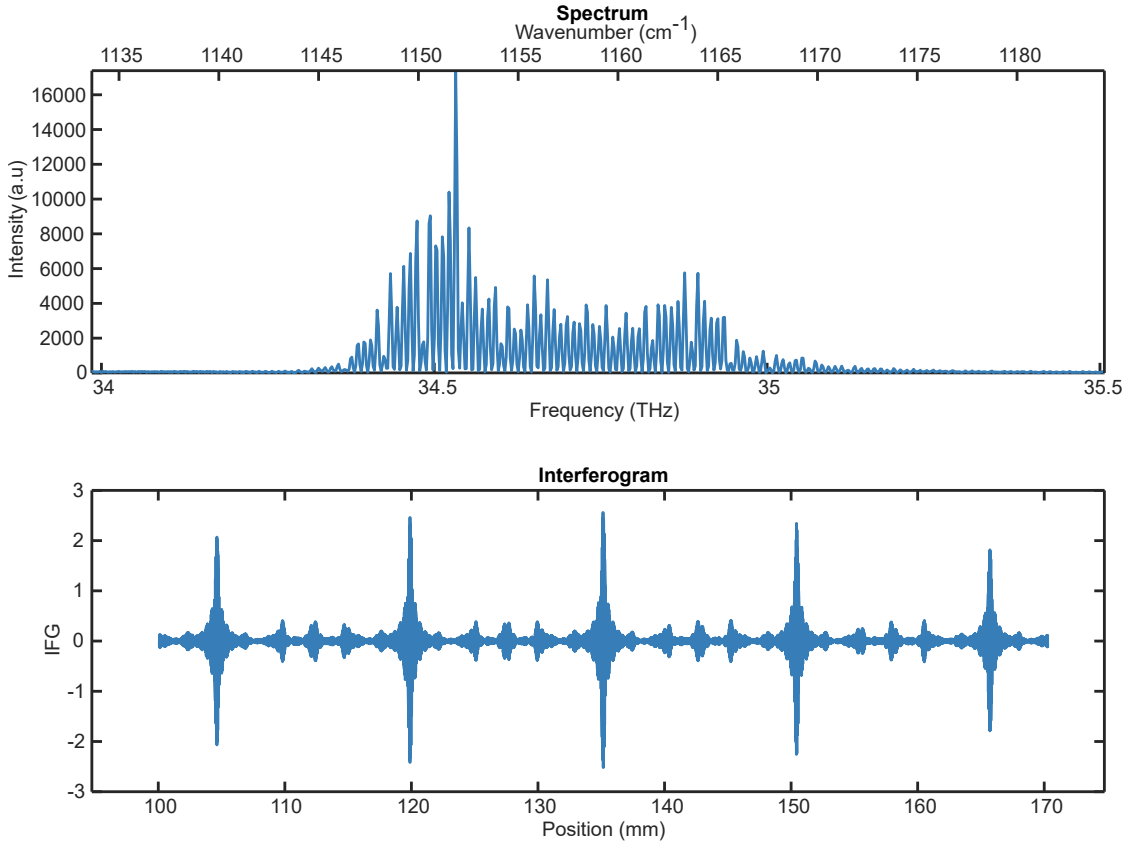

Figure 3-8: **Example interferogram and spectrum** The spectrum on the top panel is created by Fourier transforming the interferogram on the bottom panel. The interferogram has the center burst and four satellite bursts, two on each side of the center burst. The narrow peaks in the interferogram lead to a broad frequency spectrum.

to a broadband frequency spectrum, spanning 25 cm^{-1}.

Chapter 4

Frequency Comb Formation in Quantum Cascade Lasers

Frequency combs are broadband light sources with equally-spaced and phase coherent laser lines. They exist in a number of passive and active optical systems such as Kerr micro-resonators and mode-locked lasers. As alluded to in the previous chapter, Fabry-Pérot QCLs are naturally broadband devices, making them excellent candidates for frequency comb sources. With delicate balance of optical non-linearities and dispersion, the incoherent laser lines of a QCL can lock together, forming a strong, coherent frequency comb.

This chapter outlines the theory behind comb formation in QCLs, including discussions of the primary optical non-linearity involved in QCL comb: four-wave mixing. Different combs states are also discussed in the context of laser master equations, as well mean-field approaches.

4.1 Origins of comb generation

QCL frequency combs can exist in two geometries, ring-resonator geometries and a Fabry-Pérot geometries. Ring QCL frequency combs arise from phase turbulence that locks adjacent laser lines [46]. These combs have been shown to have wide dynamic range and can form so-called harmonic states, which skip every n comb lines

[47, 48, 49]. Although appealing from a physics standpoint, their low power-per-mode compared to Fabry-Pérot lasers makes them inadequate for spectroscopy. Therefore, the focus of this thesis is on Fabry-Pérot QCL combs.

All Fabry-Pérot combs start as a multi-mode lasers. Multi-mode lasing arises from spatial-hole burning (SHB), which is the spatially-dependent saturation of gain at the electric field anti-nodes inside the cavity. This gain saturation promotes competition between other cavity modes, and if these lines achieve sufficient gain, they also lase. The locking of these lines operate on similar principles to microresonator-based Kerr combs [50].

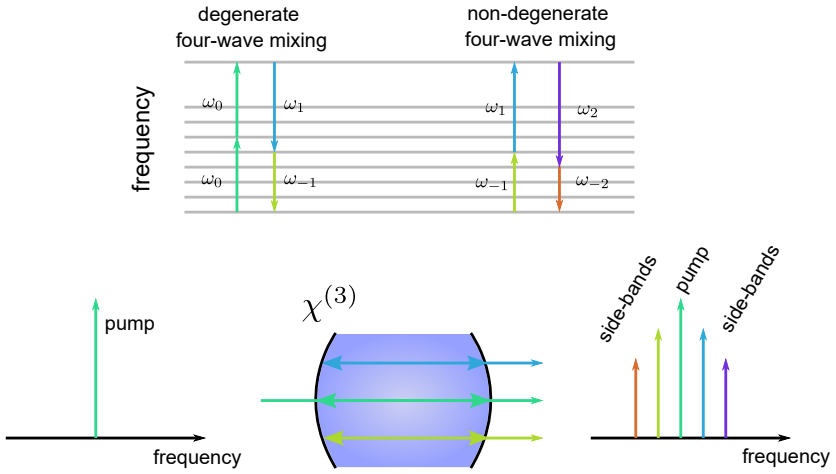

Figure 4-1: **Principles of Kerr-comb formation** An incident pump beam is split into sidebands via degenerate and non-degenerate four-wave mixing (FWM). This $\chi^{(3)}$ effect only occurs in high-Q cavities. This figure is adapted from [4]

In a Kerr microresonator, a strong pump line at frequency ω_0 is incident on a third-order nonlinear optical material ($\chi^{(3)}$ material) as depicted in Fig. 4-1. Under certain cavity conditions, degenerate four-wave mixing (FWM) split the pump line into two adjacent lines, ω_1 and ω_{-1}, which correspond to the pump frequencies neighboring cavity modes. Non-degenerate FWM further splits the lines into more adjacent sidebands, and the process continues until the sidebands do not have sufficient gain to lase.

4.1.1 Non-linear optical phenomena

Much of what follows is taken from [51] and [52]. These derivations and discussions are fundamental to the operation of QCL combs, and lay the ground-work for dispersion engineering, which will be discussed in the following chapter.

Maxwell's equations fully describe the propagation of electomagnetic waves in both vacuum and in media. In the absence of any sources, Maxwell's equations are

$$\nabla \cdot \mathbf{D} = 0 \tag{4.1}$$

$$\nabla \cdot \mathbf{B} = 0 \tag{4.2}$$

$$\nabla \times \mathbf{E} = -\frac{\partial \mathbf{B}}{\partial t} \tag{4.3}$$

$$\nabla \times \mathbf{H} = \frac{\partial \mathbf{D}}{\partial t}. \tag{4.4}$$

The electric field, $\mathbf{E}$, and the magnetic field, $\mathbf{H}$, are related to the so-called constitutive relations, $\mathbf{B} = \mu_0 \mathbf{H}$ and $\mathbf{D} = \epsilon_0 \mathbf{E} + \mathbf{P}$, by the magnetic permeability (μ_0), the electric permittivity (ϵ_0) and the polarization ($\mathbf{P}$). Furthermore, if one assumes the radiation can be described via plane waves, the electric and displacement fields can be related by a wave equation:

$$\nabla^2 \mathbf{E} = \frac{1}{c^2 \epsilon_0} \frac{\partial^2 \mathbf{D}}{\partial t^2}. \tag{4.5}$$

Next, it is common to write the polarization as a expansion of linear and non-linear terms:

$$\mathbf{P} = \mathbf{P}^{(1)} + \mathbf{P}^{\mathrm{NL}} \tag{4.6}$$

where $\mathbf{P}^{(1)}$ is the part of the polarization that scales linearly with the electric field, i.e. $\mathbf{P}^{(1)} = \chi^{(1)} \epsilon_0 \mathbf{E}$, and $\mathbf{P}^{\mathrm{NL}}$ scales to different powers of the electric field, i.e. $\mathbf{P}^{\mathrm{NL}} = \chi^{(2)} \epsilon_0 \mathbf{E^2} + \chi^{(3)} \epsilon_0 \mathbf{E^3} + ...$ One can now write 4.5 in terms of the non-linear

polarization by substituting $\mathbf{D} = \epsilon_0 n^2 \mathbf{E} + \mathbf{P}^{\mathrm{NL}}$, where $n^2 = 1 + \chi^{(1)}$,

$$\nabla^2 \mathbf{E} - \left(\frac{n}{c}\right)^2 \frac{\partial^2 \mathbf{E}}{\partial t^2} = \frac{1}{c^2 \epsilon_0} \frac{\partial^2 \mathbf{P}^{\mathrm{NL}}}{\partial t^2}. \tag{4.7}$$

In the limit that the non-linear polarization goes toward zero, 4.7 reduces to the original wave equation 4.5. Each non-linear optical process has an associated $\mathbf{P}^{\mathrm{NL}}$ term. Once $\mathbf{P}^{\mathrm{NL}}$ is known, 4.7 can be expanded to find the necessary conditions for the process to occur efficiently.

The non-linear fields can all be described by plane waves, which mean–dropping the vector notation–the electric field can be written as the product of a slowly-varying envelope function, $A_i(z)$, with an oscillatory term oscillating at ω_i with wavenumber k_i:

$$E_i(z,t) = \sum_i A_i(z) e^{i(k_i z - \omega_i t)} + \text{c.c.}, \tag{4.8}$$

where $k_i = \frac{n_i \omega_i}{c}$. One can then expand the left-hand side of 4.7 using 4.8 to find

$$\left| \nabla^2 \mathbf{E} - \left(\frac{n}{c}\right)^2 \frac{\partial^2 \mathbf{E}}{\partial t^2} \right| = \sum_i \left(\frac{\partial^2 A_i}{\partial z^2} + 2ik_i \frac{\partial A_i}{\partial z} \right) e^{i(k_i z - \omega_i t)}. \tag{4.9}$$

It is typical to ignore the first term in the parenthesis of 4.9 as it is much smaller than the second term. This is known as the slowly-varying amplitude approximation,

$$\left| \frac{\partial^2 A_i}{\partial z^2} \right| << \left| k_i \frac{\partial A_i}{\partial z} \right|. \tag{4.10}$$

Therefore, 4.9 can be written as

$$\left| \nabla^2 \mathbf{E} - \left(\frac{n}{c}\right)^2 \frac{\partial^2 \mathbf{E}}{\partial t^2} \right| = \sum_i 2ik_i \frac{\partial A_i}{\partial z} e^{i(k_i z - \omega_i t)}. \tag{4.11}$$

As stated previously, the goal is to find the evolution of the envelopes, A_i, undergoing different non-linear optical processes.

4.1.2 Four-wave mixing

The most important non-linear phenomena that occurs in QCL combs is FWM. This $\chi^{(3)}$ effect can be split into two separate processes: degenerate and non-degenerate FWM. Both are special cases of the general third-order non-linearity, which scales as the cube the electric field:

$$P^{\mathrm{NL}}(t) = \epsilon_0 \chi^{(3)} E(t)^3 \tag{4.12}$$

where

$$E(t) = \sum_i E_i e^{(i\omega_i t)} + \mathrm{c.c} \equiv \mathcal{E} + \mathcal{E}^*. \tag{4.13}$$

The non-linear polarization can then be expanded as

$$P^{\mathrm{NL}}(t) = \epsilon_0 \chi^{(3)} \left[\mathcal{E}^3 + (\mathcal{E}^*)^3 + 3\mathcal{E}^2\mathcal{E}^* + 3\left(\mathcal{E}^2\right)^* \mathcal{E} \right]. \tag{4.14}$$

The terms in red represent sum-frequency generation, as they do not have interactions between both the phasor and its conjugate, therefore, these terms are ignored. The remaining two terms are responsible for FWM and can be written as

$$P^{\mathrm{NL}}(t) = \epsilon_0 \chi^{(3)} \sum_{i,j,k} E_i E_j E_k^* e^{-i(\omega_i + \omega_j - \omega_k)t} + \mathrm{c.c.} \tag{4.15}$$

The physical significance of this expression is that in the presence of $\chi^{(3)}$ material, radiation at frequencies ω_i, ω_j, and ω_k will produce a non-linear polarization at $\omega_i + \omega_j - \omega_k$. Using 4.15 under the slowly-varying amplitude approximation, the right-hand

side of 4.7 is

$$\frac{1}{c^2\epsilon_0}\frac{\partial^2 P^{\mathrm{NL}}}{\partial t^2}. = 3\frac{\chi^{(3)}}{c^2}\frac{\partial^2}{\partial t^2}\left\{\sum_{i,j,k} E_i E_j E_k^* e^{-i(\omega_i+\omega_j-\omega_k)t} + \text{c.c.}\right\} \tag{4.16}$$

$$= 3\frac{\chi^{(3)}}{c^2}\frac{\partial^2}{\partial t^2}\left\{\sum_{i,j,k} A_i A_j A_k^* e^{i(k_i+k_j-k_k)z} e^{-i(\omega_i+\omega_j-\omega_k)t} + \text{c.c.}\right\} \tag{4.17}$$

$$= -3\frac{\chi^{(3)}}{c^2}\left\{\sum_{i,j,k} A_i A_j A_k^* \left(\omega_i+\omega_j-\omega_k\right)^2 e^{i(k_i+k_j-k_k)z} e^{-i(\omega_i+\omega_j-\omega_k)t}\right\} + \text{c.c.} \tag{4.18}$$

Equating 4.18 and 4.11 yields a partial differential equation whose solution dictates the evolution of the carrier envelope.

In the case of degenerate FWM, a pump frequency of ω_0 creates lines ω_1 and ω_{-1} such that $2\omega_0 = \omega_1 + \omega_{-1}$. Each term in 4.18 and 4.11 is separable from the other terms, therefore individual frequency components can be considered independently. For example, consider only radiation oscillating at ω_1 (the case for ω_{-1} is identical) under the conditions for degenerate FWM. 4.11 contributes only $i = 1$ to the sum and 4.18 contributes $(i, j, k) = (1, 1, 1)$ and $(i, j, k) = (0, 0, -1)$. One finds:

$$\frac{\partial A_1}{\partial z} = i\frac{3}{2}\frac{\chi^{(3)}\omega_1}{2nc}\left\{A_0 A_0 A_{-1}^* e^{i(2k_0-k_{-1}-k_1)z} + A_1|A_1|^2\right\}. \tag{4.19}$$

The first term inside the brackets has an important physical interpretation. The exponential can be interpreted as conservation of total momentum, also known as the phase matching condition. That is, if $2k_0 - k_{-1} - k_1 \neq 0$, then FWM will not be strong. It is impossible to achieve conservation of total momentum if there exist significant dispersion in the cavity. Therefore dispersion must be compensated for FWM to occur efficiently.

The procedure for non-degenerate FWM is similar. The only difference is instead of the two identical pump photons creating side bands, there are two photons of different frequencies which create additional lines: $\omega_1 + \omega_{-1} = \omega_2 + \omega_{-2}$. Consider all terms that contribute to radiation at ω_2. 4.11 contributes $i = 2$ and 4.18 contributes

$(i, j, k) = (0, -1, 1)$ and $(i, j, k) = (2, 2, 2)$. The simplified partial-differential equation is

$$\frac{\partial A_2}{\partial z} = i\frac{3}{2}\frac{\chi^{(3)}\omega_1}{2nc}\left\{2A_{-1}A_0A_1^* e^{i(k_{-1}+k_0-k_1-k_2)z} + A_2|A_2|^2\right\}. \tag{4.20}$$

Again, the conservation of momentum term is present, reinforcing the importance of dispersion in FWM and thus comb formation.

One may wonder, how do the sidebands achieve gain from FWM? The answer is that the gain comes from depleting the pump. When the pump is the only frequency present in the system[1], the envelopes for the sidebands can be shown to obey

$$\frac{\partial A_{1,-1}^2}{\partial z^2} = \left(\frac{3\chi^{(3)}}{2nc}\sqrt{\omega_1\omega_{-1}}|A_0|^2\right)^2 A_{1,-1}. \tag{4.21}$$

The solution to this partial differential equation is an exponential with a gain term equal to

$$g = \frac{3\chi^{(3)}}{nc}\sqrt{\omega_1\omega_{-1}}|A_0|^2. \tag{4.22}$$

This gain comes strictly from the $\chi^{(3)}$ non-linearity and does not require ω_1/ω_{-1} to already exist in the system.

4.1.3 Injection locking in QCL combs

As mentioned in the beginning of 4.1, QCL combs start as multi-mode lasers, which requires broadband gain. This gain is linear in nature (a $\chi^{(1)}$ effect) and is unrelated to the $\chi^{(3)}$ gain described by 4.22. Traditionally, Kerr combs form by the sole presence of the $\chi^{(3)}$ gain depleting the strong pump line. However, QCL cavities are quite lossy, and 4.22 alone could not overcome the cavity losses to produce coherent laser lines.

Instead, QCL combs form by a process known as injection locking. When an off-resonance source is incident on a cavity, the cavity can oscillate at the injected frequency rather than its natural frequency. In QCL combs, the natural frequencies

[1] as well as in the absence of phase-mismatch and self-phase modulation

are the cavity modes of an incoherent, multi-mode laser and the injected frequencies are the photons produced by FWM.

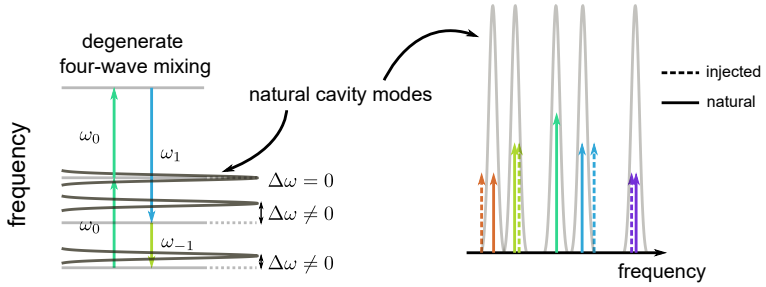

Figure 4-2: **Dispersion and FWM** FWM modes are often off-resonance with cavities modes due to dispersion; the greater the dispersion, the more off-resonance the two photon sources will be.

This is demonstrated in Fig. 4-2. A comb state deviates from the multi-mode state depending on how far the natural cavity modes are off-resonance with the FWM modes. Effectively, the laser oscillate at the cavity modes with spontaneous emission photons from FWM also present inside the cavity. In order for the comb state to supersede the natural oscillating frequencies of the laser, the deviating frequency must be within the "locking range" of the cavity.

Consider the laser cavity of length L [53] shown in 4-3 lasing at a particular frequency ω_0 with intensity I_0. At the same time, there exist an external source of light with frequency ω and intensity I. The cavity has field reflectivity r, gain g and loss α. After one cavity round trip, the field gain, $A_{\mathrm{rt}}(\omega)$, is

$$A_{\mathrm{rt}}(\omega) = e^{i\frac{\omega}{c}n(2L)}r^2e^{(g-\alpha)(2L)}. \tag{4.23}$$

The cavity is lasing at frequency ω_0, which means gain approach losses for ω_0. Therefore:

$$e^{i\omega_0\frac{2nL}{c}}r^2e^{(g-\alpha)(2L)} \approx 1 \tag{4.24}$$

and

$$A_{\mathrm{rt}}(\omega) \approx e^{i\frac{\omega-\omega_0}{c}n(2L)}. \tag{4.25}$$

The electric field continues to reflect back and forth inside the cavity an "infinite" amount of times, each round trip picking up an additional factor of $A_{\mathrm{rt}}(\omega)$. The total field transfer function is given by $A(\omega) = 1 + A_{\mathrm{rt}}(\omega) + A_{\mathrm{rt}}(\omega)^2 + ... = 1/(1 - A_{\mathrm{rt}}(\omega))$,

$$A_{\mathrm{rt}}(\omega) = \frac{1}{1 - e^{i\frac{\omega-\omega_0}{c}n(2L)}} \tag{4.26}$$

Taylor expanding the exponential and noting the free-spectral range (FSR) is given by $\Delta\omega = 2\pi c/(2nL)$, the simplified field gain is found to be

$$A(\omega) \approx \frac{i}{2\pi}\frac{\Delta\omega}{\omega - \omega_0}. \tag{4.27}$$

Light at ω will experience a gain of $|A(\omega)|^2$, which decreases significantly when ω is off resonance with ω_0. However, if ω is tuned sufficiently close to ω_0, its output intensity, $|A(\omega)|^2 I$, can approach the lasing intensity, I_0. At this point, the free-running photons begin to steal gain from the laser media, effectively shutting off the original laser photons and replacing them with the injected photons. Quantitatively, this occurs when

$$\left|\frac{i}{2\pi}\frac{\Delta\omega}{\omega - \omega_0}\right|^2 I > I_0. \tag{4.28}$$

or

$$\left|\frac{\omega - \omega_0}{\Delta\omega}\right| < \frac{1}{2\pi}\sqrt{\frac{I}{I_0}}. \tag{4.29}$$

One notes that either increases the intensity of light from FWM or decreasing the frequency offset will improve injection lock (and thus, stimulate comb formation). Fortunately, reducing cavity dispersion achieves both of these–lower dispersion improves the phase matching condition for FWM and lower dispersion reduces the frequency

drifting of cavity modes. Once injection locking has occurred, the power output of

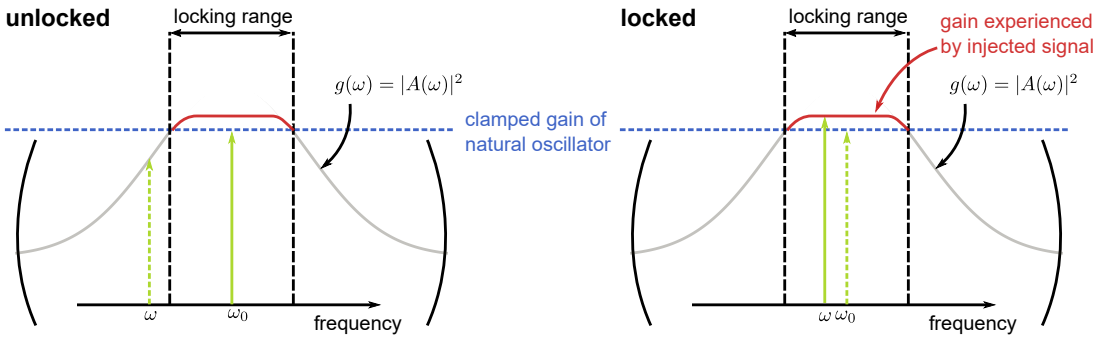

Figure 4-3: **Injection locking and FWM** When the injected photons are significantly detuned from the natural oscillating frequency of the cavity, they can supersede the main oscillator. However, if the injected photons are swept closer to ω_0, they experience a gain which can be greater than that of ω_0. Therefore, the free-running photons can overtake the cavity and lase.

the injected photons is fixed to that of I_0, or slightly above I_0 to account for the external source (FWM), regardless of how close the injected photons are tuned to the cavity mode. This is due to the fact that the amplifying media can only supply so much gain to photons propagating in the cavity.

Chapter 5

Dispersion Engineering and Characterization

When it comes to forming QCL frequency combs, there is one main tuning parameter: the dispersion—often characterized by the group velocity dispersion (GVD). Dispersion is responsible for the "walk-off" of Fabry–Pérot modes in a QCL, prohibiting comb states to form. To counteract this walk-off, the dispersion of the laser must be compensated for. Several techniques, such as GTI mirrors and plasmon layers, have been successfully implemented in the mid-IR; however these methods lack tunability (in the case of plasmon layers) or require mechanically moving parts (in the case of GTI mirrors). Recently, tunable double-chirped mirrors (DCMs) were used to compensate dispersion in THz QCLs, allowing comb formation over the entire lasing range of the device [54]. However, translating the methods used at THz frequencies to the infrared poses a set of unique engineering challenges. This chapter outlines the development and preliminary characterization of mid-IR QCLs with tunable DCM compensators.

5.1 Dispersion in QCLs

5.1.1 Mode spacing of Fabry–Pérot resonators

Dispersion plays a key role in comb formation; it is the reason Fabry–Pérot modes are not evenly spaced. Generally, dispersion is ignored when discussing Fabry–Pérot resonators, as the introduction of second-order effects complicates the analysis. Shown below is a mathematical description of dispersion as well as how dispersion distorts mode spacing in Fabry–Pérot resonators.

Dispersion is the change in group effective index, n_g, as a function of frequency, and is quantified by the GVD, defined as

$$\text{GVD} = \frac{1}{c}\frac{\partial n_g}{\partial \omega}, \tag{5.1}$$

or equivalently in terms of phase,

$$\text{GVD} = \frac{1}{2L_c}\frac{\partial^2 \phi}{\partial \omega^2}. \tag{5.2}$$

All Fabry–Pérot modes must obey the standing wave condition [9], that is the accumulated phase over one cavity round trip must be an integer multiple of 2π. To demonstrate how GVD affects the mode spacing of a Fabry–Pérot resonator, consider the standing wave condition Taylor expanded to second-order around an arbitrary frequency ω_0:

$$\phi(\omega) \approx \phi(\omega_0) + \left.\frac{\partial \phi}{\partial \omega}\right|_{\omega_0} (\omega - \omega_0) + \frac{1}{2}\left.\frac{\partial^2 \phi}{\partial \omega^2}\right|_{\omega_0} (\omega - \omega_0)^2 = 2\pi n. \tag{5.3}$$

The frequency spacing between two adjacent Fabry–Pérot modes, $\Delta\omega = \omega_{n+1} - \omega_n$, can be shown to be

$$\Delta\omega(\omega_{n+1}, \omega_n) = \left(\left.\frac{\partial \phi}{\partial \omega}\right|_{\omega_0} - \omega_0 \left.\frac{\partial^2 \phi}{\partial \omega^2}\right|_{\omega_0}\right)^{-1} \left(2\pi - \frac{1}{2}\left.\frac{\partial^2 \phi}{\partial \omega^2}\right|_{\omega_0} \left(\omega_{n+1}^2 - \omega_n^2\right)\right). \tag{5.4}$$

In the limit that second-order terms go to zero, the mode spacing approaches a

fixed value of $\Delta\omega = 2\pi \left(\frac{\partial \phi}{\partial \omega}\big|_{\omega_0} \right)^{-1}$, but the addition of these terms adds a frequency dependence to the mode spacing proportional to the GVD.

5.1.2 Quantifying dispersion

Dispersion is induced by a number of different aspects of QCLs, including the material system, the waveguide and the gain. For mid-IR QCLs, GVD values can range anywhere in magnitude from 0 to 10,000 fs^2/mm, while at THz frequencies, dispersion can exceed 100,000 fs^2/mm due to the electromagnetic waves strongly coupling to crystalline lattice near the Restrahlen band. Despite the comparatively low GVD, several thousand fs^2/mm worth of dispersion is still enough to destroy injection locking. [55] estimates that for a 3 mm long cavity, the GVD must remain below 560 fs^2/mm in order for the Fabry–Pérot modes to efficiently couple via FWM.

At THz frequencies, high-resolution dispersion information of THz QCLs can be measured using THz time-domain spectroscopy (TDS). A Ti:Sapphire pulsed laser is used to excite a photoconductive antenna, creating a short THz pulse of light. The THz light is then incident on the QCL, and phase information is encoded in the pulse of light. The THz field is then sampled using coherent electro-optic detection, and dispersion can be easily deduced from the phase information. However, generating broadband pulses of infrared light is a non-trivial task, therefore TDS cannot be used to measure dispersion in the mid-IR.

One may wonder how dispersion information can be extracted without using TDS. The answer is through what is known as a Hakki-Paoli measurement [56]. When light enters the waveguide from the front facet of a QCL—either from an external source or through direct generation—it picks up the cavity's phase/loss information as it propagates. When light reaches the back facet, a fraction of the power escapes due to mirror losses and the remaining light reflects back through the waveguide a second time. The light continues to reflect back and forth through the cavity, each round trip experiences more loss and picking up more phase information. In the frequency domain, these reflections off the facet are known as "echoes" in the interferogram.

The intensity of each echo decreases exponentially by a factor related to both the mirror losses and the waveguide losses:

$$\frac{I_{n+1}}{I_n} = Re^{-\alpha_w L_c}. \tag{5.5}$$

Here, R is the power reflectivity of the QCL facet, α_w is the waveguide loss and L_c is the cavity length. Typically, Hakki-Paoli measurements are used to measure waveguide loss, but they can also be used to measure dispersion as the phase information is also encoded in the echoes of the interferogram.

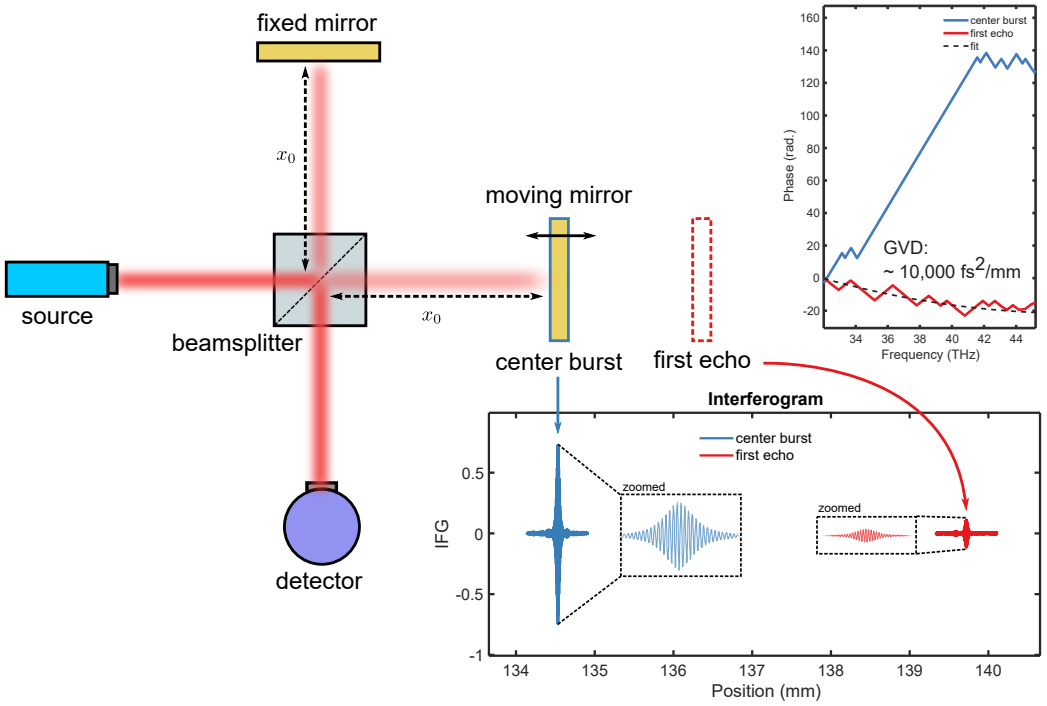

Figure 5-1: **Dispersion measurement of mid-IR QCL** The dispersion of a mid-IR QCL can be measured using a Hakki-Paoli measurement. The QCL is biased below threshold and phase information is extracted by analyzing the first echo of the interferogram, shown in red. The phase of the first echo is fit to a quadratic function, and the GVD is extracted using 5.2

The center burst of an example interferogram, shown in Fig. 5-1, can be analyzed using similar methods described in Chapter 3, with the exception of a linear phase contribution that occurs from the arbitrary position of the center burst. The echo, on the other hand, contains non-trivial phase information. The time it takes for light

to traverse one round trip of the cavity (the round trip time) is $2L_c n_g/c \equiv 2D_1/c$, where D_1 is the displacement of the first echo compared to the center burst. Consider the detector output when the moving mirror is displaced D_1 with respect to the fixed mirror. The electric field reaching the detector is a combination of light emitted directly from the facet, $E(t)$, with light delayed by a round trip time inside the cavity and interferometrically delayed by a time $2(x + D_1)/c$.

$$\begin{aligned} E_{\text{round trip}} &= E(t - 2L_c n_g/c + 2(x + D_1)/c)\sqrt{R_1 R_2}e^{i\phi(\omega)}e^{-\alpha_w L_c} \\ &= E(t - \tau)\sqrt{R_1 R_2}e^{i\phi(\omega)}e^{-\alpha_w L_c} \end{aligned} \tag{5.6}$$

Taking the Fourier transform of interferometric output leads to

$$\text{FT}\left\{\langle E(t)E(t-\tau)\rangle_t\right\} = A(\omega) * |E(\omega)|^2\sqrt{R_1 R_2}e^{i\phi(\omega)}e^{-\alpha_w L_c}. \tag{5.7}$$

Therefore, the phase of the complex Fourier transform is the round trip phase. The dispersion is then calculated using 5.2. It is important to note that the light interrogating the QCL must be phase incoherent, as to not distort the phase information of the cavity. This can be done in one of two ways. The first is utilizing an IR glowbar focused on the facet of the QCL in a transmission measurement scheme [57]. This method has the advantage of being broadband (more broadband than the gain of the QCL), but is ultimately limited by noise as spatio-temporal requirements of the interferogram are too severe. The second method (used in this thesis) is to use the sub-threshold emission of the QCL. This method requires no external optics is only limited by the strength of the spontaneous emission.

The Hakki-Paoli measurement requires an exceptionally strong, incoherent signal over a large period time for an echo to appear above the noise floor of the interferogram. This can typically be achieved by CW biasing the lasers below threshold. Unfortunately, many fabricated devices could not survive the thermal load of CW bias, and could only be biased in pulsed mode. This greatly limited the amount of light captured by the detector. To "amplify" the light, the output signal was sent

through a boxcar averager set to average over the previous 3000 detector signals. Fig. 5-2 shows the center burst of an electroluminescence signal of a pulsed biased QCL with and without the boxcar averager. Without the boxcar averager, the center burst is on the order of the noise, but with the boxcar averager, the center burst is well above the noise floor.

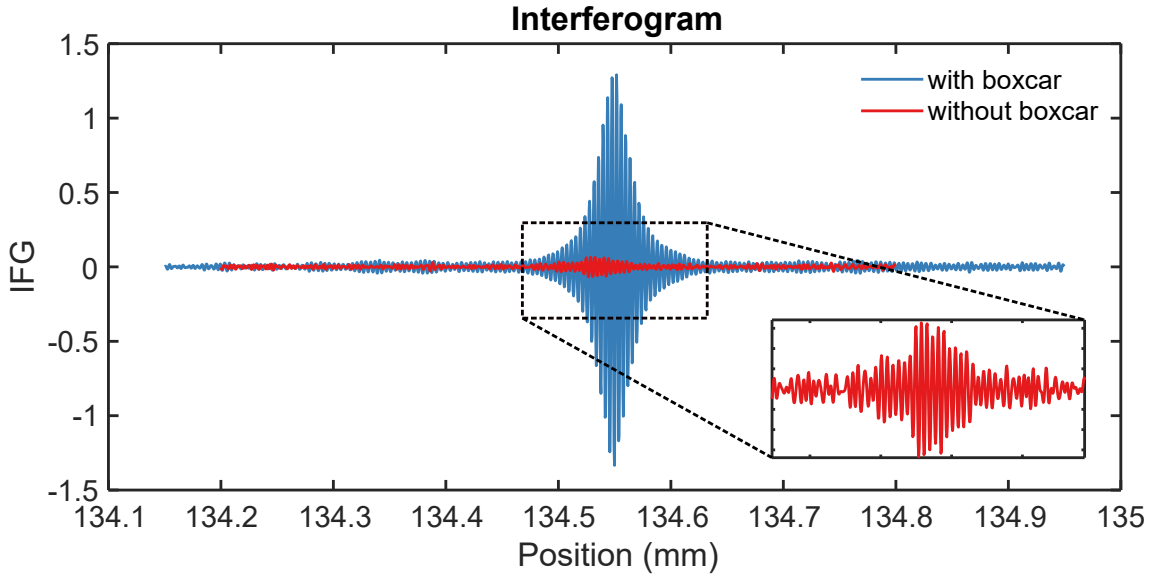

Figure 5-2: **Boxcar averager over the center burst** An electroluminescent center burst with (blue) and without (red) a boxcar averager. The signal-to-noise ratio of the signal is greatly enhanced by the boxcar averager.

5.1.3 Dispersion measurement

Fig. 5-3 shows the IVL and spectrum of a 1.5 mm long, 60 μm wide wet-etched QCL made from wafer index E4589. This wafer has a particularly low lasing threshold (< 2 kA/cm^2) and shows a broad lasing spectrum spanning over 40 cm^{-1}. However, a broad lasing spectrum is not necessarily a comb spectrum. The echos present in the interferogram get smaller symmetrically around the center burst. This loss in amplitude is attributed to a loss of phase coherences for photons interfering at different round trips. If laser were acting as a comb, each burst in the interferogram would be indistinguishable from one another. Therefore, the laser has non-negligible dispersion.

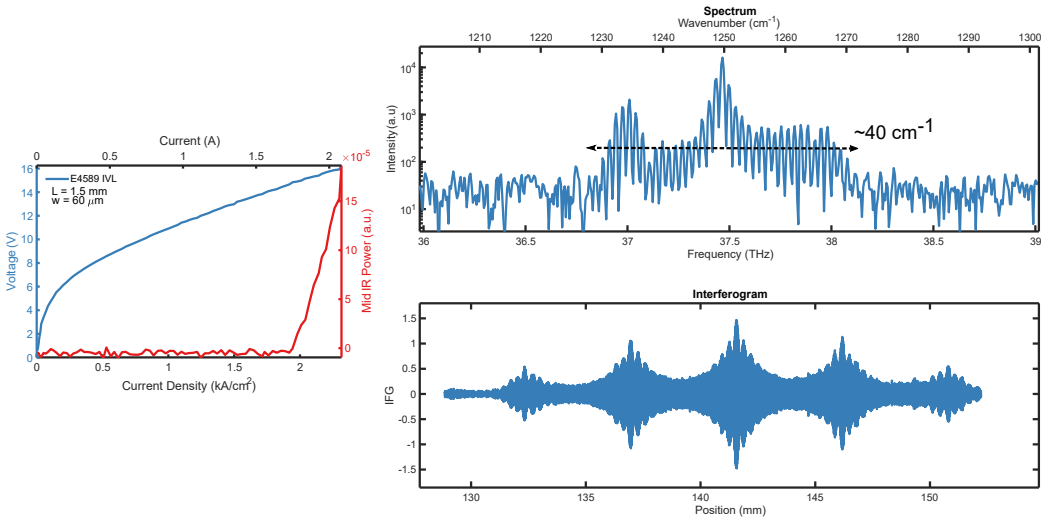

Figure 5-3: **E4589 IVL and Spectrum** Left: the IVL of a 1.5 mm long, 60 μm wide wet-etched device from wafer index E4589. The current threshold is 1.8 kA/cm^2. Right: the spectrum and interferogram of the same device biased at 2.0 A. The device is lasing at the fundamental modes of the cavity, but is not acting as a comb.

Dispersion measurements were conducted on E4589 devices using methods described in 5.1.2 (Fig. 5-4). Devices were cleaved into 1 mm bars to decrease the round trip time, thus reducing the amount of loss light experiences in the cavity. Pulsed (0.25% duty cycle) sub-threshold interferograms were taken at the center burst, first echo as well as the negative first echo. Windowed interferograms were used to find the GVD over a range of frequencies, from 36 THz to 39 THz, roughly spanning 100 cm^{-1}. As expected, the center burst has zero GVD over the entire frequency range. The echoes, on the other hand, have substantial GVD ($>$ 5000 fs^2/mm), which changes sign twice—once at 36.75 THz, and again at 38.25 THz. In addition, the opposing echoes have opposite dispersion. This is expected as the a negative echo effectively advances light by a round-trip time (as apposed to delaying it), introduces an additional negative sign to the analysis.

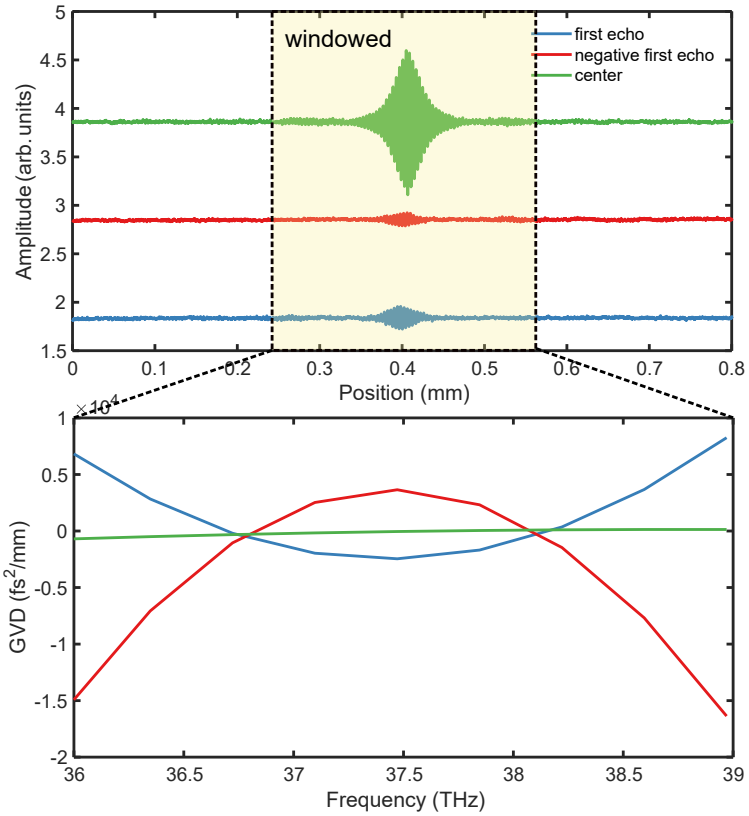

Figure 5-4: **E4589 interferogram and dispersion** The top panel shows the averaged interferograms for the center (green), negative first echo (red) and first echo (blue) for a 1 mm long device fabricated from E4589. The windowed interferograms were used to find the GVD from 36 THz to 39 THz. The center burst contains no dispersion, while the echos contain equal and opposite dispersion.

5.2 Dispersion compensators

Although the first mid-IR QCL comb was developed without deliberate dispersion compensation, the gain medium was specially designed to optimize comb performance. Fig. 5-5 shows the calculated GVD and gain for the heterogeneous gain media used in the first QCL comb (red curve) compared to a typical mid-IR QCL gain media (blue curve). The GVD for the heterogeneous design is zero spanning from 1450 cm^{-1} to 1550 cm^{-1}, with a flat gain spectra, while the GVD for the bound-to-continuum (BTC) design changes rapidly over the gain spectra. In general, however, the QCL gain media will not exhibit this behavior, so the dispersion must be externally accounted for.

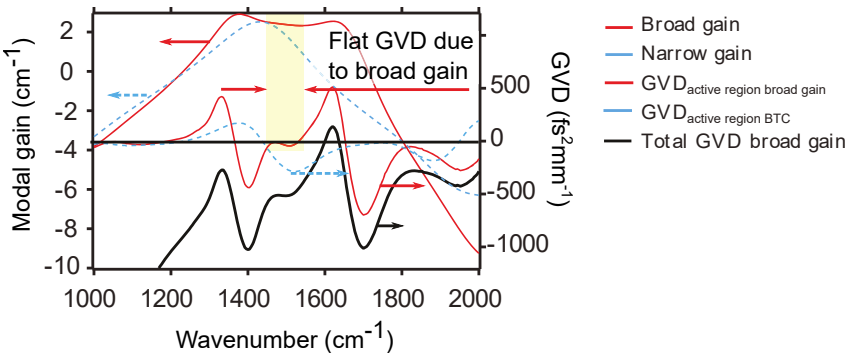

Figure 5-5: **GVD and gain for the first mid-IR QCL comb** The calculated GVD and gain for the gain medium used in the first mid-IR QCL comb (red). The gain medium is a heterogeneous stack of several active regions, optimized to give flat gain and zero dispersion over a large spectral range. The GVD and gain of the heterogeneous gain medium is compared to a typical mid-IR active region design (blue). The total GVD (including cladding) is shown in black. This figure is adapted from [5]

For THz QCL combs, electrically tunable DCMs have been used with great success in compensating large dispersion (Fig. 5-6). DCMs act as Bragg reflectors on one facet of laser by periodically modulating the effective refractive index of the waveguide. By "chirping" the periodicity of the oscillations, different wavelengths experience the resonant Bragg condition along different points inside the cavity. For example, if the periodicity is chirped from a small value to a large value, longer wavelengths of light will travel longer distances inside the cavity as compared to shorter wavelengths of light. If the periodicity is chirped properly, the dispersion of laser can be canceled. In order to minimize large reflections at the beginning of the dispersion compensator portion of the waveguide, the amplitude of the oscillations is also chirped, hence the name double-chirped mirrors. By fabricating a small (2 μm) gap between the Fabry–Pérot section and DCM, the two become electrically isolated while remaining optically coupled. This allows the DCM to be electrically tuned independently from the laser itself. This additional level of tunability allows the engineer to turn any multi-mode lasing state into a comb state.

However, directly translating the methods used for THz QCL combs to the mid-IR introduces several engineering challenges. THz wavelengths are 10 times longer than

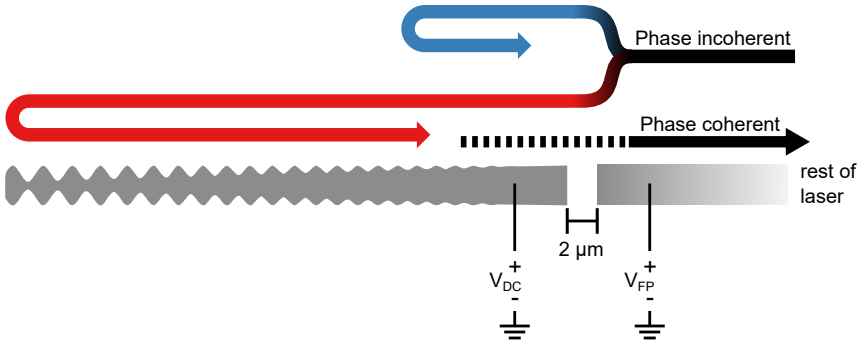

Figure 5-6: **Working principles of a DCM** The double-chirped mirror (DCM) works as a Bragg reflector with a spatially-dependant resonant condition. The periodicity of the oscillation is chirped from a small value to a large value, which allows long wavelengths of light to penetrate far into the cavity, while shorter wavelengths are quickly reflected. If a gap is fabricated between the DCM and rest of the laser, the two can be independently biased, giving another control-knob to the engineer.

mid-IR wavelengths, therefore the spatial resolution required in designing THz DCMs is significantly larger. μm level resolution quickly becomes nm at mid-IR frequencies. To remedy this, a third-order DCM is utilized as apposed to a first order DCM. This results in a reduced facet reflectivity from close to unity to 30%, which is on the order of a cleaved facet. Even with a third-order DCM, e-beam lithography must be used to define the DCM as apposed to standard optical lithography. Furthermore, the spatial requirements of mid-IR DCMs precludes the use of wet-etching in order to preserve the flatness of the sidewall.

DCMs were initially designed using a transfer-matrix method (TMM) simulation in MATLAB. The designed DCM is shown in 5-7. The induced GVD of the DCM exactly cancels the dispersion of the laser. Several other DCMs were designed that offset the canceled dispersion by $\pm$ 20 % to take into account errors in the dispersion measurement. Note that difference in magnitude between the the compensator GVD and the device GVD is due to the differing length of the two sections of the laser.

The TMM simulation assumes the mode is completely confined within the waveguide using infinitely-long perfect electric conductors (PECs). This is not a completely accurate assumption (although it is a much better assumption in THz QCLs where the active region is sandwiched between metal waveguides), so further DCMs were

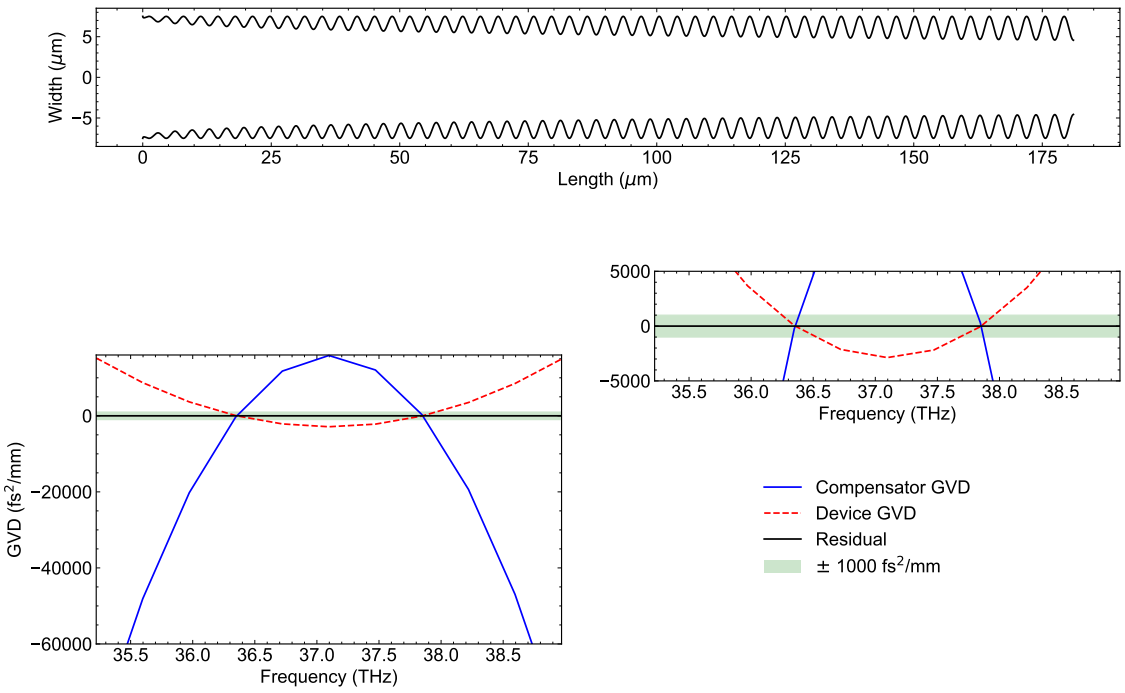

Figure 5-7: **Example DCM designed in MATLAB** The corrugation structure for the designed DCM is shown in the top panel, while its GVD is shown in the bottom panel (blue). The induced GVD exactly cancels the dispersion of the laser.

designed using genetic optimization in COMSOL—a full wave simulation package.

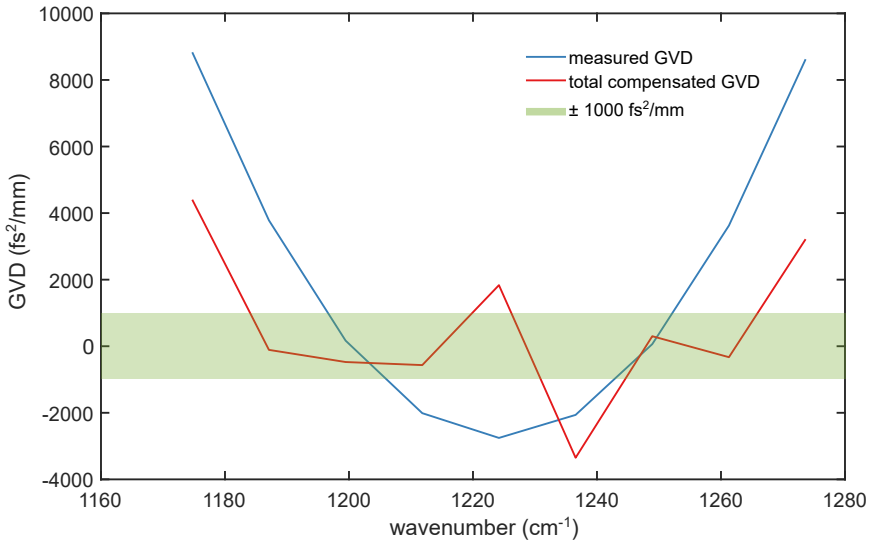

Figure 5-8: **Example DCM designed in COMSOL** The residual GVD of the compensator the device dispersion lies within ± 1000 fs^2/mm for more than 70 cm^{-1}

Corrugation structures were generated in MATLAB, then sent to COMSOL to run the electromagnetic simulation. The reflectivity of the structure was calculated and used to find the GVD of the generated DCM. With fabrication constraints considered in the model, the residual GVD of the optimized structure is within ± 1000 fs^2/mm for more than 70 cm^{-1} (Fig. 5-8).

Fabrication of the compensators follows the exact same fabrication flow discussed in chapter 3, with the exception of window-opening and Au electroplating. E-beam lithography is used to define the Ni hard-mask for dry-etching. Example DCM are shown in Fig. 5-9, with the top picture being a TMM design, while the bottom picture is a COMSOL design. The dry-etching process produces straight sidewalls while preserving the integrity of the DCM's oscillations. It should be noted that the two structures look quite different as the optimization of the design has many local minima.

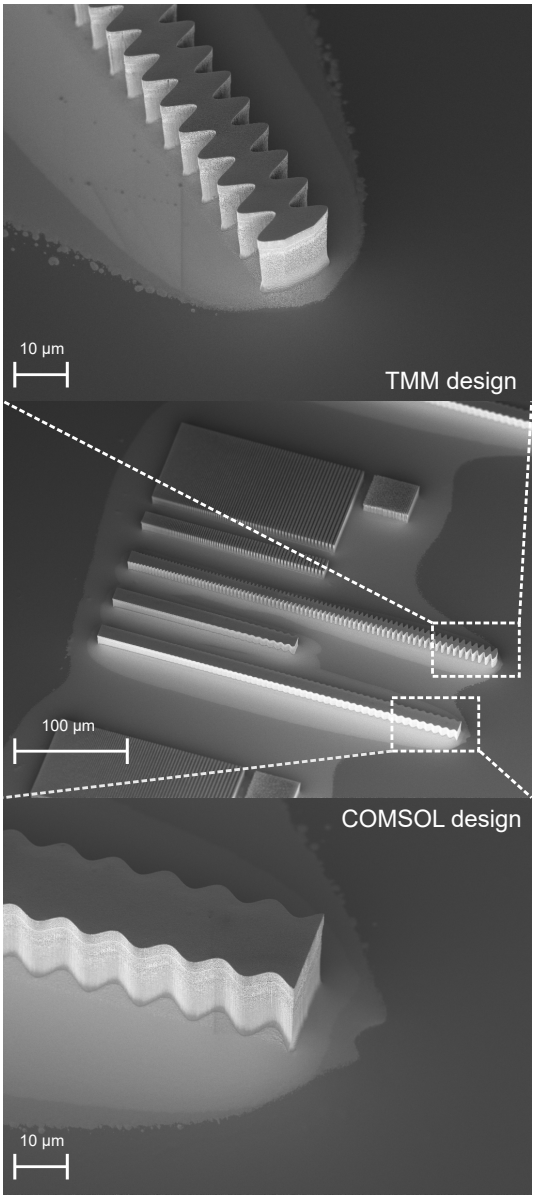

Figure 5-9: **SEM of DCMs** SEM images of TMM generated structures (top) and COMSOL generated structures (bottom) are shown.

5.3 Initial result

The initial result of devices with and without compensators is shown in Fig. 5-10. The pulsed biased (0.5 % duty-cycle) spectra of a 2.26 mm Fabry–Pérot cavity is shown on the left, while the spectra for another 2.26 mm Fabry–Pérot cavity with a dispersion compensator is shown on the right. The bias on both devices spanned from 1.17

A—just above threshold—to 2.80 A. The spectra of the device with the dispersion compensator is significantly more broadband than that of the bare Fabry–Pérot cavity. However (for devices with and without compensators), the spectra is not continuous and the mode spacing is uneven. Even when biasing the dispersion compensator, spectral holes are still present.

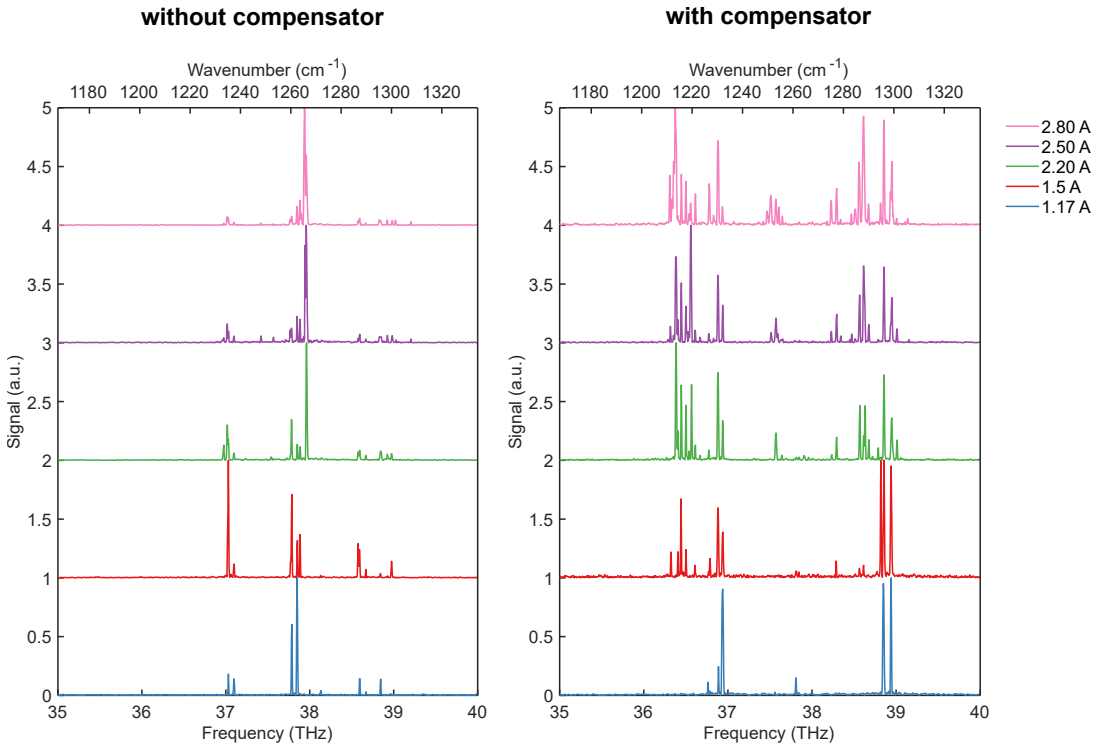

Figure 5-10: **Initial device result** Spectra of a 2.26 mm device from E4589 with (right) and without (left) a DCM dispersion compensator. While the device with the DCM is more broadband than the laser without, both devices show several spectral holes and do not lase at the fundamental modes of the cavity.

This result motivated further study on the effects of pulse-biasing a mid-IR QCL compared to CW biasing. To do this, a commercially-available Fabry–Pérot QCL (Thorlabs, H0994) was pulsed-biased with a variety of pulse-widths. The pulsed spectra and intracavity beating (measured from a spectrum analyzer) was then compared to CW measurements. The results of this study are shown in Fig. 5-11. As the pulse width is increased from 1 μs to 400 μs, the spectra slightly compresses in the frequency domain, and the weak intracavity beating begins to red-shift, indica-

tive of active region heating. However, both the pulsed beating and spectra look far different from the CW results. The CW spectra is clearly lasing at the fundamental modes of the cavity, and posses a strong intracavity beating, which is several orders of magnitude larger than the pulsed beating.

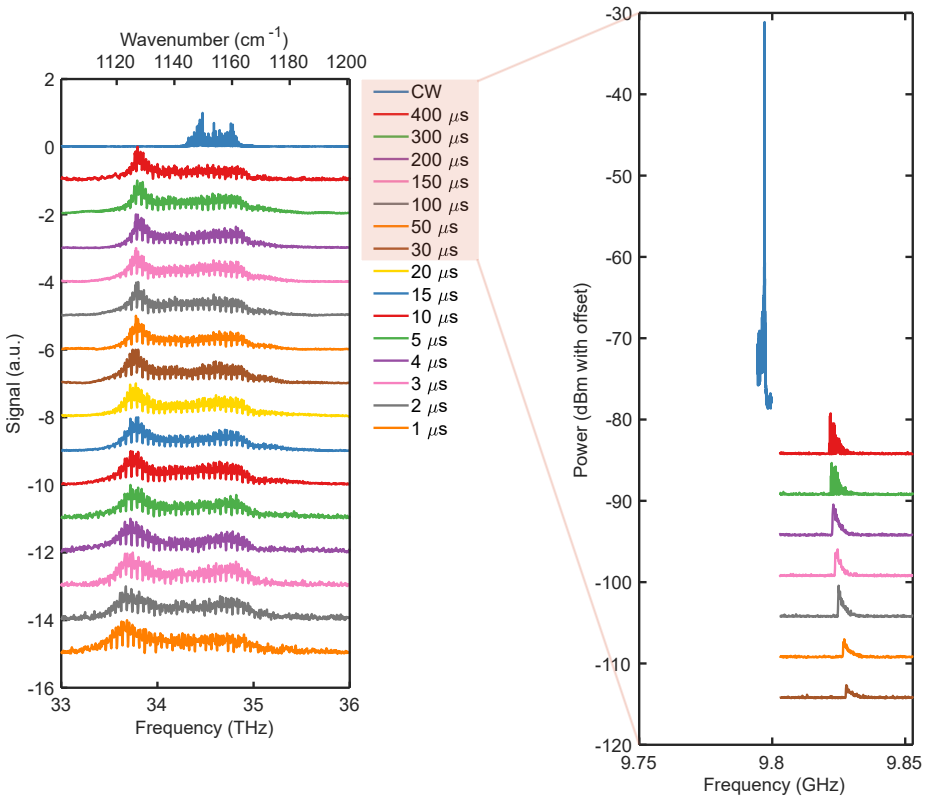

Figure 5-11: **Pulsed vs. CW operation of a mid-IR QCL** The left panel shows the spectra for a Thorlabs QCL under pulse bias from a pulse with of 1 μs to 400 μs, as well as under CW bias. Even at 400 μs, the pulsed and CW spectra are dissimilar. The right panel shows the intracavity beating measured on a spectrum analyzer (resolution bandwidth: 3 kHz, sweep time: 1 sec., span (CW): 5 MHz, span (Pulsed): 50 MHz). The CW beating is much stronger and more narrowband compared to the pulsed beating.

One may wonder why the results are so different, and the answer comes from the thermal transience that occurs during the bias pulse. At CW bias, the temperature of the active region reaches an equilibrium value depending on the bias, while under pulsed operation, the temperature fluctuates every time a pulse occurs. Therefore, the device never reaches a thermal equilibrium, ultimately distorting the output of the

QCL. This is not to say a QCL cannot achieve broadband, multi-mode lasing while under pulsed conditions; rather, the large thermal transience that occurs in mid-IR QCLs will prevent strong comb formation, and will hinder spectroscopic applications [58]. Therefore, CW operation is the only feasible direction to achieve stable comb formation.

5.4 Towards room-temperature CW operation

Achieving CW operation at room temperature requires a significant amount of engineering considerations to dissipate the large thermal load ($>$ 10 W). State-of-the art mid-IR QCLs utilize Fe doped InP as sidewall coverage to remove heat from the active region. However, as mentioned in Chapter 3, this method was not utilized in this thesis. Instead, a combination of Au electroplating and epi-down mounting was used in attempts to reach RT-CW operation.

Initially, electroplated devices were failing under CW bias. Thermal build-up caused catastrophic failure at the facet, as shown in Fig. 5-12. It was determined that the failure occurs due to a lack of Au near the cleaved facet. In order to avoid this, the devices were cleaved either extremely close to the electroplated edge, or through the electroplated Au.

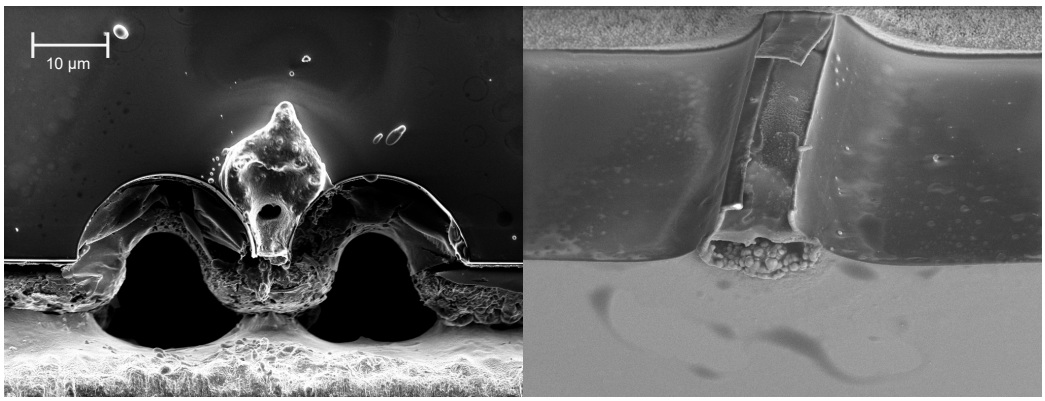

Figure 5-12: **Exploded facets** Catastrophic device failure occurs when there is insufficient Au near the facet to dissipate heat. Heat cannot be removed from the active region and the facet explodes.

Both of these methods prevented catastrophic failure, but devices still could not lase at room temperature. Despite this, Fabry–Pérot devices that were CW biased at 64 K showed broadband (>40 cm^{-1}) spectral coverage (Fig. 5-13), as well as narrow intramodal beating, indicative of coherent, comb-like operation.

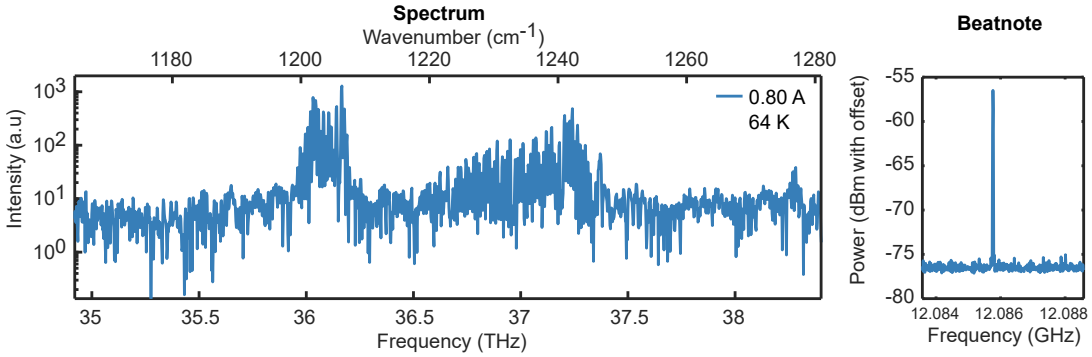

Figure 5-13: **Cold spectrum and beatnote** A 2 mm long Fabry–Pérot cavity (A1182) biased at 0.80 A at 64 K. The spectrum is shown on the left, while the beating is shown on the right.

RT-CW operation was recently achieved, but the device was short-lived. Efforts to achieve robust RT-CW devices are still ongoing. Several parameters such as thickness of the electroplated Au, mounting duration time, and substrate thickness are currently being explored as possible bottlenecks for RT-CW operation. Once devices can be routinely CW biased, high-resolution dispersion measurements can be taken and dispersion compensators can be designed using the methods described in 5.1 and 5.2.

Chapter 6

Coherence of QCL Frequency Combs

How does one distinguish a multi-mode lasing state with a comb state? The echos in the interferogram can be used to identify the mode of operation qualitatively, but they lack the ability to quantitatively define coherence. This can be solved a number of different ways. Usually, the presence of strong intracavity beating via an electrical beatnote is a good indicator the laser is acting as a comb, but it is not conclusive proof of comb operation. In order to fully prove the existence of a comb state, a heterodyne measurement must be completed. The most powerful such technique is Shifted Wave Interference Fourier Transform Spectroscopy (SWIFTS). Using SWIFTS, both the amplitude and phase of the intracavity beating is measured and used to extract the time-domain profile of the instantaneous electric field. This chapter reviews techniques commonly used to evaluate the coherence of QCL combs as well as some results of these techniques applied to devices in this thesis.

6.1 The Beatnote

As alluded to in previous chapters, the easiest way to infer whether an optical device is acting as a comb is through the beatnote, which is a measurement of the intracavity beating of the laser lines. The laser signal is incident on a detector, as shown in Fig. 6-1, and beating between each line at optical frequencies produces a signal at radio

frequencies. The beatnote frequency is given by

$$f_{\text{beatnote}} = \frac{c}{2n_g L_c}, \tag{6.1}$$

which is primarily a function of the length of the cavity, L_c. The full-width half-max (FWHM) of the beatnote can range anywhere from sub kilohertz for a highly-coherent source, to many hundreds of megahertz. Accordingly, a completely incoherent source will possess no beatnote. Therefore, the fastest way to tell whether a device is *not* a frequency comb is by measuring the beatnote. A beatnote measurement is commonly

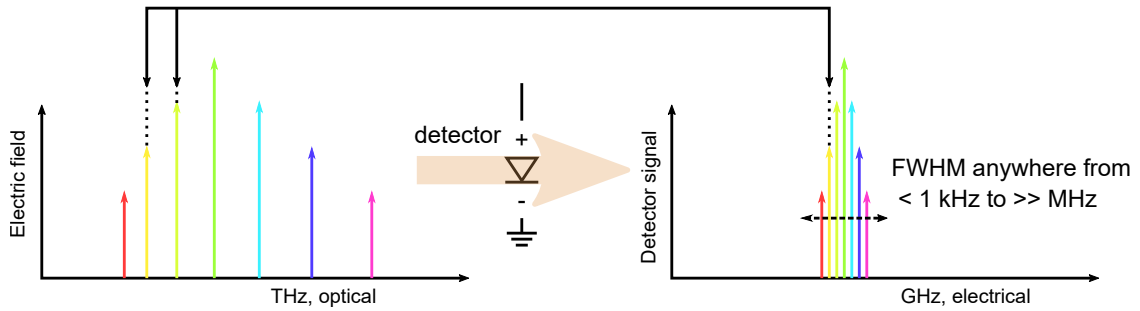

Figure 6-1: **Diagram of the beatnote** The beating of all the spectral lines at optical frequencies produces a beatnote at radio frequencies, which can be measured from a spectrum analyzer. Adapted from [6].

conducted using one of a two detectors. The first of which is an ultra-fast optical detector and the second of which is the QCL itself, read off the bias wire.

6.1.1 Electrical beatnote

An electrical beatnote is the measurement of the beating of the lasing lines using the QCL as self-detection. When a QCL is operating coherently, the beating produces AC current modulations that can be read off of a bias tee in the setup shown in Fig. 6-2. The power supply is fed through the DC portion of the bias-tee, as indicated by the inductive element, while the beatnote is read from the AC portion of the bias-tee. The capacitve element in the bias-tee blocks DC, so the output can be amplified (if necessary, the electrical beatnote is usually quite strong) and examined using an rf spectrum analyzer. The particular electrical beatnote shown in Fig. 6-2 has a

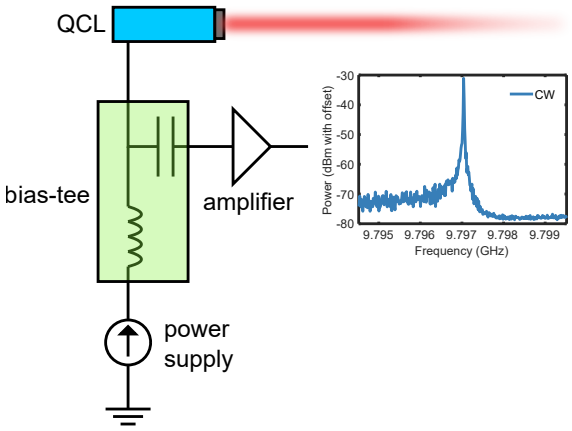

Figure 6-2: **Electrical beatnote measurement** The electrical beatnote is extracted from a bias-tee. A power supply (typically a current source) drives the QCL above threshold. AC current modulations that occur from intracavity mixing are taken from the AC input of the bias-tee, amplified and examined using a spectrum analyzer.

FWHM on the order of kHz, indicative of a highly-coherent device (Thorlabs H0994). However, the beatnote has a broad pedestal at lower frequencies; therefore the device cannot be characterized as a true comb.

6.1.2 Optical beatnote

Beatnotes can also be measured optically using an ultra-fast detector. A typical cavity length for a QCL is 4.5 mm, which corresponds (roughly) to a round-trip frequency of 10 GHz. Therefore, the detector must have a responsivity up to GHz level. For IR QCLs, a quantum-well infrared photodetector (QWIP) is commonly used. The bandstructure for a typical QWIP is shown in Fig. 6-3. A QWIP is a optical device that utilizes intersubband transitions to detect photons. When photons are incident on a biased QWIP, electrons are excited from the bound states of the quantum wells (typically GaAs/AlGaAs for IR) to the continuum, producing a photocurrent, I_{ph}, equal to [59]

$$I_{\mathrm{ph}} = e\phi\eta g_{\mathrm{ph}} \tag{6.2}$$

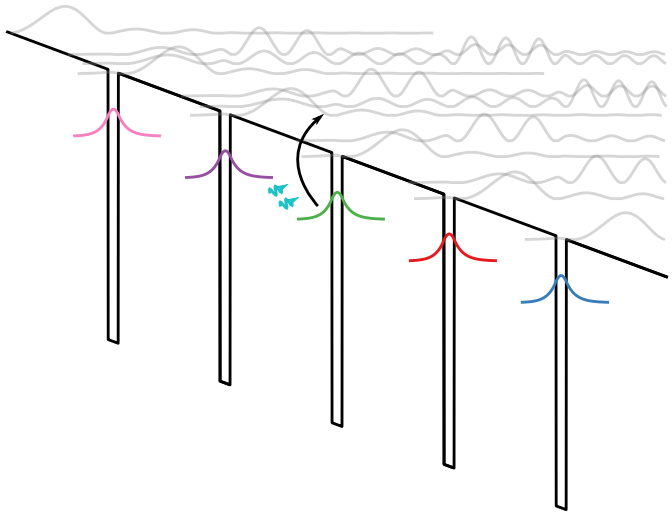

Figure 6-3: **Bandstructure of a QWIP** When photons are incident on a biased QWIP, carriers are excited from the highest subband to the continuum, inducing a photocurrent directly proportional to the photon flux.

Here, ϕ is the photon flux, η is absorption efficiency and g_{ph} is the photconductive gain. State-of-the-art QWIPs can detect signals up to 40 GHz.

It is important to note that an optical beatnote is causally the same as an electrical beatnote; they both arise from the same physical phenomena. Fig. 6-4 shows a QCL beatnote measured both electrically and optical. Although much weaker, the optical beatnote closely resembles the electrical beatnote in frequency and line-shape.

6.2 Interferometric techniques

The beatnote is the most convenient measurement for comb characterization, but as stated previously, it is not full proof of comb operation. How can one be certain that all laser lines contribute to the beatnote? For example, what if only two lines in the spectra beat strongly to produce the beatnote? In order to determine whether this is the case, interferometric techniques such as intermode beat spectroscopy or SWIFTS can be conducted.

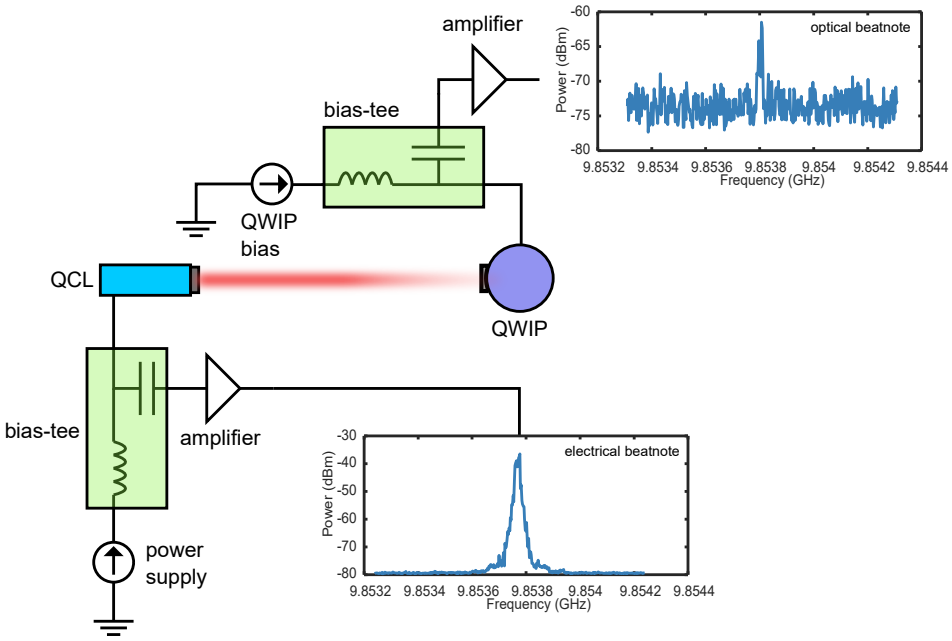

Figure 6-4: **Optical beatnote and electrical beatnote** The beatnote of a mid-IR QCL (Thorlabs H0355) measured both optically (through a QWIP) and electrically (through the bias-tee) with the same spectrum analyzer.

6.2.1 Intermode beat spectroscopy

Intermode beat spectroscopy is an interferometric technique first developed by Andraes Hugi *et. al.* in 2012 [5]. Intermode beat spectroscopy is used to determine how coherent a source is by comparing the generic FTS laser spectra with the analog spectra produced only by the optical beatnote. The basic setup for intermode beat spectroscopy is shown in Fig. 6-5. Intermode beat spectroscopy measures the FTS spectra beating at a particular frequency, ω_{LO}, which typically chosen to the be the round trip frequency. The intensity output of intermode beat spectroscopy is

$$I_{\mathrm{BS}}(\omega_{\mathrm{LO}},\tau) \approx \left| \sum_n \left\langle E_{n+1} E_n^* e^{i(\omega_{n+1,n}-\omega_{\mathrm{LO}})} \right\rangle e^{i\omega_n \tau} \right|^2 . \tag{6.3}$$

Fundamentally, intermode beat spectroscopy is sensitive to the phase difference between lines in the spectra. If two adjacent lines n and $n+1$ are not separated exactly by ω_{LO}, they will be averaged away and not contribute to the output. If the spectra

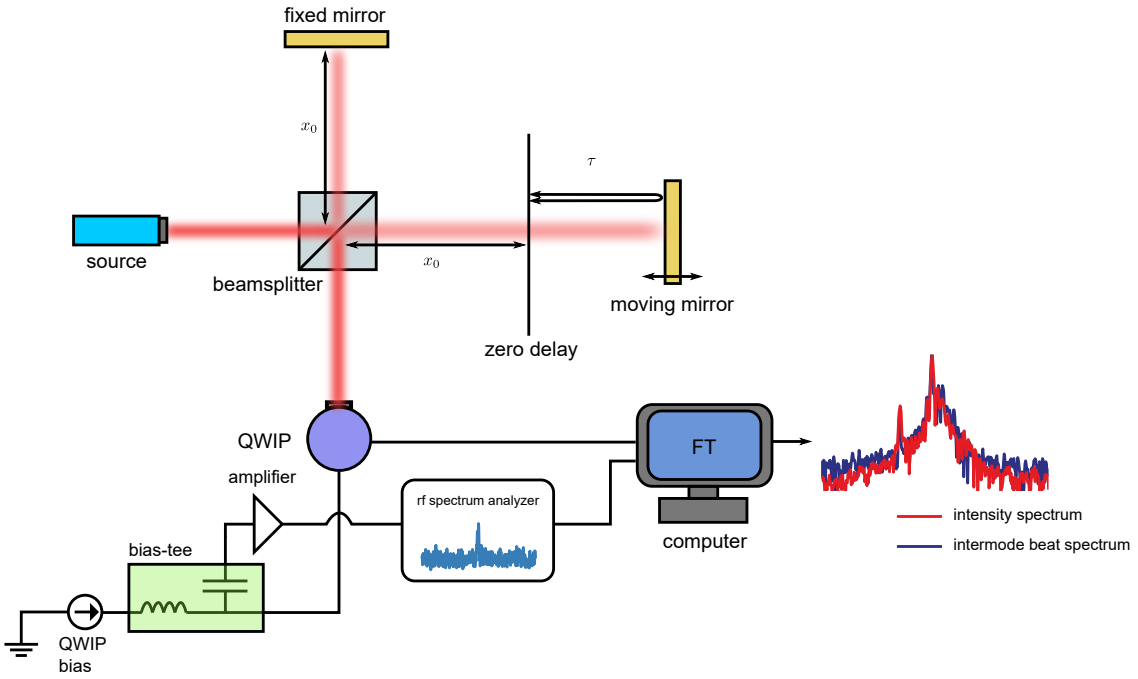

Figure 6-5: **Intermode beat spectroscopy setup** The optical beatnote measured from a QWIP is interogated interferometrically, Fourier transformed and compared to a normal FTS spectra. If the two spectra strongly overlap, the all laser lines present in the spectra contribute to the beatnote. Data adapted from [5]

obtained from normal FTS and intermode beat spectroscopy are the same, all lines in the comb are beating at the round-trip frequency. It is important to note that intermode beat spectroscopy cannot be conducted using the electrical beatnote, as the interference of the beating can only be measured using a QWIP. More importantly, the interference of the beating will not show up in the electrical signal because the two beatnotes are no longer causally connected; the physics of the two beatnotes is different.

Intermode beat spectroscopy is a powerful technique that can give valuable insight on the conditions of a QCL comb state; however, it does not provide a truly quantitative measure of coherence, being as it is only sensitive to the phase *difference* between lines, and cannot directly measure phase.

6.2.2 SWIFTS

SWIFTS is a technique developed by David Burghoff *et. al.* in 2014 [8] that directly measures the amplitude and phase of the intracavity beating to quantitatively describe the coherence of a device. SWIFTS achieves this by demodulating the output of conventional FTS with a local oscillator whose frequency is equal to the repetition rate of the device.

To understand the signal processing involved in SWIFTS, first consider demodulating the output of FTS using an arbitrary local oscillator at frequency ω_{LO} using an I(in phase)/Q(quadrature) demodulator. Doing this produces two new interferograms that have I and Q modulations. The SWIFTS interferograms are $S_Q(\tau) = \langle E(t)E(t-\tau)\sin(\omega_{\mathrm{LO}}t)\rangle$ and $S_I(\tau) = \langle E(t)E(t-\tau)\cos(\omega_{\mathrm{LO}}t)\rangle$. Using analysis identical to that of Chapter 3, the Fourier transform of the two SWIFTS interferograms can be shown to be

$$S_I(\omega) = A(\omega) * \frac{1}{2}[(E*K)(\omega-\omega_{\mathrm{LO}}) + (E*K)(\omega+\omega_{\mathrm{LO}})]E^*(\omega) \tag{6.4}$$

$$S_Q(\omega) = A(\omega) * \frac{1}{-2i}[(E*K)(\omega-\omega_{\mathrm{LO}}) - (E*K)(\omega+\omega_{\mathrm{LO}})]E^*(\omega), \tag{6.5}$$

which can be combined into a quantity $S_{\pm}(\omega)$ defined as

$$S_{\pm}(\omega) \equiv (S_I \pm iS_Q)(\omega) = A(\omega) * [E^*(\omega)(E*K)(\omega\pm\omega_{\mathrm{LO}})]\,. \tag{6.6}$$

In the limit that the measurement Kernel is taken as a delta function, 6.6 becomes

$$S_{\pm}(\omega) = A(\omega) * [E^*(\omega)E(\omega\pm\omega_{\mathrm{LO}})]\,. \tag{6.7}$$

SWIFTS is effectively a cross-correlation measurement—it determines how correlated the fields are shifted by an arbitrary frequency ω_{LO}. If the shifting frequency is chosen as the repetition rate of the device under test ($\omega_{\mathrm{LO}} = \Delta\omega$), SWIFTS will only produce non-zero results if the lasers lines are both exactly shifted by the repetition rate *and* phase coherent. Note that since the apodization function is applied after the frequency

shifting, SWIFTS is not limited by the resolution of the FTIR; rather, the resolution of SWIFTS is only determined by the duration of the measurement.

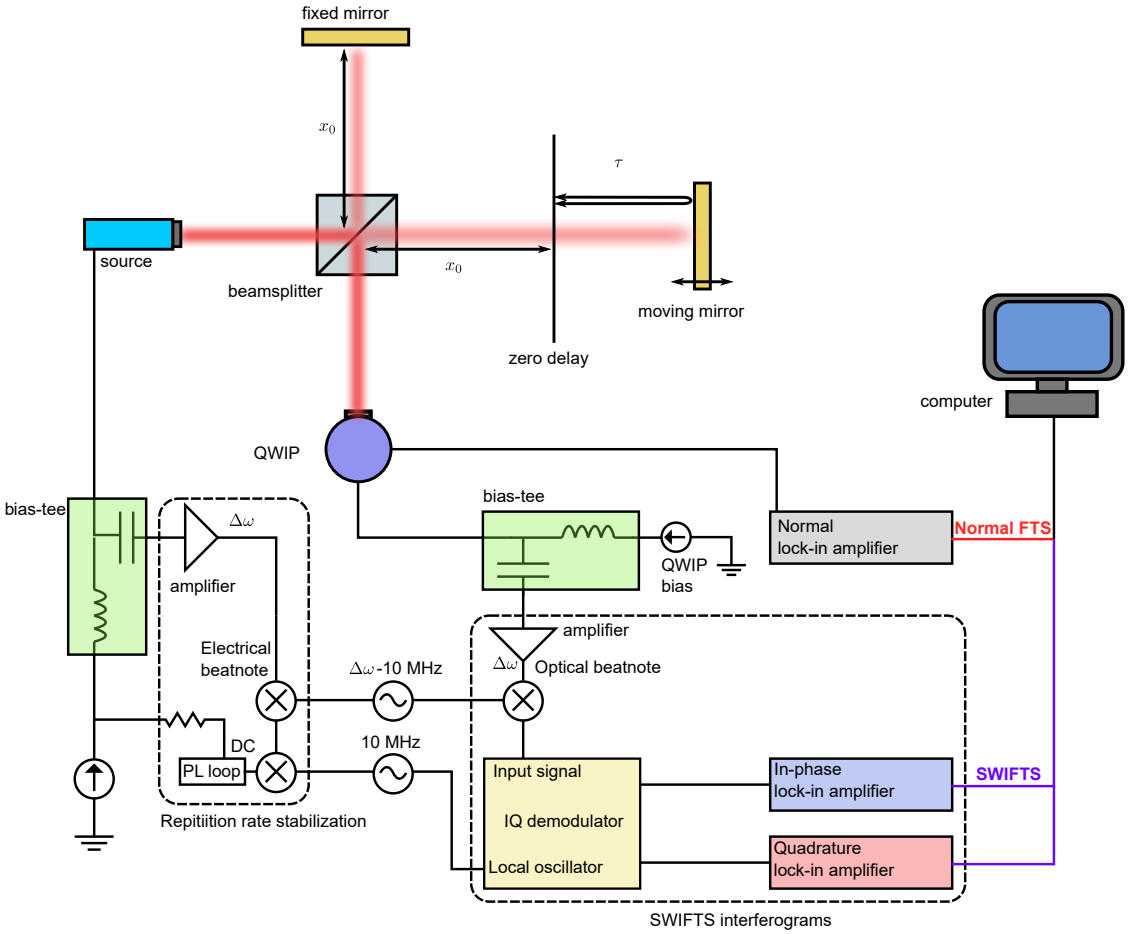

Figure 6-6: **SWIFTS setup** The three major components of a SWIFTS measurement are repetition rate stabilization, normal FTS and generation of SWIFTS interferograms. Repetition rate stabilization is done by down-converting the electrical beatnote to DC, and locking the DC signal using a phase-locked loop. The output of the QWIP is used for both normal FTS and generating the SWIFTS interferograms by down-converting the optical beatnote to 10 MHz and demodulating with an external local-oscillator.

An example SWIFTS measurement setup is shown in Fig. 6-6. It is broken up into three sections: repetition rate stabilization, normal FTS and SWIFTS interferogram generation. The first section is used to stabilize the device repetition rate to reduce noise in the SWIFTS measurement. The repetition rate of comb devices can jitter due to temperature fluctuations, current fluctuations, mechanical vibrations, etc. To

stabilize the device, the repetition rate (taken from the electrical beatnote) is down-converted to DC and fed to phase-locked loop, which constantly adjusts to the current driven to the device in order to maintain the DC input. Any fluctuations creates AC current, which the phase-locked loop seeks to minimize.

The second section of the setup is normal FTS. The output of the detector—which must be an ultra-fast detector, such as a QWIP—is fed to a lock-in amplifier, and is used to obtain the device spectra. This spectra is used as a reference for the spectra generated from SWIFTS.

The last (and most important) part of the setup is the generation of the SWIFTS interferograms. The optical beatnote is first down-converted from the repetition rate, $\Delta\omega$, to 10 MHz and is demodulated using an IQ-demodulator. This down-conversion is done to place the optical beatnote in the optimal frequency range of the IQ-demodulator. In addition, the down-conversion only shifts the frequency of the output and does not disturb the phase of the fields. The rf synthesizer used to down-convert the electrical beatnote to DC is also used as the local oscillator for the IQ demodulator. The outputs of the IQ-demodulator, $S_I(\tau)$ and $S_Q(\tau)$, are inputs to two lock-in amplifiers with identical settings to the lock-in amplifier used to obtain the normal FTS spectra.

SWIFTS can also be preformed in the so-called self-referential scheme shown in Fig. 6-7, where instead of stabilizing the repetition rate of the device, the down-converted electrical beatnote is directly used as the local oscillator for the IQ-demodulator. Of course, this method of SWIFTS does not provide the same level of coherence information as traditional SWIFTS, but reduces the number of rf-synthesizers required from 2 to 1, and drastically simplifies the biasing of the QCL. This method of SWIFTS was utilized for this thesis.

Fig. 6-8 shows the result of a SWIFTS measurement on a Thorlabs QCL (H0355) with broadband operation from 34 THz to 35 THz. The right panel shows the electrical beatnote taken from the device at a bias of 0.8 A, while the left panel shows both the normal FTIR spectra (red) and the SWIFTS spectra (blue). Frequencies where the normal spectra and SWIFTS spectra strongly overlap indicate regions of high

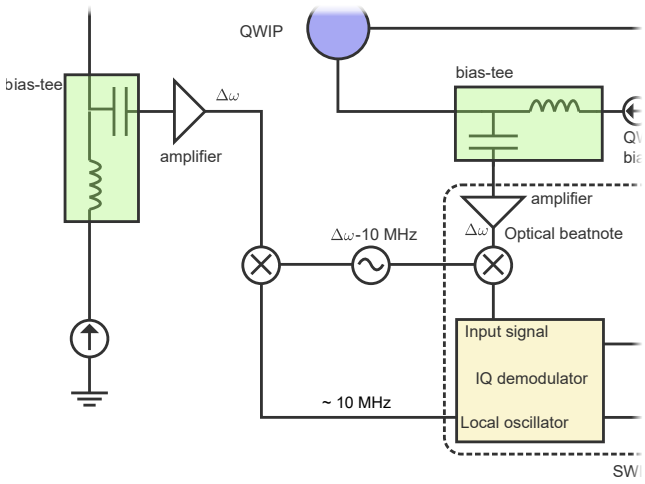

Figure 6-7: **Self-referential SWIFTS** Instead of locking the electrical beatnote to an external local oscillator, the electrical beatnote itself can be used as a local oscillator.

coherence. While frequencies where the normal spectra greatly exceed the SWIFTS spectra are regions of low coherence. This precisely demonstrates the weakness of the beatnote. Despite the FWHM of the beatnote being on the order of 1 kHz, the device does not act as a comb over the entire spectral range of the device, notably from 34.2 THz to 34.5 THz.

The most powerful aspect of SWIFTS is that is a phase-sensitive measurement. Unlike normal FTS, which measures $\langle |E(\omega)|^2 \rangle$, SWIFTS measures $\langle E(\omega)E(\omega+\Delta\omega) \rangle$. Therefore the phase of the SWIFTS is the phase difference between adjacent comb lines. If that phase differences between each line of spectra can be recovered, then the phase of full electric field can, in principle, be recovered. In practice, this process is quite difficult and requires heavy statistical analysis. The reader is encouraged to study [8, 16] for more details. The time-domain profile of the electric field can be expressed as $E(t) = \sum_n E_n e^{-i\omega_n t}$, where ω_n is the field frequency and E_n is its associated phasor. If the phasors can be deduced, the instantaneous field intensity

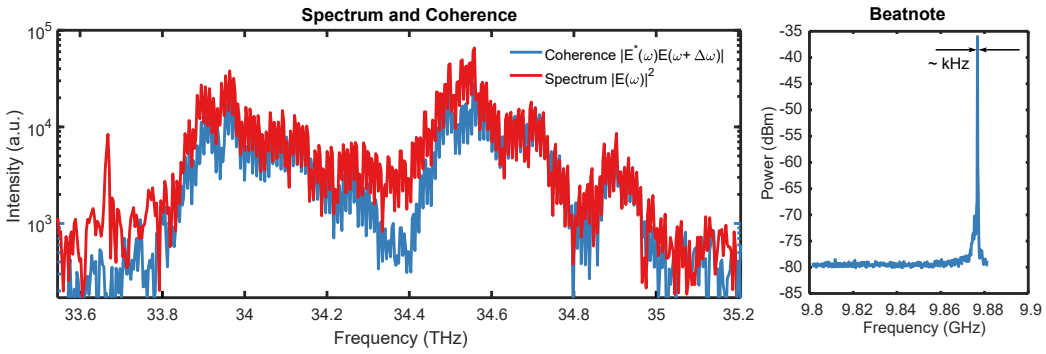

Figure 6-8: **Example SWIFTS result** Both the normal FTS spectra (red) and SWIFTS spectra (blue) plotted on top of one another. Regions of strong overlap are highly coherent. The SWIFTS shows a portion of the spectral region that is phase incoherent even though the FWHM of the electrical beatnote is narrow (kHz).

and frequency can be found from

$$I(t) = E^*(t)E(t) \tag{6.8}$$

$$f(t) = \frac{1}{2\pi|E(t)|^2}\mathrm{Im}\left[E^*(t)\frac{\mathrm{d}E(t)}{\mathrm{d}t}\right]. \tag{6.9}$$

.

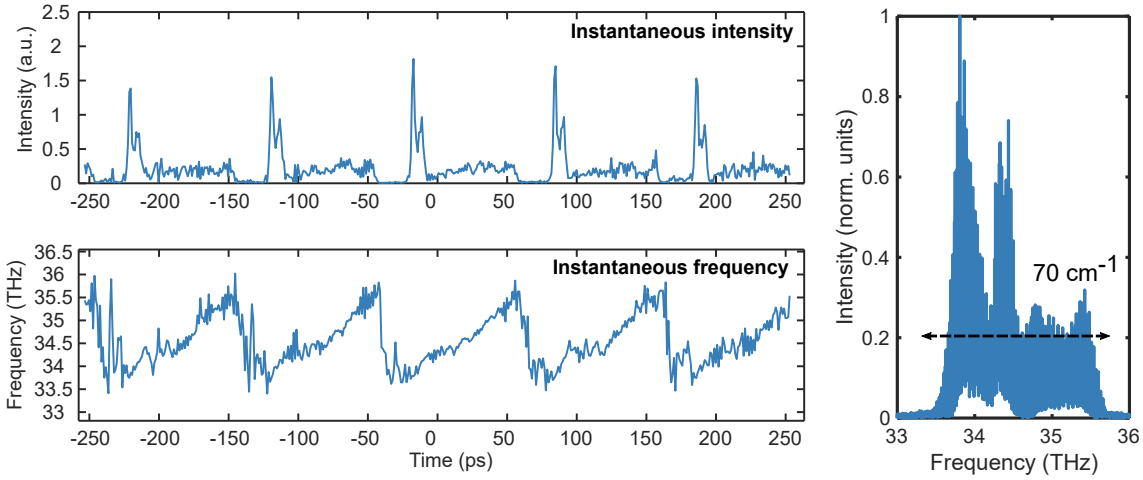

Figure 6-9: **Time-resolved electric field profile** The instantaneous electric field intensity and frequency are extracted from SWIFTS. The device exhibits a linear frequency chirp in time from 33.5 THz to 35.5 THz. Small increases in optical intensity are a result of the frequency turn-around in resetting the chirp.

Fig. 6-9 shows the electric field profile for the same device found using the aforementioned equations biased at 1.2 A. The dense spectra spanning 70 cm^{-1} is shown on the right panel. The intensity output the QCL comb is approximately constant in time with the exception of small jumps in the intensity with a periodicity of 100 ps, which is the round trip time of the cavity. The instantaneous frequency, on the other hand, is not constant in time. In fact, the frequency is *linearly chirped*, and the intensity spikes in the time domain correspond to the frequency turn-around points. Unlike traditional mode-locked sources—which are amplitude modulated and emit periodic intensity pulses in time—QCL combs are frequency modulated, and the frequency is linearly chirped in time [1]. This linear chirp behavior is theoretically unexpected, but has been shown to exist in a plethora of different semiconductor sources [61, 62, 63, 64, 65].

SWIFTS rivals other pulse characterization techniques such as spectral phase interferometry for direct electric-field reconstruction (SPIDER) [66] or frequency-resolved optical gating (FROG) [67], moreover SWIFTS has the advantage requiring only linear optical elements. Recently, other techniques, such as Fourier-transform Analysis of Comb Emission (FACE) [68] have been developed to extract detailed phase information, but these techniques require the use of a reference comb device.

[1] Unless the gain spectra is discontinuous. In this case, the frequency is modulated as a boxcar [60]

Chapter 7

Modeling Frequency Comb Fields

Injection locking and comb formation have an intuitively pleasing interpretation in the frequency domain: laser lines are equidistant and phase locked. But one may wonder why the electric field in linearly chirped in time. Traditional methods for answering such a question involved solving the full Maxwell-Bloch equations (MBEs), which are a series of 10 coupled partial differential equations for the populations, coherences and electric fields of the system [69]. Such a task is numerically daunting. However, recent works [14] were able to simplify the full MBEs down to a set of two master equations, one for each direction of electric field propagation inside a Fabry-Pérot cavity. In addition, a mean-field approach [60] can be applied (with some approximations) to simplify the master equations down even further to achieve an equally intuitive explanation of comb formation in the time domain: the electric fields obey a nonlinear Schrödinger equation with a potential proportional to its phase.

7.1 Master equation for semiconductor lasers

Laser master equations were first developed by Hermann A. Haus in 1975 to describe mode-locking [70]. Since then, master equations have been used to describe a plethora of different optical phenomena. The master equation formalism works especially well for semiconductor lasers (specifically, QCLs) as it can be derived from first principles using the density matrix approach to a two-level system. What follows is not a

complete derivation, but the key steps are outlined. The reader is directed towards [14, 60] for a full derivation of the master equation for semiconductor lasers with fast gain dynamics.

The first assumption made is that the electric field that propagates inside a Fabry-Pérot cavity is comprised of a right-moving wave (denoted by E_+) and a left-moving wave (denoted by E_-) with slowly-varying envelopes:

$$E(z,t) = E_+(z,t)e^{i(\omega_0 t - k_0 z)} + E_-(z,t)e^{i(\omega_0 t - k_0 z)} + \text{c.c.} \tag{7.1}$$

To account for spatial-hole burning (SHB)—which triggers multimode operation—all populations and coherences in the two-level system are assumed to have a spatially-varying grating at the fundamental frequency of the cavity. The density matrix is then evolved using the von Neumann equation, which creates a set of coupled equations describing the time evolution of the populations and coherences of the system. These equations, coupled with the wave equation, 4.7, can be used to show:

$$\left(\frac{n}{c}\frac{\partial}{\partial t} - \frac{\partial}{\partial z}\right)E_\pm + \frac{\alpha_w}{2}E_\pm - i\frac{1}{2}k''\frac{\partial^2 E_\pm}{\partial t^2} = i\frac{1}{2\omega_0 n\epsilon_0 c}\frac{\partial^2 P^{\text{NL}}}{\partial t^2}e^{-i(\omega_0 t \mp k_0 z)}, \tag{7.2}$$

where the effect of waveguide loss, α_m, and dispersion, k'' have also been included. All non-linear phenomena has been packaged on the RHS in the non-linear polarization. There are two non-linear effects that need to be considered for Fabry-Pérot QCLs. The first is the Kerr non-linearity and the second is the non-linearity that arises from the dynamics of the system.

Kerr non-linearity

The Kerr non-linearity is a $\chi^{(3)}$ effect in which the propagation of light inside a cavity can change the surrounding refractive index. The non-linear polarization term that arises from the Kerr effect can be derived in a similar manner to the non-linear

polarization for FWM:

$$P^{\mathrm{NL}} = \epsilon_0 \chi^{(3)} E(z,t)^3 \tag{7.3}$$

$$= 3\epsilon_0 \chi^{(3)} \left(|E_\pm|^2 + 2|E_\mp|^2 \right) E_\pm e^{i(\omega_0 t \mp k_0 z)}. \tag{7.4}$$

Therefore the Kerr term for the RHS of 7.2 can be easily calculated as

$$i \frac{1}{2\omega_0 n \epsilon_0 c} \frac{\partial^2 P^{\mathrm{NL}}}{\partial t^2} e^{-i(\omega_0 t \mp k_0 z)} = -i \frac{3\chi^{(3)} \omega_0}{2nc} \left(|E_\pm|^2 + 2|E_\mp|^2 \right) E_\pm \tag{7.5}$$

$$= -i\gamma_k \left(|E_\pm|^2 + 2|E_\mp|^2 \right) E_\pm, \tag{7.6}$$

where γ_k is known as the Kerr non-linearity.

System dynamics

The derivation for non-linearity that arises from the dynamics of the system is considerably more involved than the Kerr non-linearity. The starting point is the Bloch equations that describe the coherences, d, and population inversion, w, of a two-level system,

$$\dot{w} = \frac{2}{i\hbar} \left(d\mu^* a^* e^{-i\omega_0 t} - d^* \mu a e^{i\omega_0 t} \right) - \frac{w - w_0}{T_1} \tag{7.7}$$

$$\dot{d} = \frac{1}{i\hbar} w \mu a e^{i\omega_0 t} + \left(i\omega_0 - \frac{1}{T_2} \right). \tag{7.8}$$

Here, $a \equiv E_+ e^{-ik_0 z} + E_- e^{ik_0 z}$ represents the slowly-varying envelopes propagating in both directions, μ is the dipole matrix element, T_1 the population lifetime, T_2 is the coherence lifetime, and w_0 is the equilibrium population inversion. The non-linear polarization is found in terms of the atomic density N as

$$P^{\mathrm{NL}} = -N(\mu^* d + \mu d^*). \tag{7.9}$$

Although this is a simple expression, solving for the coherence as required by 7.9 is not an easy task. Furthermore, taking the second derivative of 7.9 is only possible

by approximating the derivatives in a power-series. The final expression (neglecting unimportant terms) is simply stated here for completeness. The RHS of 7.2 is given by

$$i\frac{1}{2\omega_0 n\epsilon_0 c}\frac{\partial^2 P^{\mathrm{NL}}}{\partial t^2}e^{-i(\omega_0 t\mp k_0 z)} = \frac{g_0}{2}\left(1-\frac{1}{P_s}\left(|E_\pm|^2+2|E_\mp|^2\right)\right)E_\pm + \frac{g_0}{2}T_2^2\frac{\partial^2 E_\pm}{\partial t^2} + \frac{g_0}{2P_s}\left((2T_1+3T_2)\frac{\partial E_\mp^*}{\partial t}E_\mp + (T_1+\frac{5}{2}T_2)E_\mp^*\frac{\partial E_\mp}{\partial t}\right)E_\pm. \tag{7.10}$$

Here, many variables have been hidden by two constants: $g_0 = \frac{ez_0^2\omega_0 JT_1T_2}{n\epsilon_0 c\hbar L_{\mathrm{mod}}}$, which is the small signal gain, and $P_s = \left(\frac{4T_1T_2}{\hbar^2}|\mu|^2\right)^{-1}$, which is the saturation intensity. Therefore, the full master equation is given by

$$\left(\frac{n}{c}\frac{\partial}{\partial t}-\frac{\partial}{\partial z}\right)E_\pm + \frac{\alpha_w}{2}E_\pm - i\frac{1}{2}k''\frac{\partial^2 E_\pm}{\partial t^2} = \frac{g_0}{2}\left(1-\frac{1}{P_s}\left(|E_\pm|^2+2|E_\mp|^2\right)\right)E_\pm + \frac{g_0}{2}T_2^2\frac{\partial^2 E_\pm}{\partial t^2} + \frac{g_0}{2P_s}\left((2T_1+3T_2)\frac{\partial E_\mp^*}{\partial t}E_\mp + (T_1+\frac{5}{2}T_2)E_\mp^*\frac{\partial E_\mp}{\partial t}\right)E_\pm. \tag{7.11}$$

The red terms represent gain saturation, as when the field intensities approach P_s, the gain depletes to zero. The blue represents gain curvature, which will ultimately limit the bandwidth of the frequency comb. The green terms represent cross-interactions between the forward the backward propagating electric fields, otherwise known as cross-steepening.

Now that a full-field master equation has been derived, it can be numerically integrated over many thousands of cavity round trips to provide valuable insight on the electric field propagating inside the cavity. This includes the instantaneous frequency of the field, spectral components as well as its phase coherence. Numerically solving 7.11, however, is easier said then done.

7.2 Mean-field theory for QCL combs

The methods described in section 7.1 are completely general, and can be used to analyze any semiconductor laser with fast gain dynamics—not just QCLs. However, integrating 7.11 is numerically intensive, as each cavity round trip must be subdivided to into a fine mesh to capture the dynamics of the fields. In the Kerr micro-resonator community, this issue was solved by noting the intracavity field intensity is relatively constant over a round trip, and can be averaged to greatly lighten the numerical load [71]. This approach—known as the Lugiato-Lefever equation (LLE)—provided valuable insight on the formation of comb states in passive media. Unfortunately, the same approximations cannot be made for Fabry-Pérot QCLs. The intracavity field changes rapidly over a round trip, with large mirror losses at each facet. Therefore, averaging the fields in their usual form leads to non-physical results.

It was only recently that a mean-field approach was developed for QCL combs. Details of the mean-field derivation can be found in the supplemental information of [60]. The heart of the approach is to normalize the electric field to the steady-state output of the laser by defining an intensity envelope function, $F(z,t)$, which contains all the gain dynamics,

$$E(z,t) \equiv F(z,t) \exp\left(\frac{1}{2}\int_0^z \mathrm{d}z \left\{g_{\text{eff}}(z')\right\}\right) \equiv F(z,t)K^{1/2}(z), \tag{7.12}$$

where g_{eff} is the effective gain of the system and $K(z)$ is the dimensionless power gain the field experiences when propagating to a point z inside the cavity. 7.12 is then substituted into 7.11 and integrated over a single round trip through the cavity (with some additional approximations) to find

$$\begin{aligned}\frac{\partial F}{\partial t} = -\frac{1}{3}r\left(|F|^2 + 2\langle K\rangle^{-1}\,\tilde{K}[|F|^2] - 3P_0\right)F + i\frac{1}{2}\beta\frac{\partial^2 F}{\partial z^2} + \frac{1}{4}D_g\frac{\partial^2 F}{\partial z^2} \\ -\tilde{K}\left[\gamma_1\frac{\partial F^*}{\partial z}F + \gamma_2 F^*\frac{\partial F}{\partial z}\right]F.\end{aligned} \tag{7.13}$$

7.13 requires some discussion. T represents *slow time*, which comes from the integration over a round trip time, T_r, as apposed to *fast time*, t. The average value of K is

Parameter	Symbol	Value	Unit
Current density	J	1200	$\mathrm{A/cm^2}$
Dispersion	k''	800	$\mathrm{fs^2/mm}$
Kerr non-linearity	γ_k	3.5×10^{-11}	$\mathrm{m/V^2}$
Facet 1 reflectivity	R_1	0.09	unitless
Facet 2 reflectivity	R_1	1.0	unitless
Wavelength	λ	8	μm
Cavity length	L	4.5	mm
Population lifetime	T_1	0.4	ps
Coherence lifetime	T_2	50	ps
Refractive index	n	3.3	unitless
Dipole matrix element	μ	2.3	nm
Module length	L_{mod}	58	nm
Waveguide loss	α_{w}	4	$\mathrm{cm^{-1}}$

Table 7.1: **Simulation parameters for mean-field theory**

$\langle K \rangle \equiv \frac{1}{2L_c}\int_0^{2L_c} \mathrm{d}u\{K(u)\}$ and $\tilde{K}[f](z) \equiv \frac{1}{4L_c}\int_0^{4L_c} \mathrm{d}u\left\{K\left(-\frac{u}{2}\right) f(z-u)\right\}$ represents the convolution of K with the bracketed function f, $\beta \equiv k''\left(\frac{c}{n}\right)^3$ is the normalized dispersion, $r \equiv 3\frac{g_0}{2P_w}\frac{c}{n}\langle K \rangle$ represents energy relaxation, $\gamma_1 \equiv \frac{g_0}{2P_s}\left(\frac{c}{n}\right)^2(2T_1+3T_2)$ and $\gamma_2 \equiv \frac{g_0}{2P_s}\left(\frac{c}{n}\right)^2\left(T_1+\frac{5}{2}T_2\right)$ are "cross-steepening" terms, and $D_g \equiv 2g_0T_2^2\left(\frac{c}{n}\right)^3$ is the gain curvature.

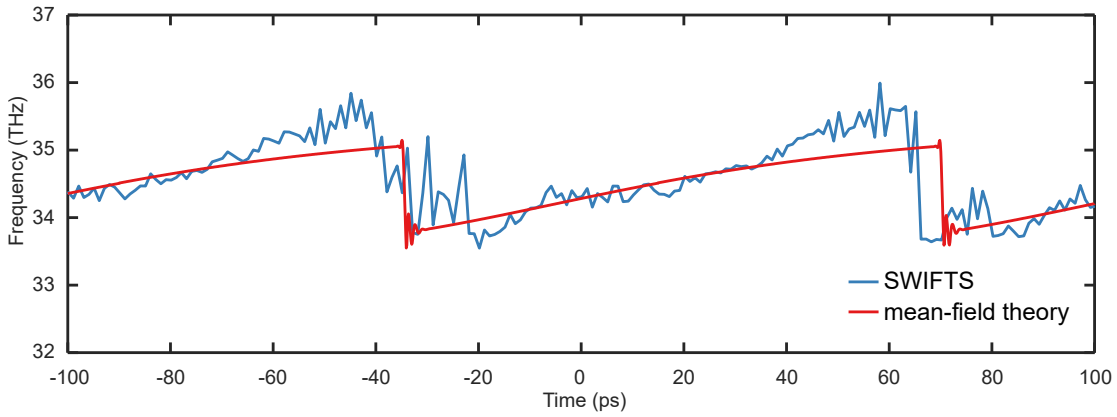

Figure 7-1: **Mean-field theory with SWIFTS result** The time-domain electric field frequency of a Thorlabs QCL (H0355) extracted from SWIFTS (blue) compared to the mean-field theory (red).

7.13 can now be easily integrated using common techniques such as the split-step

method. Fig. 7-1 shows the result of integrating 7.13 over 20,000 round trips using the parameters listed in Table 7.1 compared to the SWIFTS data from a Thorlabs QCL biased at 1.2 A. The mean-field theory accurately predicts the linear frequency chirping and the two curves agree qualitatively.

But one may wonder where the linear chirping behavior arises from. The answer is the large cross-steepening the field experiences when the wave is reflected at either facet. The phase of the field experiences positive feedback due to the counter-propagation, leading to the parabolic phase profile [60]. The interaction of the field with the counter-propagating wave is the reason this FM behavior has been only seen in Fabry-Pérot cavities; ring resonators do not have facets to facilitate such an interaction.

This can be shown mathematically by approximating the derivatives in the cross-steepening terms as $\frac{\partial F^*}{\partial z}F = -i\frac{\partial \phi}{\partial z}A$, where A and ϕ are the amplitude and phase of F. Assuming the non-linear gain is of the form [1]

$$g_{\mathrm{NL}} = i(\gamma_1 - \gamma_2)\frac{|F|^2}{P_0}\frac{\Delta P}{4L_c}(\phi - \langle\phi\rangle), \tag{7.14}$$

where ΔP represents the power discontinuity at the first facet, one can simplify the mean-field theory down to a nonlinear Schrödinger equation (NLSE)

$$-i\frac{\partial F}{\partial T} = \frac{\beta}{2}\frac{\partial^2 F}{\partial z^2} + \gamma|F|^2(\phi - \langle\phi\rangle)F + ir(|F|^2 - P_0)F. \tag{7.15}$$

Here, $\gamma \equiv (\gamma_1 - \gamma_2)\frac{\Delta P}{4L_c P_0}$ is the normalize cross-steepening. NLSEs are typically used in optics to describe optical fibers, and are intensity dominated equations. 7.15, on the other hand, is a phase dominated equation. As a result, an analytical solution can be found of the form

$$F(z,T) = A_0 \exp\left[i\frac{\gamma|A_0|^2}{2\beta}\left(z^2 - \frac{1}{3}L_c^2\gamma|A_0|^2T\right)\right], \tag{7.16}$$

which exactly describes the FM behavior shown in both SWIFTS and the mean-field

[1] under the assumption of no gain curvature.

theory. The parabolic phase profile in the exponential leads to a linear frequency chirp. In fact, the analytical abilities of the mean-field theory allow one to write down all that contributes the linear chirp behavior in terms of fundamental laser parameters:

$$\Delta f = \frac{L_c}{12\pi}\alpha_{\mathrm{m}}(g_0 - \alpha_{\mathrm{w}} - \alpha_{\mathrm{m}})k^{''-1}\left(T_1 + \frac{1}{2}T_2\right). \tag{7.17}$$

Notably, FM behavior required large mirror losses, α_{m}, and small dispersion, $k^{''}$, both of which are present in Fabry-Pérot QCLs.

Chapter 8

Conclusion

In summary, a general study of frequency combs based on mid-IR QCLs has been conducted. Devices were fabricated via wet and dry etching methods from bare wafers grown by Thorlabs. Devices were tested and characterized to determine the laser dispersion. Using this information, dispersion compensators based on DCMs were fabricated to facilitate FWM to lock the lasers lines. Initial results show that the large thermal transience experienced by the QCL during one pulse-bias cycle prevents stable comb operation. This result motivated further fabrication steps to handle the increased thermal load of CW biasing the laser at room temperature.

Coherence techniques, such as beatnote analysis and SWIFTS, were conducted on a Thorlabs QCL to evaluate its comb performance. The time-domain electric field profile extracted from SWIFTS shows a linearly chirped FM output. This behavior agrees well with theoretical analysis based on laser master equations and mean-field theories.

Although room temperature frequency combs have not been fabricated in-house thus far, several devices that CW lased at cryogenic temperature showed narrow beatnotes, indicative of comb-like behavior. Additionally, room temperature CW lasing was recently achieved. The path forward to achieve robust, room temperature frequency combs is clear. Once lasers can consistently handle the thermal load of CW bias at room temperature, dispersion measurements can be taken, and dispersion compensators can be designed.

Appendix A

Numerical Methods for Modeling QCLs

Many different methods have been proposed for solving 2.21, such as the finite difference method [72] and spectral element method [73]. The most popular method, however, is the shooting method. The shooting method goes as follows. Initial guesses for solutions to 2.21 are made based on boundary conditions on one side of the structure, those guesses are "shot" through the simulation domain via propagation matrices, and boundary conditions on the side are used to make corrections to the initial guesses. This process is repeated and refined until all solutions are found.

A.1 Numerical methods

A.1.1 Material parameters and grid discretization

In order to apply the shooting method, the simulation domain must be established. At each point in the simulation domain, several material parameters must be specified: the Kane energy E_{p}, the conduction band energy, E_{c}, the light hole energy, E_{lh} and the split-off band energy, E_{so}. Fortunately (for mid-IR QCLs) these parameters are well-established [x], with the only exception being E_{p}. Instead of using tabulated values, E_{p} is found at the band edge and compared to literature values of effective mass. This

ensure consistency when dealing with low-energy electrons. Strain effects on these parameters for stacked III-V semiconductors can also be accounted for accordingly [74].

In general, simulations should be performed over several modules of a QCL (3, for example), and only the center module wavefunctions should be trusted. Edge effects can significantly perturb wavefunction calculations. A discretization mesh of 5-10 nodes per monolayer of material is generally sufficient in capturing all of the physics.

A.1.2 The shooting method

Consider the simulation domain shown in Fig. A-1. Each node point i is a blue or red dot, depending the material domain. The Schrödinger equation is solved for between each node point, denoted by node spacing l_i. The Schrödinger equation can be split

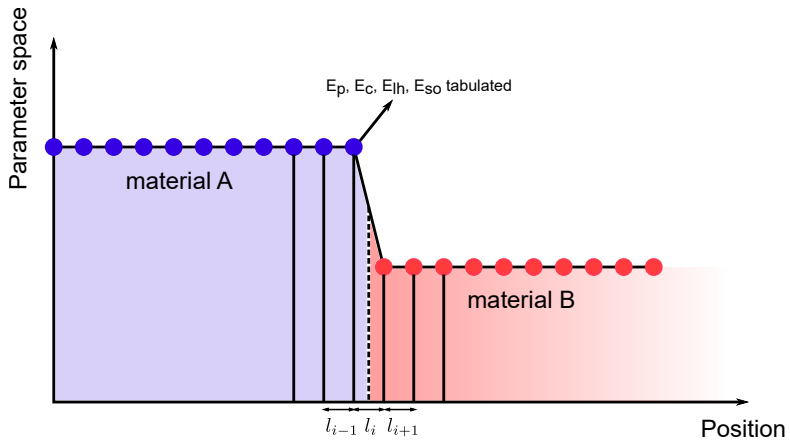

Figure A-1: **Simulation domain for QCLs** Each node contains all parameters necessary for calculations.

from one second order differential equation to two first order differential equations by defining a placeholder function g_c. 2.21 becomes

$$-\frac{\hbar^2}{2}\frac{\partial g_c}{\partial z} = (E - E_c(z))f_c \tag{A.1}$$

$$g_c = \frac{1}{m^*(E,z)}\frac{\partial f_c}{\partial z}. \tag{A.2}$$

Without loss of generality, the solutions of f_c and g_c in layer i can be written as

$$f_{c,i} = Ae^{ik_i z_i} + Be^{-ik_i z_i}, \text{ and} \tag{A.3}$$

$$g_{c,i} = \frac{ik_i}{m_i^*} Ae^{ik_i z_i} - \frac{ik_i}{m_i^*} Be^{-ik_i z_i}, \tag{A.4}$$

where $k_i = \sqrt{\frac{2m^*(E-E_{c,i})}{\hbar^2}}$. Starting at the "left" of the simulation $z = 0$, these equations can be written in matrix form to find constants A and B,

$$\begin{pmatrix} A \\ B \end{pmatrix} = \frac{1}{2} \begin{pmatrix} 1 & \frac{m^*}{ik_0} \\ 1 & -\frac{m^*}{ik_0} \end{pmatrix} \begin{pmatrix} f_{c,0} \\ g_{c,0} \end{pmatrix}. \tag{A.5}$$

It can be thus shown that f_c and g_c at the next node point are

$$\begin{pmatrix} f_{c,1} \\ g_{c,1} \end{pmatrix}. = \begin{pmatrix} e^{ik_1 l_1} & e^{-ik_1 l_1} \\ \frac{ik_1}{m_1^*} e^{ik_1 l_1} & -\frac{ik_1}{m_1^*} e^{-ik_1 l_1} \end{pmatrix} \frac{1}{2} \begin{pmatrix} 1 & \frac{m_0^*}{ik_0} \\ 1 & -\frac{m_0^*}{ik_0} \end{pmatrix} \begin{pmatrix} f_{c,0} \\ g_{c,0} \end{pmatrix} \tag{A.6}$$

or

$$\begin{pmatrix} f_{c,1} \\ g_{c,1} \end{pmatrix} = \begin{pmatrix} \cos k_1 l_1 & \frac{m_0^*}{k_0} \sin k_1 l_1 \\ -\frac{m_0^*}{k_0} \sin k_1 l_1 & \cos k_1 l_1 \end{pmatrix} \begin{pmatrix} f_{c,0} \\ g_{c,0} \end{pmatrix}. \tag{A.7}$$

A.7 can be used iteratively to propagate initial guesses for f_c and g_c across the simulation domain. The matrix nature of the evolution allows for fast computations. The shot f_c for a particular energy E is considered a true bound state if it obeys the boundary condition on the right-hand side of the domain: f_c goes toward zero. If this condition is satisfied, f_c is envelope for a wavefunction and E is its eigenenergy.

In practice this is first done by placing energy bounds via bisection on all possible solutions by counting the number zero crossing each shot f_c has. For example, if at a particular energy, E_i, the $f_{c,i}$ has three zeros crossing and at a higher energy, E_j, $f_{c,j}$ has five zero crossing, a bound state of four zeros crossings must exist between energies E_i and E_j. The true eigenenergy, $E_{:)}$, is then found via a bounded root-finding algorithm.

A.1.3 The Hartree potential

Electron densities in QCLs are typically on the order of 10^{16} to 10^{17} cm^{-3}, which means their space-charge effects on the wavefunctions cannot be neglected. These effects are typically treated in a mean-field approximation though the addition of a Hartree potential, $V_{\mathrm{H}}(z)$, to the Hamiltonian. The Hartree potential is computed from the local charge distribution, $\rho(z)$, via the Poisson equation,

$$\frac{\partial}{\partial z}\left(\epsilon(z)\frac{\partial V_{\mathrm{H}}(z)}{\partial z}\right) = -\rho(z), \tag{A.8}$$

with appropriate boundary conditions. $\rho(z)$ is calculated from

$$\rho(z) = eN_{\mathrm{D}}(z) - e\sum_i n_i|f_i|^2, \tag{A.9}$$

where e is the charge of the electron, $N_{\mathrm{D}}(z)$ is the ionized dopant distribution, $|f_i|^2$ is the probability density for subband i, and n_i is the surface electron density in subband i.

In principle, the only way to calculate n_i is through transport modeling of QCLs; however, this is time consuming and often not necessary for quick calculations, such as the ones made in this thesis. A good (although not justified) model for n_i is that of a thermal distribution across each subband. The thermal distribution is characterized by a Fermi distribution with chemical potential μ, such that charge neutrality ($\int \rho(z)dz = 0$) is maintained:

$$n_i = \int D_i(E)f(E,\mu)dE, \tag{A.10}$$

where $D_i(E) = \frac{m_i^*}{\pi\hbar^2}\Theta(E - E_i)$ is the two-dimensional density of states for subband i with eigenenergy E_i and $f(E,\mu)$ is the Fermi distribution. Solutions to A.8 are found using similar methods described in A.1.2: initial guesses for $V_{\mathrm{H}}(0)$ are made, $V_{\mathrm{H}}(z)$ is found by applying the shooting method on A.8, boundary conditions ($V_{\mathrm{H}}(z)$ goes toward 0) are checked, and the initial guess is refined until convergence.

Careful considerations must be made when solving for the Hartree potential across multiple modules; the periodicity of $V_{\mathrm{H}}(z)$ must be the same as the periodicity of the QCL. In other words, the 2D electron densities (and hence, the wavefunctions) must be periodic. To ensure this, only wavefunctions localized in the center module are thermally populated. Those wavefunctions and populations are then copied to the neighboring modules and shifted in both real space and energy space accordingly. All other wavefunctions are discarded.

Perturbations to the wavefunctions via the Hartree potential are often significant. Therefore wavefunctions must be found *self-consistently* through multiple iterations of solving the Schrödinger equation and Poisson equation. A flow-chart for a typical calculation is shown in Fig. A-2

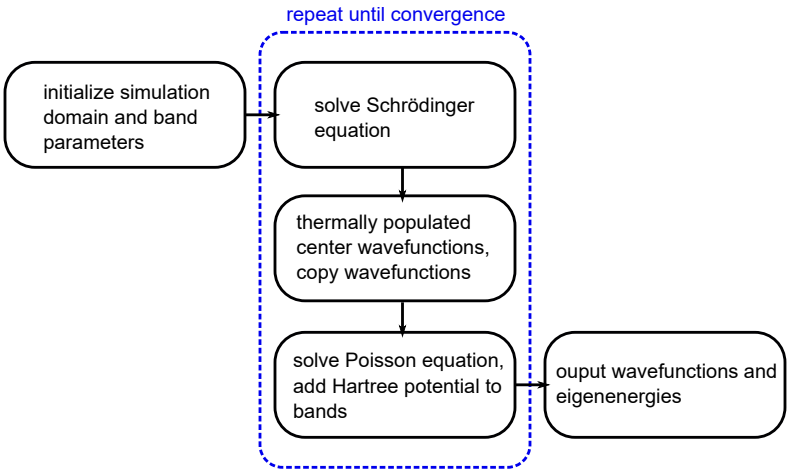

Figure A-2: **Flow chart for QCL band-structure calculation** The steps involved in calculating the bandstructure of QCLs.

Bibliography

[1] I. Coddington, N. Newbury, and W. Swann, "Dual-comb spectroscopy," *Optica*, vol. 3, pp. 414–426, Apr 2016.

[2] S. Kumar, *Development of terahertz quantum-cascade lasers*. PhD thesis, 2007.

[3] H. K. Lee and J. S. Yu, "Thermal effects in quantum cascade lasers at ∼4.6 m under pulsed and continuous-wave modes," *Applied Physics B*, vol. 106, pp. 619–627, Oct. 2011.

[4] A. Schliesser, N. Picqué, and T. W. Hänsch, "Mid-infrared frequency combs," *Nature Photonics*, vol. 6, pp. 440–449, Jul 2012.

[5] A. Hugi, G. Villares, S. Blaser, H. C. Liu, and J. Faist, "Mid-infrared frequency comb based on a quantum cascade laser," *Nature*, vol. 492, pp. 229–233, Dec. 2012.

[6] D. Burghoff, "Frequency-modulated combs: origins and opportunities," in *Terahertz Emitters, Receivers, and Applications XII* (M. Razeghi and A. N. Baranov, eds.), SPIE, Aug. 2021.

[7] K. C. Cossel, E. M. Waxman, F. R. Giorgetta, M. Cermak, I. R. Coddington, D. Hesselius, S. Ruben, W. C. Swann, G.-W. Truong, G. B. Rieker, and N. R. Newbury, "Open-path dual-comb spectroscopy to an airborne retroreflector," *Optica*, vol. 4, pp. 724–728, Jul 2017.

[8] D. Burghoff, T.-Y. Kao, N. Han, C. W. I. Chan, X. Cai, Y. Yang, D. J. Hayton, J.-R. Gao, J. L. Reno, and Q. Hu, "Terahertz laser frequency combs," *Nature Photonics*, vol. 8, pp. 462–467, May 2014.

[9] J. Hillbrand, P. Jouy, M. Beck, and J. Faist, "Tunable dispersion compensation of quantum cascade laser frequency combs," *Optics Letters*, vol. 43, p. 1746, Apr. 2018.

[10] Y. Bidaux, I. Sergachev, W. Wuester, R. Maulini, T. Gresch, A. Bismuto, S. Blaser, A. Muller, and J. Faist, "Plasmon-enhanced waveguide for dispersion compensation in mid-infrared quantum cascade laser frequency combs," *Optics Letters*, vol. 42, p. 1604, Apr. 2017.

[11] D. Burghoff, Y. Yang, J. L. Reno, and Q. Hu, "Dispersion dynamics of quantum cascade lasers," *Optica*, vol. 3, p. 1362, Nov. 2016.

[12] A. Gordon, C. Y. Wang, L. Diehl, F. X. Kärtner, A. Belyanin, D. Bour, S. Corzine, G. Höfler, H. C. Liu, H. Schneider, T. Maier, M. Troccoli, J. Faist, and F. Capasso, "Multimode regimes in quantum cascade lasers: From coherent instabilities to spatial hole burning," *Physical Review A*, vol. 77, May 2008.

[13] D. Burghoff, "Unraveling the origin of frequency modulated combs using active cavity mean-field theory," *Optica*, vol. 7, p. 1781, Dec. 2020.

[14] N. Opačak and B. Schwarz, "Theory of frequency-modulated combs in lasers with spatial hole burning, dispersion, and kerr nonlinearity," *Physical Review Letters*, vol. 123, Dec. 2019.

[15] Z. Han, D. Ren, and D. Burghoff, "Sensitivity of SWIFT spectroscopy," *Optics Express*, vol. 28, p. 6002, Feb. 2020.

[16] D. Burghoff, Y. Yang, D. J. Hayton, J.-R. Gao, J. L. Reno, and Q. Hu, "Evaluating the coherence and time-domain profile of quantum cascade laser frequency combs," *Optics Express*, vol. 23, p. 1190, Jan. 2015.

[17] B. Lax, "[111] direct transition exciton and magnetoreflection in germanium," *Physical Review Letters*, vol. 4, pp. 511–513, May 1960.

[18] K. Unterrainer, C. Kremser, C. Wurzer, E. Gornik, P. Pfeffer, W. Zawadzki, B. Murdin, and C. R. Pidgeon, "Tunable cyclotron resonance-laser in p-ge," *Semiconductor Science and Technology*, vol. 7, pp. B604–B609, Mar. 1992.

[19] R. F. Kazarinov and R. A. Suris, "Possibility of amplification of electromagnetic waves in a semiconductor with superlattice," *Sov. Phys.-Semicond.*, vol. 5, no. 4, pp. 707–709, 1971.

[20] F. Capasso, K. Mohammed, and A. Cho, "Resonant tunneling through double barriers, perpendicular quantum transport phenomena in superlattices, and their device applications," *IEEE Journal of Quantum Electronics*, vol. 22, pp. 1853–1869, Sept. 1986.

[21] J. E. Davey and T. Pankey, "Epitaxial GaAs films deposited by vacuum evaporation," *Journal of Applied Physics*, vol. 39, pp. 1941–1948, Mar. 1968.

[22] A. Cho and J. Arthur, "Molecular beam epitaxy," *Progress in Solid State Chemistry*, vol. 10, pp. 157–191, Jan. 1975.

[23] L. L. Chang, L. Esaki, and R. Tsu, "Resonant tunneling in semiconductor double barriers," *Applied Physics Letters*, vol. 24, pp. 593–595, June 1974.

[24] F. Capasso, K. Mohammed, and A. Y. Cho, "Sequential resonant tunneling through a multiquantum well superlattice," *Applied Physics Letters*, vol. 48, pp. 478–480, Feb. 1986.

[25] J. Faist, F. Capasso, D. L. Sivco, C. Sirtori, A. L. Hutchinson, and A. Y. Cho, "Quantum cascade laser," *Science*, vol. 264, pp. 553–556, Apr. 1994.

[26] J. Faist, F. Capasso, C. Sirtori, D. L. Sivco, A. L. Hutchinson, and A. Y. Cho, "Continuous wave operation of a vertical transition quantum cascade laser above t=80 k," *Applied Physics Letters*, vol. 67, pp. 3057–3059, Nov. 1995.

[27] J. Faist, F. Capasso, C. Sirtori, D. L. Sivco, J. N. Baillargeon, A. L. Hutchinson, S.-N. G. Chu, and A. Y. Cho, "High power mid-infrared (∼5 m) quantum cascade lasers operating above room temperature," *Applied Physics Letters*, vol. 68, pp. 3680–3682, June 1996.

[28] M. Beck, "Continuous wave operation of a mid-infrared semiconductor laser at room temperature," *Science*, vol. 295, pp. 301–305, Dec. 2001.

[29] R. Köhler, A. Tredicucci, F. Beltram, H. E. Beere, E. H. Linfield, A. G. Davies, D. A. Ritchie, R. C. Iotti, and F. Rossi, "Terahertz semiconductor-heterostructure laser," *Nature*, vol. 417, pp. 156–159, May 2002.

[30] Thorlabs, "Quantum and interband cascade lasers (qcls and icls), 3 - 11 m." Available at `https://www.thorlabs.com/newgrouppage9.cfm?objectgroup_id=6932` (2021/08/23).

[31] A. Hugi, R. Terazzi, Y. Bonetti, A. Wittmann, M. Fischer, M. Beck, J. Faist, and E. Gini, "External cavity quantum cascade laser tunable from 7.6 to 11.4 m," *Applied Physics Letters*, vol. 95, p. 061103, Aug. 2009.

[32] C. K. Akhgar, G. Ramer, M. Żbik, A. Trajnerowicz, J. Pawluczyk, A. Schwaighofer, and B. Lendl, "The next generation of IR spectroscopy: EC-QCL-based mid-IR transmission spectroscopy of proteins with balanced detection," *Analytical Chemistry*, vol. 92, pp. 9901–9907, June 2020.

[33] Y. Wang, M. G. Soskind, W. Wang, and G. Wysocki, "High-resolution multi-heterodyne spectroscopy based on fabry-perot quantum cascade lasers," *Applied Physics Letters*, vol. 104, p. 031114, Jan. 2014.

[34] H. Callebaut and Q. Hu, "Importance of coherence for electron transport in terahertz quantum cascade lasers," *Journal of Applied Physics*, vol. 98, p. 104505, Nov. 2005.

[35] C. Jirauschek, "Density matrix monte carlo modeling of quantum cascade lasers," *Journal of Applied Physics*, vol. 122, p. 133105, Oct. 2017.

[36] H. Callebaut, *Analysis of the electron transport properties in quantum cascade lasers*. PhD thesis, 2006.

[37] C. Jirauschek and T. Kubis, "Modeling techniques for quantum cascade lasers," *Applied Physics Reviews*, vol. 1, p. 011307, Mar. 2014.

[38] A. Khalatpour, *New frontiers in THz quantum cascade lasers*. PhD thesis, 2020.

[39] G. Bastard and J. Schulman, "Wave mechanics applied to semiconductor heterostructures," *Physics Today*, vol. 45, pp. 103–105, Feb. 1992.

[40] E. O. Kane, "Band structure of indium antimonide," *Journal of Physics and Chemistry of Solids*, vol. 1, pp. 249–261, Jan. 1957.

[41] D. P. Burghoff, "Characterization of mid-infrared quantum cascade lasers," Master's thesis, 2009.

[42] J. Faist, *Quantum Cascade Lasers*. Oxford University Press, Mar. 2013.

[43] A. Khalatpour, A. K. Paulsen, C. Deimert, Z. R. Wasilewski, and Q. Hu, "High-power portable terahertz laser systems," *Nature Photonics*, vol. 15, pp. 16–20, Nov. 2020.

[44] P. Jouy, J. M. Wolf, Y. Bidaux, P. Allmendinger, M. Mangold, M. Beck, and J. Faist, "Dual comb operation of $\sim$ 8.2 m quantum cascade laser frequency comb with 1 w optical power," *Applied Physics Letters*, vol. 111, p. 141102, Oct. 2017.

[45] T. Zeng, "Long-wave infrared frequency combs based on quantum cascade lasers," Master's thesis, 2017.

[46] M. Piccardo, B. Schwarz, D. Kazakov, M. Beiser, N. Opačak, Y. Wang, S. Jha, J. Hillbrand, M. Tamagnone, W. T. Chen, A. Y. Zhu, L. L. Columbo, A. Belyanin, and F. Capasso, "Frequency combs induced by phase turbulence," *Nature*, vol. 582, pp. 360–364, June 2020.

[47] D. Kazakov, M. Piccardo, Y. Wang, P. Chevalier, T. S. Mansuripur, F. Xie, C. en Zah, K. Lascola, A. Belyanin, and F. Capasso, "Self-starting harmonic frequency comb generation in a quantum cascade laser," *Nature Photonics*, vol. 11, pp. 789–792, Oct. 2017.

[48] M. Piccardo, P. Chevalier, S. Anand, Y. Wang, D. Kazakov, E. A. Mejia, F. Xie, K. Lascola, A. Belyanin, and F. Capasso, "Widely tunable harmonic frequency comb in a quantum cascade laser," *Applied Physics Letters*, vol. 113, p. 031104, July 2018.

[49] M. Piccardo, P. Chevalier, T. S. Mansuripur, D. Kazakov, Y. Wang, N. A. Rubin, L. Meadowcroft, A. Belyanin, and F. Capasso, "The harmonic state of quantum cascade lasers: origin, control, and prospective applications [invited]," *Optics Express*, vol. 26, p. 9464, Apr. 2018.

[50] P. Del'Haye, A. Schliesser, O. Arcizet, T. Wilken, R. Holzwarth, and T. J. Kippenberg, "Optical frequency comb generation from a monolithic microresonator," *Nature*, vol. 450, pp. 1214–1217, Dec. 2007.

[51] D. P. Burghoff, *Broadband terahertz photonics*. PhD thesis, 2014.

[52] R. Boyd, *Nonlinear Optics*. San Diego, California: Academic Press, 4 ed., 2020.

[53] A. E. Siegman, *Lasers*. Mill Valley, California: University Science Books, 1986.

[54] Y. Yang, D. Burghoff, J. Reno, and Q. Hu, "Achieving comb formation over the entire lasing range of quantum cascade lasers," *Optics Letters*, vol. 42, p. 3888, Sept. 2017.

[55] J. Faist, G. Villares, G. Scalari, M. Rösch, C. Bonzon, A. Hugi, and M. Beck, "Quantum cascade laser frequency combs," *Nanophotonics*, vol. 5, pp. 272–291, June 2016.

[56] B. W. Hakki and T. L. Paoli, "cw degradation at 300k of GaAs double-heterostructure junction lasers. II. electronic gain," *Journal of Applied Physics*, vol. 44, pp. 4113–4119, Sept. 1973.

[57] C. Dorrer, N. Belabas, J.-P. Likforman, and M. Joffre, "Spectral resolution and sampling issues in fourier-transform spectral interferometry," *Journal of the Optical Society of America B*, vol. 17, p. 1795, Oct. 2000.

[58] Y. Yang, D. Burghoff, D. J. Hayton, J.-R. Gao, J. L. Reno, and Q. Hu, "Terahertz multiheterodyne spectroscopy using laser frequency combs," *Optica*, vol. 3, p. 499, May 2016.

[59] B. Levine, "Quantum-well infrared photodetectors," *Journal of applied physics*, vol. 74, no. 8, pp. R1–R81, 1993.

[60] D. Burghoff, "Unraveling the origin of frequency modulated combs using active cavity mean-field theory," *Optica*, vol. 7, p. 1781, Dec. 2020.

[61] M. Singleton, P. Jouy, M. Beck, and J. Faist, "Evidence of linear chirp in mid-infrared quantum cascade lasers," *Optica*, vol. 5, p. 948, Aug. 2018.

[62] J. Hillbrand, D. Auth, M. Piccardo, N. Opačak, E. Gornik, G. Strasser, F. Capasso, S. Breuer, and B. Schwarz, "In-phase and anti-phase synchronization in a laser frequency comb," *Physical Review Letters*, vol. 124, Jan. 2020.

[63] L. A. Sterczewski, C. Frez, S. Forouhar, D. Burghoff, and M. Bagheri, "Frequency-modulated diode laser frequency combs at 2 m wavelength," *APL Photonics*, vol. 5, p. 076111, July 2020.

[64] M. Piccardo, P. Chevalier, B. Schwarz, D. Kazakov, Y. Wang, A. Belyanin, and F. Capasso, "Frequency-modulated combs obey a variational principle," *Physical Review Letters*, vol. 122, June 2019.

[65] B. Schwarz, J. Hillbrand, M. Beiser, A. M. Andrews, G. Strasser, H. Detz, A. Schade, R. Weih, and S. Höfling, "Monolithic frequency comb platform based on interband cascade lasers and detectors," *Optica*, vol. 6, p. 890, July 2019.

[66] C. Iaconis and I. Walmsley, "Self-referencing spectral interferometry for measuring ultrashort optical pulses," *IEEE Journal of Quantum Electronics*, vol. 35, pp. 501–509, Apr. 1999.

[67] R. Trebino, K. W. DeLong, D. N. Fittinghoff, J. N. Sweetser, M. A. Krumbügel, B. A. Richman, and D. J. Kane, "Measuring ultrashort laser pulses in the time-frequency domain using frequency-resolved optical gating," *Review of Scientific Instruments*, vol. 68, pp. 3277–3295, Sept. 1997.

[68] L. Consolino, M. Nafa, F. Cappelli, K. Garrasi, F. P. Mezzapesa, L. Li, A. G. Davies, E. H. Linfield, M. S. Vitiello, P. D. Natale, and S. Bartalini, "Fully phase-stabilized quantum cascade laser frequency comb," *Nature Communications*, vol. 10, July 2019.

[69] Y. Wang and A. Belyanin, "Active mode-locking of mid-infrared quantum cascade lasers with short gain recovery time," *Optics Express*, vol. 23, p. 4173, Feb. 2015.

[70] H. A. Haus, "Theory of mode locking with a fast saturable absorber," *Journal of Applied Physics*, vol. 46, pp. 3049–3058, July 1975.

[71] L. A. Lugiato and R. Lefever, "Spatial dissipative structures in passive optical systems," *Physical Review Letters*, vol. 58, pp. 2209–2211, May 1987.

[72] P. Harrison and A. Valavanis, *Quantum Wells, Wires and Dots.* John Wiley & Sons, Ltd, May 2016.

[73] C. W. I. Chan, *Towards room-temperature Terahertz Quantum Cascade Lasers: directions and design.* PhD thesis, 2015.

[74] S. L. Chuang, *Physics of Photonic Devices.* Wiley, Jan. 2009.